PERFORMANCE OF A TLD WITH INCLINED AND OSCILLATING SCREENS

THE PERFORMANCE OF A TUNED LIQUID DAMPER EQUIPPED WITH INCLINED AND OSCILLATING DAMPING SCREENS

By

MARCUS RICHARD CASSOLATO, B.E.SC., B.SC.

A Thesis
Submitted to the School of Graduate Studies
in Partial Fulfilment of the Requirements
for the Degree
Master of Applied Science

McMaster University

MASTER OF APPLIED SCIENCE (2007)
(Civil Engineering)

McMaster University
Hamilton, Ontario, Canada

TITLE: The Performance of a Tuned Liquid Damper Equipped with Inclined and Oscillating Damping Screens

AUTHOR: Marcus R. Cassolato, B.E.Sc., B.Sc. (The University of Western Ontario [UWO])

SUPERVISOR: Professor Michael J. Tait

NUMBER OF PAGES: xxii, 201

ABSTRACT

The first application of the *tuned liquid damper* (TLD) to mitigate the dynamic vibrations of structures was only around 20 years ago and has just been recently applied in North America. TLDs are partially fluid filled tanks (usually water) with a fundamental sloshing frequency tuned close to the frequency of the dynamic mode of structural vibration to be suppressed. Water alone is insufficient to achieve the level of damping typically required for design. Damping devices are often submerged in the water to greatly increase the inherent TLD damping. The damping device investigated in this study is a thin sharp-edged horizontal-slat screen. TLDs with such screens of a particular solidity are designed for one target amplitude of structural response and have limited efficiency over a range of structural response. To increase the efficiency, the concept of *smart screens* is introduced in this study.

Smart screens is the name given to a damping screen that alters its fluid pressure-loss characteristics at differing levels of excitation, (ideally) in a passive state of control. Symmetric fixed-angle screens and oscillating (rotating) parallel-linked screens are experimentally investigated inside a rectangular TLD on a shake-table under sinusoidal motion in this study.

TLDs have similar principles to common *tuned mass damper*s (TMD) and are analyzed accordingly. The TLD equipped with fixed-angle screens is modelled with linear numerical fluid models to simulate the TLD performance for preliminary design purposes. An inclined screen alters the pressure-loss characteristics from its typical vertical position, which in turn changes the inherent TLD damping, allowing damping to be controlled by simple screen rotation. The analytical models, including the utilization of a pressure-loss coefficient for an inclined horizontal-slat screen in oscillatory flow developed in this study, are compared with experimental results to verify their accuracy and ascertain limitations.

Oscillating smart screens are investigated mainly for their practical consideration in a preferred passive mode of control. The screens rotate automatically with changes in fluid velocity (or excitation amplitude). Their ability to maintain a near-constant amount of TLD damping (or resonant energy dissipation) is examined. Other implementations of (passive) smart screens are possible and suggestions for future study are recommended.

A TLD equipped with the mathematically modelled symmetric fixed-angle screens is theoretically investigated in a hypothetical structure-TLD system. This system demonstrates the ability of a smart screen to change its damping characteristics—altering the angle of inclination in this study—over a range of structural response thereby maintaining an optimal level of efficiency over a range of structural response accelerations.

ACKNOWLEDGEMENTS

First and foremost, I would like to genuinely express my utmost appreciation to my supervisor, Dr. Mike Tait. As a close colleague, his extreme interest, guidance, and faith in me are unprecedented. Thank you for taking me under your wing on your quest to McMaster University.

I would like to thank all the technical staff working in the Applied Dynamics Laboratory and Engineering Machine Shop. Most of all, I owe a lot to Peter Koudys, Geotechnical Lab technician, for giving me his patient knowledge, time, and extraordinary craftsmanship.

I would also like to express my heartfelt gratitude to all the friendly faculty, staff, and students I've met in my journey. Thanks especially to the chair of the department (Sept. `04 – July `06), Dr. D. Stolle, for his very kind support along with Carol Robinson and the administrative staff for always being resourceful and friendly.

To the many friends and acquaintances I've made amongst my fellow students, to name a few: Jason Crossen, Frank Campanaro, Lisa Federico, Larisa Logan (Long), Cam Baker, Shawn Miller, Xiaocong ("Cong") Deng, Eric Catania, Jamie Hamelin, Mike Wesolowsky, Daman Panesar, and Kevin Mumford. Your immediate support and companionship are treasured and I will never forget the many fond memories. Enormous thanks to undergraduate summer research student, Joseph Shayne Love, for his great help and competence.

Last but certainly not least, I would like to thank my family for their endless support and understanding. Thank you to my mother for her reassuring words and limitless faith in me.

This thesis is also dedicated to my wife, Gina, for her unyielding sacrifices and immeasurable support during this study.

To the memory of my father,
whose everlasting
wisdom, intelligence, and support
made this journey possible.

TABLE OF CONTENTS

LIST OF FIGURES

Figure No. and Description **Page**

LIST OF TABLES

NOMENCLATURE

A	amplitude of sinusoidal displacement
A_c	area of fluid jet at vena contracta
A_{cs}	cross-sectional area of submerged screen
A_g	total gross area of screen submerged in water
A_s	total solid area of screen (and structural components) submerged in water
b	tank width
b_s	damping screen slat spacing (on-centre)
c	damping (structural damping, C)
C	ratio of flow area at vena contracta to screen area, i.e., $C = (1 - \mathrm{S})C_c$
C_c	contraction coefficient for damping screen
C_D	drag force coefficient of damping screen
C_l	pressure-loss coefficient of (vertical) damping screen
C_m	inertia coefficient
C_u	linearized velocity loss coefficient
C_θ	pressure-loss coefficient of damping screen as a function of θ
d	damping screen slat width (5mm)
DMF	dynamic magnification factor
E	energy (energy dissipation, $E_d = E_w = E_{sw}$)
e_o	fluid particle displacement (sinusoidal amplitude)
f	forcing frequency (Hz)
F_b	total measured force from bottom platform in experimental testing rig
F_c	conservative forces
f_D	drag force (potential flow)
f_i	inertial force (potential flow)
f_n	natural fundamental fluid sloshing frequency (Hz)
F_{sw}	TLD sloshing force (amplitude) [from m_{eff}, non-conservative force]
F_t	total measured force from top platform in experimental testing rig

F_w	TLD base shear force (F_{sw} plus conservative forces)
g	gravitational constant (9.81m/s^2)
h	still water height (water depth)
H_2,H_∞	optimization techniques; variance opt. (spectrum), peak opt.
i	subtank number in linear shallow water wave theory (§4.4)
k	stiffness (structural stiffness, K)
KC	Keulegan-Carpenter number
L	tank length
m	mass (structural mass, M)
m_{eff}	(effective) participating mass
mg	"milli-g" ($^1\!/_{1000}$ the gravitational constant, g)
m_o	non-participating mass, $m_o = m_w - m_{eff}$
m_{vir}	virtual mass
M°	oscillating (moving) screens experimental results in figure legends (§5)
PF	Davenport's peak factor
q	generalized coordinate
Q	screen damping force
R	response ratio
Re	Reynolds number
S	general notation representing the effect of screen solidity
SC	surface contaminant factor in boundary layer damping
S_{eq}	solidity of damping device representing actual pressure-loss measured
SF	scale factor of experimental TLD (10)
S_n	nominal solidity of damping screen, $S_n = d/b_s$
T	period of excitation; kinetic energy
t	time
T_i	inertial kinetic energy
u	horizontal velocity; average u throughout h in §4.4
u_1	incident velocity to screen

u_c	vena contracta velocity through screen
U	average fluid velocity throughout water depth
u_o	fluid velocity (sinusoidal amplitude)
V	potential energy
w	vertical velocity
x	spatial coordinate (horizontal)
X, x_s	structural displacement
x_j	screen location
x_r	relative motion of (equivalent) TMD
z	spatial coordinate (vertical)
α	tuning ratio
β	forcing frequency ratio
γ	excitation factor
Γ	modal participation factor
γ_θ	Carrothers and Baines (1965) empirical pressure-loss ratio
δ	incremental parameter [prefix to variable]
ΔP	pressure difference across a screen
ζ	damping ratio
η	free-surface response (amplitude)
θ	damping screen angle (or inclination) measured from vertical position
Θ	integration term of damping force, Q_n, in Equation (4.33)
Λ	non-dimensional excitation amplitude; non-dim. shake-table displacement
λ	wavelength
μ	mass ratio
v	kinematic viscosity; cycling frequency
ρ	density of water
σ	RMS (std. dev.) response (σ_r, TMD response; σ_η, TLD fluid reponse)
φ	phase angle
ψ	deflection angle of exiting flow on leeward side of damping screen, $\psi(\theta)$

Ψ	efficiency
ω	radial forcing frequency (rad/s)
ω_n	radial natural fundamental sloshing frequency; modal sloshing frequency
Φ	velocity potential
$\hat{\ddot{x}}_s$	peak-hourly structural acceleration
ϕ	incidence angle of approaching flow; dynamic modal value
$\propto$	proportionality ($A \propto B$, A "dependent on / proportional to" B)
§	"section" symbol (prefix to section number, "§C.x.x", in a chapter, "C")

Common Subscripts

a	dynamic vibration *absorber* property
eff	effective parameter
eq	equivalent mechanical parameter
n	modal number or natural (fundamental) mode
nc	non-conservative parameter
o	amplitude parameter
opt	optimized parameter
s	structure property
sw	only sloshing water mass parameter
w	entire water mass parameter
x	horizontal component
z	vertical component

Common Superscripts

*	generalized parameter
′	non-dimensional parameter
··	acceleration ($\partial^2/\partial t^2$)
^	peak value

CHAPTER 1: INTRODUCTION AND LITERATURE REVIEW

1.1 Introduction

Seen in any major urban center in North America and around the world, there is the need for tall slender structures—commonly known as *skyscrapers*—to accommodate the urban economic core. Considerations when developing such structures are the utilization of space, prevention of urban sprawl, and an efficient use of resources. Consequently, these structures are becoming taller, lighter, increasingly flexible, and lightly damped, which magnify their sensitivity to dynamic excitations, thus requiring additional design considerations to satisfy both strength and serviceability requirements. For tall structures, serviceability requirements typically govern the design calling for a reduction in, for example, deflections and accelerations, primarily from wind loading. A structural response mitigation system is often used to meet such requirements. The main role of such systems is to dissipate a portion of energy that is input into the primary structural system by external forces.

1.2 Structural Response Mitigation System Classification

There are three main types of structural response mitigation systems: isolation, passive, and semi-active/active systems (Soong and Dargush 1997). Examples of dampers in these classifications are listed in Table 1.1. Isolation involves isolating the structure from the input excitation at the foundation level against earthquakes.

Table 1.1. Structural Response Mitigation Systems

Seismic Isolation	Passive Energy Dissipation	Semi-Active and Active Control
Elastomeric Bearings	Metallic Dampers	Active Bracing Systems
	Friction Dampers	Active Mass Dampers
Lead Rubber Bearings	Viscoelastic Dampers	
	Viscous Fluid Dampers	Variable Stiffness or Damping Systems
Sliding Friction Pendulum	Tuned Mass Dampers	Smart Materials
	Tuned Liquid Dampers	

(Soong and Dargush 1997)

Semi-active and active control systems require a feedback loop and external power source in order to operate. Semi-active systems require significantly lower external power requirements than active systems and can be seen as controllable passive systems. Passive energy dissipation devices require neither feedback nor any external power source, thus becoming a popular motion control strategy. The basic function of *passive energy dissipation devices* (PEDD), when incorporated into a structure, is to absorb or consume a portion of the input energy, directly or indirectly, resulting from wind or earthquake excitations, decreasing the energy dissipation demand on the primary structure (Soong and Dargush 1997).

Direct PEDDs consist of the top four items listed in the middle column of Table 1.1. Examples of direct energy dissipation mechanisms include the flow of a highly viscous fluid through an orifice (viscous fluid dampers) and the shearing action of a polymeric/rubber-like material in viscoelastic dampers (Kareem et al.

1999). Indirect energy dissipation mechanisms are those consisting of a secondary auxiliary system that imparts indirect damping through modification of the structure's own frequency-response (Kareem 1983). Those most popular being damped secondary inertial systems such as tuned mass and tuned liquid dampers.

1.3 Dynamic Vibration Absorbers

Passive auxiliary damping devices—first invented by Frahm in 1909 according to Den Hartog (1985)—are known, in general, as *dynamic vibration absorbers* (DVA). The most popular DVAs are the tuned mass and tuned liquid damper, which act on similar principles corresponding to a secondary mass being added to the structure. Unlike a tuned mass damper, which consists of a solid mass (concrete or steel), a tuned liquid damper utilizes liquid for the absorber mass. Currently, the most common DVA utilized is the tuned mass damper (Kareem et al. 1999); however, recent advancements in tuned liquid damper research and their growing application (§1.5) are making them an attractive option over traditional tuned mass dampers.

1.3.1 Tuned Mass Dampers

A *tuned mass damper* (TMD) is essentially a large mass, usually of concrete or steel, housed in an intricate mechanical system. They are only activated once excited and their effectiveness is only seen once there is movement between the building and device. It is the relative motion induced by the external excitation that makes a TMD functional. The effectiveness of a TMD depends on its mass and stiffness being properly tuned to the primary structure's dynamic mode of vibration that is to be suppressed. The objective is to optimize the transfer of the vibration energy from the building to the damper by considering the resonant frequency of the damper.

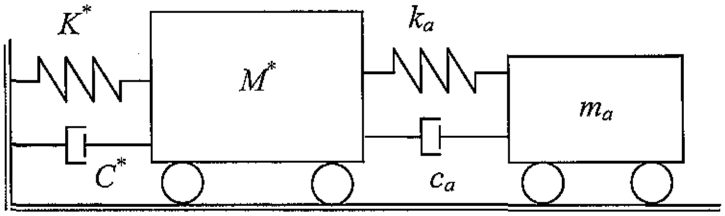

Figure 1.1. Theoretical representation of a structure-DVA system.

A TMD consists of a mass (m_a), a spring (stiffness, k_a), and a dashpot (damping, c_a) as shown in Figure 1.1. The structure is represented similarly utilizing the generalized parameters of the target mode of vibration (generalized mass, M^*, generalized stiffness, K^*, and generalized viscous damping, C^*). The simple mechanism of reducing building vibration is the inertial force from the TMD being exerted back onto the primary structure, applied antiphase to the excitation force.

1.3.2 Tuned Liquid Dampers

The *tuned liquid damper* (TLD) operates in a manner similar to that of a TMD and, therefore, a great deal of the analysis and design is in parallel with

TMD theory. However, the primary difference from a TMD is the amplitude-dependent (non-linear) nature of fluid response. Often a TLD is modelled as an equivalent mechanical system like the TMD; the TLD has a similar mass, spring, and dashpot representation of the fluid, illustrated in Figure 1.2(c). Depending on the type of TLD and theoretical model used, the mass, stiffness, and damping, can be represented in vastly different ways. Yu et al. (1999) modelled a TLD as the entire water mass participating with a non-linear stiffness hardening parameter and non-linear damping based on the excitation amplitude, denoted the NSD model. Tait (2004) expanded on Yu et al. (1999) considering only the participating portion of the fluid. Sun et al. (1995) created an amplitude-dependent virtual mass and virtual damping model matching the properties of an equivalent mechanical amplitude-dependent TMD. Graham and Rodriguez (1952) and Warnitchai and Pinkaew (1998) represent the mass, stiffness, and damping using potential flow theory and dynamic equations of motion.

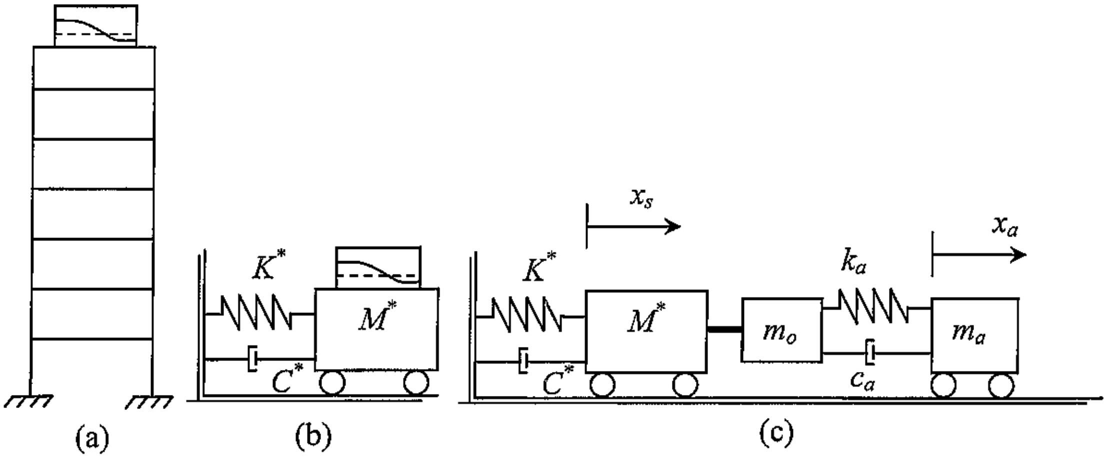

Figure 1.2. (a) Structure-TLD (b) Theoretical representation (c) TMD analogy.

Figure 1.2 demonstrates that not all the fluid in a TLD tank participates in the sloshing motion of the water. This non-participating portion of the water, m_o, is added to the primary mass of the structure. The participating mass in a TLD, m_a, contributes to the inertial force. The natural sloshing frequency of the TLD (Equation (4.39) with $n = 1$, rectangular tank) is tuned to the dynamic properties of the structure, like a TMD, in the direction of motion(s) considered.

A TLD uses the sloshing motion of the liquid to absorb building vibration energy as kinetic energy of the liquid motion and dissipates it through the viscous shearing of the liquid, friction between liquid and container wall, collisions of floating particles, etc. (Tamura 1998). However, the damping provided by sloshing water alone is still insufficient for optimal design. Typically for structures, water is preferred inside a TLD because of their storage benefits.

Utilizing liquid motion as a vibration absorber for structures is relatively new. TLDs were first used in 1902 by Frahm who built a system of two tanks half filled with water into a large ship, communicating through a water pipe below and through an air pipe above (Den Hartog 1985), see Figure 1.3(b). These "anti-rolling tanks" were perhaps the first use of a *tuned liquid column damper* (TLCD) that passively used a "gravity spring" and the corresponding natural frequency of the column of liquid rising and falling in its U-tube shape (Figure 1.3(a)). More recently, Sakai et al. (1989) proposed the TLCD to be used as a new type of DVA in structural applications (cable-stayed bridge towers). TLDs were applied as a vibration absorber to reduce the oscillations of space satellites (Carrier and Miles

1960) and were called *nutation dampers*, which were a ring of liquid around the satellite to reduce rotations about the cylindrical principal axis (Figure 1.3(c)).

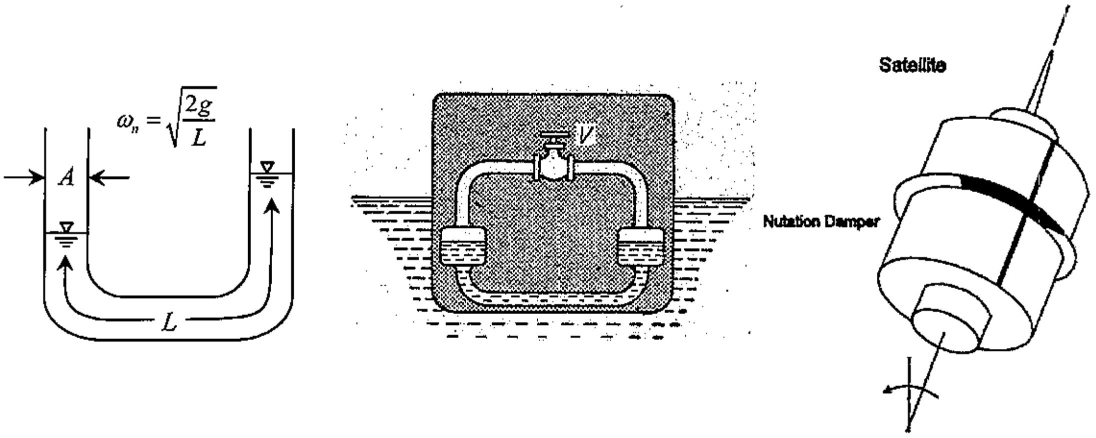

(a) (b) (c)

Figure 1.3. (a) TLCD (b) Frahm's anti-rolling tank (c) Nutation damper in satellite.

Initial structural applications of TLDs were proposed in the mid-to-late 1980s by studies such as Modi and Welt (1987), Kareem and Sun (1987), and Fujino et al. (1988).

1.4 Types of Tuned Liquid Dampers

The liquid container can be of many different shapes and sizes. The most common being rectangular, cylindrical, annular (nutation/toroidal), conical (Figure 1.4), and U-tube shapes (Figure 1.3(a)).

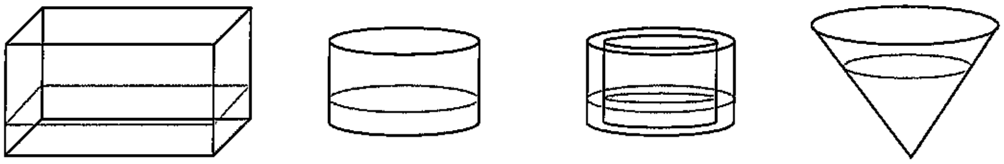

rectangular cylindrical annular (nutation) conical

Figure 1.4. Various shapes of tuned liquid damper tanks.

Casciati et al. (2003) studied a frustum-conical tank in contrast to the widely used cylindrical tank and detailed a linearized SDOF model for small excitations as well as a non-linear model with amplitude-dependent equivalent TMD parameters for larger excitations. Modi and Welt (1987) conducted an experimental and analytical study on a nutation damper. Their theoretical investigation addressed the energy-dissipation mechanism assuming potential flow with a non-linear free-surface condition in conjunction with boundary-layer correction. Sun et al. (1995) studied rectangular, cylindrical, and annular tanks using virtual mass and damping parameters. TLCDs, mentioned in the previous section, are becoming an increasingly popular type of DVA. Gao and Kwok (1997) studied the effectiveness of U-shaped and V-shaped TLCDs in controlling structural vibration and estimated the optimum parameters of TLCDs for maximum reduction of peak structural response to harmonic excitation. Yalla and Kareem (2000) developed similar optimum parameters under random "white-noise" excitation for TLCDs and applied them to a semi-active TLCD to improve optimal performance over an increased range of excitation (Yalla and Kareem 2003).

Olson and Reed (2001) investigated a sloped-bottom rectangular TLD with 30° (from tank bottom) wedges at either end of the tank to investigate the increase in participating fluid sloshing mass and utilized a NSD (*non-linear stiffness and damping*) model developed by Yu et al. (1999). Rectangular TLDs have been used in many structures to effectively reduce vibration in one direction of motion (Fediw et al. 1995). However, recent extensive non-linear amplitude-dependent numerical modelling and experimental testing on *two-dimensional* (2-D) TLDs in a rectangular shape, under multi-directional excitation, have been shown to be very effective in suppressing structural motion in two principal directions (Tait 2004). The sloshing dynamics for 2-D TLDs in each principal axis were found to be independent, which makes 1-D numerical modelling readily applicable in each direction (Tait 2004).

A rectangular TLD can be classified as shallow-water or deep-water based on the ratio of fluid depth, h, to tank length, L. Shallow-water TLDs, $h/L < 0.1$, have a large participating mass and a highly non-linear free-surface motion at large amplitudes including wave breaking, making analytical modelling difficult. The NSD model from Yu et al. (1999) attempts to account for the wave breaking phenomenon. Shallow-water TLDs have been successfully modelled using linear shallow water wave theory suitable for small excitations (Fediw 1992). On the other hand, for a large range of excitation, non-linear models are more accurate (Tait 2004, Kaneko and Ishikawa 1999). Deep-water TLDs, $h/L > 0.2$, are also utilized as DVAs, however the level of participating mass is reduced (Noji et al. 1988). Although their response is more linear, they typically require additional damping devices to be placed inside the tank such as screens. Kaneko and Yoshida (1999) modelled a deep-water TLD with submerged nets (screens) using finite amplitude theory. Deep-water TLDs are popular when they are primarily used as water storage tanks, while providing structural vibration mitigation.

1.5 Applications of TMDs and TLDs

TMDs and TLDs are installed primarily in tall structures (skyscrapers) to reduce building vibrations; in particular, building accelerations that an occupant feels during building motion. For example, a tall structure with a large lateral displacement may not necessarily be sensed with a long period of motion. There is still no international consensus on the design descriptor of acceleration (McNamara et al. 2002, Boggs 1997). RMS or peak acceleration is at the heart of the debate. RMS acceleration is considered by some researchers to be more representative especially considering what an occupant feels over the course of an hour or so, which is also reliable and simpler to evaluate (Boggs 1997). Peak acceleration criteria typically govern in North America and Davenport's peak factor, g (Davenport 1964), is a widely adopted method for estimating peaks from RMS accelerations. Various wind-induced acceleration criteria are listed in Tait (2004), which categorize three main building types and their hourly peak horizontal accelerations: residential from 10 to 15mg, hotels from 15 to 20mg, and offices from 20 to 30mg (see Nomenclature for use of "mg").

A few of the earliest applications of tuned mass dampers were in North America. In the 244m tall Hancock Tower in Boston, MA, USA, two TMDs were installed at opposite ends of the 58th floor in order to counteract the torsional motion (Kareem et al. 1999). Each unit is essentially a steel box filled with lead weighing 300tons, which is activated at 3mg of motion. Another application of

TMDs is in the 278m high Citicorp Building in New York, NY, USA. The system consists of a 410ton concrete block with two spring damping mechanisms (Figure 1.5), one for north-south motion and the other for east-west motion, installed on the 63rd floor (Kareem et al. 1999). The block, resting on a series of 12 hydraulic pressure-balanced bearings, has its motion inhibited by 2 pneumatic springs tuned to the natural period of the building; the system, including computer-controlled hydraulic actuators, reduces wind-induced response by 40% in both directions simultaneously (Wiesner 1979).

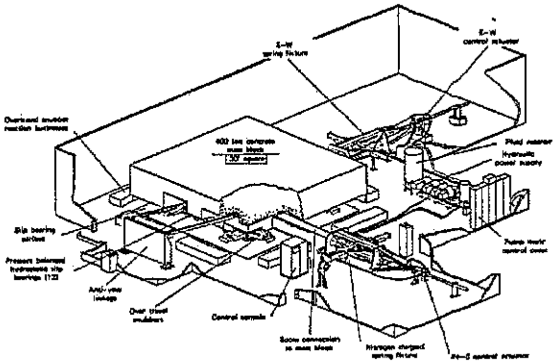

Figure 1.5. Schematic of TMD in Citicorp, NY.

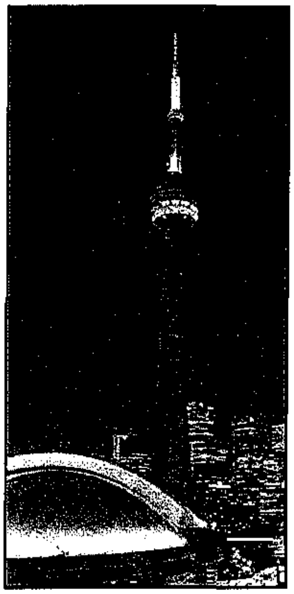

Figure 1.6. CN Tower.

In Canada, the 554m high CN Tower in Toronto, ON (see Figure 1.6), had 20ton donut-shaped lead pendulum TMDs installed during construction in 1975 (Kareem et al. 1999). A pendulum-type TMD is utilized in Taipei 101 in Taipei, Taiwan. It consists of a 680ton steel ball suspended from cables at the 92nd floor visible from observation decks and a restaurant (Figure 1.7); it is the largest anti-sway system in the world (Hadenius 2004). The pendulum-type TMD works on the same principle as a typical translational TMD but instead uses a swinging motion to exert its inertial restoring force onto the structure (Gerges and Vickery 2003).

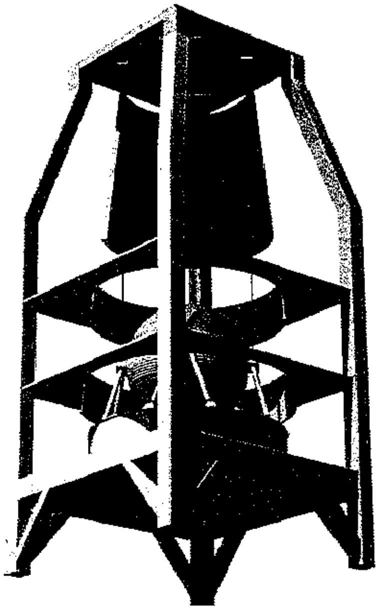

Figure 1.7. Pendulum-TMD in Taipei 101.

As mentioned earlier, the application of the TLD in civil engineering structures emerged in the 1980s. Their application is becoming increasing popular as they have numerous benefits over a TMD:

- Innate simplicity in construction: a tank of water
- Low installation and maintenance costs
- Ease of retrofit capability (multiple small TLDs)
- Ease of tuning, the natural frequency of the TLD can be adjusted by simply changing the water depth
- Dual-function capability (water storage; fire suppression system)
- No activation mechanism is required and TLDs remain active all the time, unlike TMDs where activation must be made at a certain threshold of excitation (Soong and Dargush 1997)
- TLDs can operate in all possible directions in the horizontal plane

The cons of a TLD are its non-linear amplitude-dependent response, only a portion of the mass participates, and a large amount of space is required to achieve a particular mass ratio, μ. The non-linear response behaviour results in a more complex design and analysis process over traditional TMDs.

TLDs were initially installed in great numbers over in the Far East, especially Japan, where most of the initial research and development began. Tamura et al. (1995) outline some full-scale experiments on the effectiveness of TLDs in buildings under wind excitations conducted on four buildings that are frequently referenced. The Nagasaki Airport Tower, the Yokohama Marine Tower, the Shin-Yokohama Prince Hotel (SYPH), and the Tokyo International Airport Tower in Japan are the four buildings. All four structures were installed with multiple cylindrical TLDs, sometimes generally referred to as *multiple mass dampers* (MMDs).

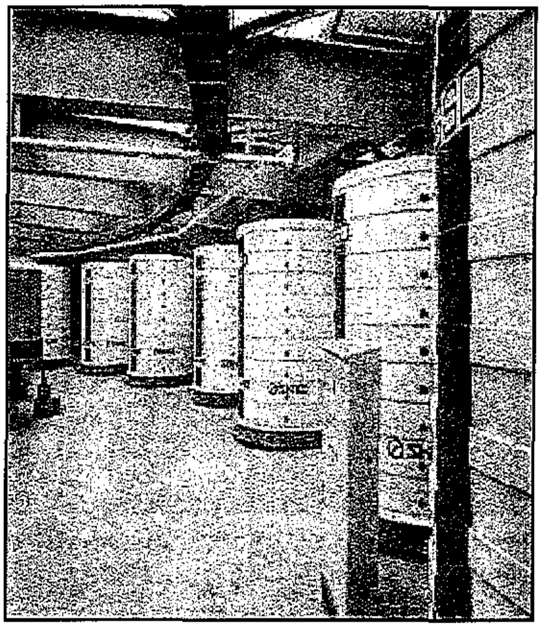
Figure 1.8. Stacks of cylindrical-TLD MMDs installed in SYPH (Tamura et al. 1995).

In the SYPH, The TLD system prescribed was a multi-layer stack of 9 circular containers each 2m in diameter and 22cm high, yielding a total height of 2m. It was found that the RMS accelerations in each direction were reduced 50% to 70% by the TLD at wind speeds over 20m/s, with the decrease in response becoming even greater at higher wind speeds due to the TLDs achieving optimal damping (Tamura et al. 1995). The RMS acceleration without the TLD for the building was over $0.01 m/s^2$, which was reduced to less than $0.006 m/s^2$, defined by the International Organization for Standardization (ISO) as the minimum perception level at 0.31Hz.

There are two recent examples of TLD applications in Canada, One Wall Centre in Vancouver, BC, and 1 King West in Toronto, ON (Figure 1.9).

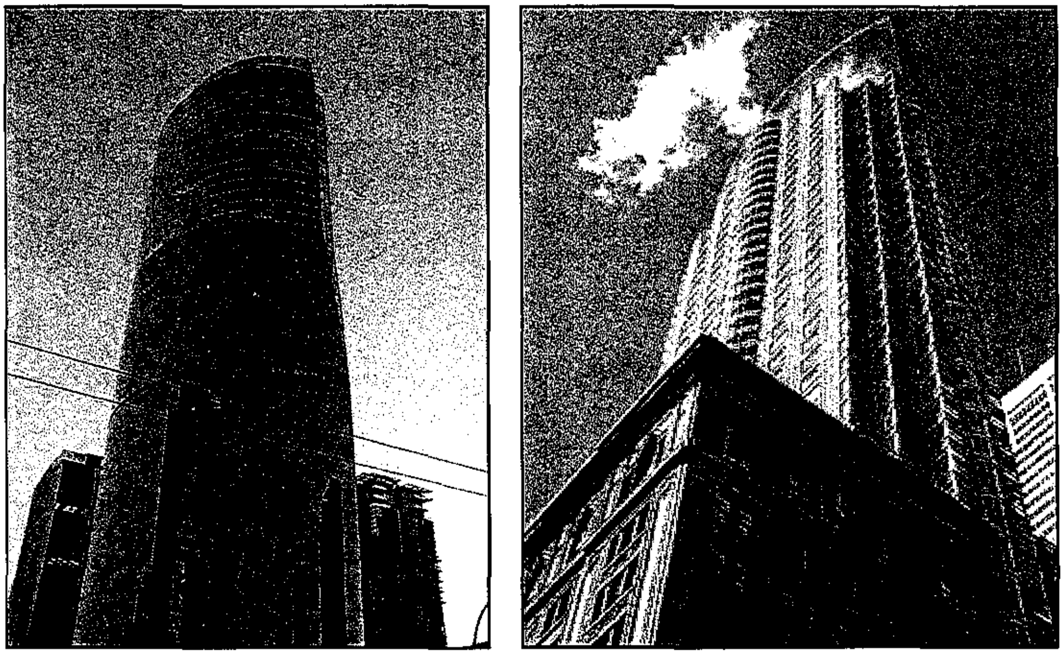

Figure 1.9. One Wall Centre, Vancouver (left). 1 King West, Toronto (right).

The 150m high One Wall Centre is the tallest building in Vancouver with a 21.3m wide elliptical footprint and a 7:1 slenderness ratio (Motioneering 2004). Two TLCDs were installed that consist of a 4-storey high, 189000L U-shaped water tank oriented across the narrow aspect of the building. An estimated $2M in construction costs were saved compared to conventional damping systems and additional overall cost savings were realized by using water in TLCD tanks to meet fire suppression water storage requirements (Motioneering 2004). This solution was the first of its kind and size in the world.

The 176m high 1 King West building in Toronto was built incorporating the original head office of The Dominion Bank of Canada built in 1914 and has a slenderness ratio of 11:1 (SkyscraperPage 2007). Two insulated concrete TLDs (rectangular) equipped with damping screens were installed on the 51st floor, 12x9x2m in size, on each side of the building divided into 5 chambers by cross-walls so the predominate water flow is in the East-West direction, which is the critical direction for the building (Discovery 2005). This application of TLDs to such a slender structure is unprecedented in North America.

1.6 Damping & Optimization Techniques in DVAs

As alluded to earlier in §1.3.2, water alone provides insufficient inherent TLD damping in most cases for the optimal design of a TLD for structural applications. Research on TLDs outlined earlier revealed work conducted to optimize the damping characteristics of the damper. Design criteria for DVAs often require an optimal damping ratio for at least one particular amplitude of structural excitation. Den Hartog (1985) mathematically introduced the concept of optimal damping in a passive damped vibration absorber in his first edition of *Mechanical Vibrations* in 1934, which will be described here.

The undamped structure consists of mass, M, and stiffness, K, with a DVA attached with mass, stiffness, and damping, m, k, and c, respectively, similar to that shown in Figure 1.1, ignoring the structural dashpot. The structure is subjected to a harmonic force, $P_o\sin\omega t$, with excitation frequency, ω. The natural frequencies of the structure and absorber are $\omega_s = \sqrt{K/M}$ and $\omega_a = \sqrt{k/m}$, respectively. The forced frequency ratio defined as, $\beta = \omega/\omega_s$, and the tuning ratio between the damper and the absorber is $\alpha = \omega_a/\omega_s$. Derived from the equations of motion is the dynamic magnification factor, *DMF*, relating the dynamic displacement of the main structure to its static displacement, P_o/K, often referred to as the classic Den Hartog solution:

$$DMF = \sqrt{\frac{(2\zeta\beta\alpha)^2 + (\beta^2 - \alpha^2)^2}{(2\zeta\beta\alpha)^2(\beta^2 - 1 + \mu\beta^2)^2 + \left[\mu\alpha^2\beta^2 - (\beta^2 - 1)(\beta^2 - \alpha^2)\right]^2}} \tag{1.1}$$

Equation (1.1) is plotted below in Figure 1.10 with varying values of the damping ratio of the absorber, $\zeta = c/2m\omega_a$. The mass ratio and tuning ratio are fixed at

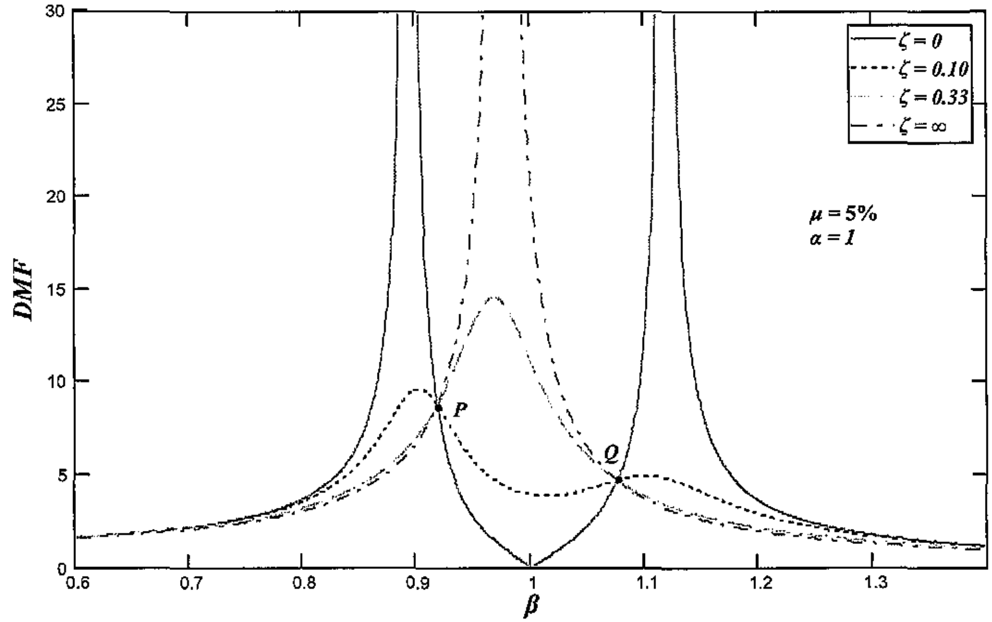

Figure 1.10. Dynamic magnification factor of main mass for various values of absorber damping ratio, ζ. (all curves pass through P and Q)

$\mu = m/M = 5\%$ and $\alpha = 1$, respectively.

For $\zeta = 0$ or $\zeta = \infty$, the peak(s) is infinite. For $\zeta = 0$, no DVA damping, the two masses behave independently with two peaks tending to infinity. For $\zeta = \infty$, infinite DVA damping, the masses are fused together resembling an undamped single-degree-of-freedom system. Therefore, somewhere in between the limiting values of ζ there exists a value for which the two peaks take on values that minimize the response of the main mass (or hypothetical structure). This corresponding value of ζ is called the *optimal damping ratio*, ζ_{opt}. The best obtainable resonant amplitude at optimal damping is the ordinate of points *P* or *Q*.

Note that the points *P* and *Q* in Figure 1.10 are staggered, which means that the absorber and the main structure are not optimally tuned, α_{opt}. Complete derivations can be found in Den Hartog (1985) and Brock (1946) for the equations of the optimal tuning ratio that balance the ordinates of *P* and *Q* and the corresponding optimal damping ratio. They are,

$$\alpha_{opt} = \frac{1}{1+\mu} \tag{1.2}$$

$$\zeta_{opt} = \sqrt{\frac{3\mu}{8(1+\mu)}} \qquad (1.3)^{*}$$

The demonstration of the classic Den Hartog solution to minimize the main structural displacement clearly indicates the influence of the TLD damping parameter and its optimal value that minimizes the response of the main structure.

---

[*] Refer to Asami et al. (2002) for further clarification of this result

However, this situation is ideal for a main structure with no damping subjected to a pure harmonic force, equipped with a DVA having a solid mass and amplitude-independent behaviour (a TMD). This may not always be a realistic situation as some structural damping will exist, albeit usually small or negligible. For example, tall structures are mainly susceptible to wind-induced excitation, which is treated as a random "white-noise" excitation. In the case of TLDs, which are naturally amplitude-dependent, equivalent mechanical models must be developed to account for their non-linearity. Many other different minimization criteria exist besides minimal structural displacement due to a harmonic force as mentioned at the beginning of §1.5. Some of these are listed below (Soong and Dargush 1997):

- Minimum displacement of main structure (Den Hartog 1985)
- Maximum effective damping, ζ_{eff}, of combined structure/DVA system (McNamara 1977, Luft 1979) (Figure 1.11, right)
- Minimum relative motion between DVA and main structure (McNamara 1977, Luft 1979)
- Minimum velocity or acceleration of main structure (Warburton 1982)

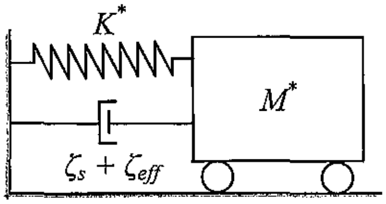

Figure 1.11. Equivalent single-degree-of-freedom system with effective damping.

Warburton (1982) completed an extensive set of closed-form solutions of α_{opt} and ζ_{opt} for damped and undamped structures that are frequently utilized in research and application. Closed-form solutions for α_{opt} and ζ_{opt} are quite complex for a damped structure but if the structure possesses little damping, it may be neglected altogether in favour of a more streamlined design (Vickery et al. 2001). Asami et al. (2002), Nishihara and Asami (2002), and Asami and Nishihara (2003) present arguments for a closed-form solution for H_2 and H_∞ optimization of the absorber, especially for damped structures. H_∞ optimization is the classic (Den Hartog) optimization presented earlier (minimization of infinite peak(s), "∞"). H_2 optimization—meant for the reduction of a spectrum of frequencies, not just the resonant frequency, ω_s—is to reduce the total vibration energy of the system over all frequencies (Asami et al. 2002). In H_2, the area under the frequency-response curve of the system is minimized.

With the significance of optimal DVA damping established, this study's focus on TLDs and the inadequate amount of damping provided by water alone will be addressed in the following section.

1.7 Damping Screens Submerged in TLDs

Often, poles, screens, and other objects are submerged in the water to introduce additional energy dissipating mechanisms as the various energy dissipating mechanisms of water alone are insufficient. Research mentioned previously in this chapter included work done on such damping devices to achieve optimal damping parameters. Warnitchai and Pinkaew (1998) developed a mathematical model based on potential flow theory and determined the damping characteristics of poles and wire-mesh screens. Ju (2004) performed experiments and created an equivalent mechanical model for a WSDE (*water sloshing damper with embossments*), which is a rectangular TLD, equipped with or without wire-mesh screens, including embossments distributed on the end walls where the vertical velocity of the fluid is maximum (following Warnitchai and Pinkaew (1998)) adding additional damping. The embossments dissipate the energy of the vertical fluid velocity at the end walls. While the embossments increased damping, the total effective damping without screens was insufficient for optimal design against wind-induced forces (Ju 2004).

Fediw (1992) and Tait (2004) successfully experimented and modelled screens in a TLD showing that their drag characteristics can often be considered independent of fluid flow inside a TLD with wire-mesh and thin-sharp-edged-horizontal-slat screens, respectively. Both studies utilized a linearized fluid velocity loss coefficient. The fundamental damping characteristics of screens are related to the square of the velocity given by the well-known relationship,

$$C_l = \frac{\Delta P}{\frac{1}{2}\rho U_0^{\,2}} \tag{1.4}$$

where ΔP is the pressure-drop across the screen, ρ is the density of water, U_o is the average velocity at the screen, and C_l is the resulting pressure-loss coefficient of the screen. Prandtl (1933) appears to be the first to obtain a "pressure-drop" expression for the reduction of the differences in mean wind speed through screens (Schubauer et al. 1950).

Fediw (1992) and Tait (2004) also showed that thin screens inside a TLD are independent of fluid flow when the Keulegan-Carpenter number, $KC = U_o T/d$ (Equation (4.62)), is sufficiently large, $KC > 25$ (Keulegan and Carpenter 1958), applicable in a range of excitation right down to small amplitudes. A loss coefficient independent of fluid flow simplifies the design process of TLDs equipped with damping screens. Ultimately, screens (or any damping device) can be optimally designed to achieve ζ_{opt} for a particular amplitude of excitation. The efficiency of TLDs equipped with damping screens reduces, if the amplitude of excitation increases or decreases from the optimized target amplitude (Tait 2004). This brings to light the focus of this study: to increase the efficiency of a TLD equipped with screens over a *range* of structural response amplitude.

1.8 Smart Screens

In order to increase the efficiency of *KC*-independent damping screens, the objective of this thesis is to orient the screens at various angles in order to change the pressure-drop coefficient (Equation (1.4)) that alters the absorber damping, intending to optimize the TLD at different excitation amplitudes. *Smart Screens* is the name given to this concept, which possesses two key characteristics:

(1) Damping screens (*KC*-independent) that change angle in order to vary C_l, to control ζ of the TLD

(2) "Smart" screens change their orientation in the flow automatically—or *passively*—amidst the sloshing liquid motion when the amplitude of excitation increases or decreases

It is well documented that the pressure-loss coefficient of a vertical screen is a function of solidity (or porosity), Reynolds number, and Mach number (Laws and Livesey 1978); however, Mach fluid speeds are not characteristic in a TLD. Baines and Peterson (1951) and Cornell (1957) describe the pressure-loss coefficient in terms of the solidity of the screen. Cornell (1957) showed that the loss coefficient becomes independent of Reynolds number, *Re*, at high values of *Re*. Baines and Peterson (1951) developed a loss coefficient for a screen as a function of the solidity, independent of *Re*. Tait (2004) showed use of the loss coefficient from Baines and Peterson (1951) was independent of the Keulegan-Carpenter number, *KC*, in oscillatory flow as discussed earlier.

Numerous studies exist that describe the pressure-loss characteristics of angled screens but few exist with a detailed mathematical analysis and extensive experimental support over a large range of screen solidity, certainly not in oscillatory flow. Many researchers have demonstrated that the pressure-drop variation with angle of attack is a simple trigonometric relationship. The parameter, θ, describes the angle between the incident velocity and the screen orientation here (Figure 1.12). Idelchik (1986) reported the change in loss coefficient as simply $\sin(90° - \theta)$ for angled screens, grates, grillages, etc. Laws and Livesey (1978), Richards and Robinson (1999), Schubauer et al. (1950), and

Brundrett (1993) all report a $\cos^2\theta$ relationship for the loss coefficient for a variety of screen types. Schubauer et al. (1950) in particular reported the pressure-drop to be proportional to the square of the component of the velocity normal to the screen, similar to the cross-flow principle (Garrison (1985), Hoerner (1964)). Carrothers and Baines (1965) performed experiments on angled screens with a variety of solidities all under 0.50. They found that the $\cos^2\theta$ relationship overestimates the loss coefficient for $\theta > 45°$ and developed an empirical correction for $\theta > 45°$ based on their experimental data. Blevins (1984) also supported these findings.

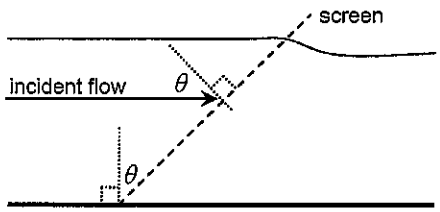

Figure 1.12. Inclined screen.

Reuter et al. (2001) developed a formula for angled screens including shape factors for the influence of the horizontal bearings and vertical rakes of a wedge-wire screen. Reuter et al. (2001) also found that the screen studied was independent of the flow, from velocities 0.5 to 0.9m/s. Yeh and Shrestha (1989) present a mathematical model to determine the pressure-drop of inclined screens. An angled screen was studied similar to Reuter et al. (2001) at a flow velocity of approximately 0.60m/s. Yeh and Shrestha's (1989) theoretical formulation, which includes the incident flow velocity, was found to overpredict the decrease in pressure-drop at high inclinations ($\theta > 60°$) when contrasted with their own experimental results, where they observed a minimum around $\theta \approx 60°$. Reuter et al. (2001) attributes this to Yeh and Shrestha (1989) neglecting the bearing profiles, which Yeh and Shrestha (1989) also recognized. However, the existence of a minimum could not be confirmed by Reuter et al. (2001) in their study.

Thus far, pressure-drop characteristics reported for angled screens were studied in open channel steady flow. For oscillatory flow, little work exists on the nature of inclined screens. Badr (1994) studied the fluid losses of inclined elliptic cylinders with flat plates (indicative of a horizontal slat in a slat-screen) as a special case. Badr's (1994) drag coefficient formulation for an inclined flat plate was reduced from an elliptic cylinder as a function of the angle of inclination and the Strouhal number. No experimental support was given in Badr (1994) and no applicable ranges of Reynolds or the Strouhal number were given. Okajima et al. (1998) examined flat plates with various angles of attack in oscillatory flow supporting the fact that experimental data on bluff bodies other than a circular cylinder are extremely rare, especially in the case of oscillatory flow. Okajima et al. (1998) examined the drag (or pressure-loss) coefficient versus the Keulegan-Carpenter number for oscillatory flow. Although their experimental study was insightful, no clear theoretical formulation was created or contrasted with.

For smart screen characteristic, (1), and the intent to use *KC*-independent inclined screens, this study will examine (in Chapter 4) the combination of the theory developed by Baines and Peterson (1951) and the detailed theoretical development for angled screens by Yeh and Shrestha (1989).

As for smart screen characteristic, (2), no directly applicable research was found during this study on passive motion of inclined screens in oscillatory flow.

Chapter 5 will be dedicated to experiments on such screens and their automatic damping modifications over various excitation amplitudes.

1.9 Overview of Thesis

Chapter 2 describes the extensive experimental program undertaken in this study including details on the design and construction of the test specimen and data acquisition. Background information on the testing rig, tuned liquid damper, and shake-table will also be presented.

Chapter 3 examines the experimental results of thin sharp-edged horizontal-slat screens held at various fixed-angles in a tuned liquid damper. The influence of screen angle and excitation amplitude will be discussed including sloshing forces, screen forces, free-surface response, and energy dissipation of the TLD.

Chapter 4 presents two linear numerical models utilized in this study including the effect of fixed-angle screens. Other researchers' formulations of the pressure-loss coefficient for inclined screens and one developed in this study will be used. Simulated frequency-response and time histories will be compared to the experimental results of Chapter 3.

Chapter 5 observes the experimental results of slat-screens (described in Chapter 2 and experimented on in Chapter 3 at fixed-angles) oscillating with the sloshing fluid motion about a hinge located near the bottom of the TLD tank. The increased invariability of the damping (or energy) will be examined including fluid forces and free-surface response. These moving "smart screen" results will also be compared to the results of Chapter 3.

Chapter 6 will theoretically look at the influence of inclined screens in a hypothetical structure-TLD system and their ability to maintain optimal damping over an increased range of structural response amplitude. The angled screen loss coefficient developed in Chapter 4 will be used to adjust the screen angle at differing amplitudes of structural response.

Chapter 7 reviews and discusses some of the important conclusions drawn from the presented research and highlights areas of future work that would be valuable in this area.

CHAPTER 2: DESIGN, CONSTRUCTION, AND DESCRIPTION OF TEST PROGRAM

2.1 Introduction

This chapter presents details of the experimental research conducted in this study, which are shake-table experiments of a scaled-model *tuned liquid damper* (TLD). The general test setup and method of instrumentation was derived from Tait (2004). The description of the test program, which includes the tank and screens will be detailed first, followed by the design and construction of the testing rig. The chapter also includes information on data acquisition, instrumentation, and filtering used in this study.

2.2 Tank and Damping Slat-Screens

A scaled-model (1:10) 1-D TLD was selected to be manufactured to match a TLD tank used by Tait (2004) as a benchmark, shown in Figure 2.1.

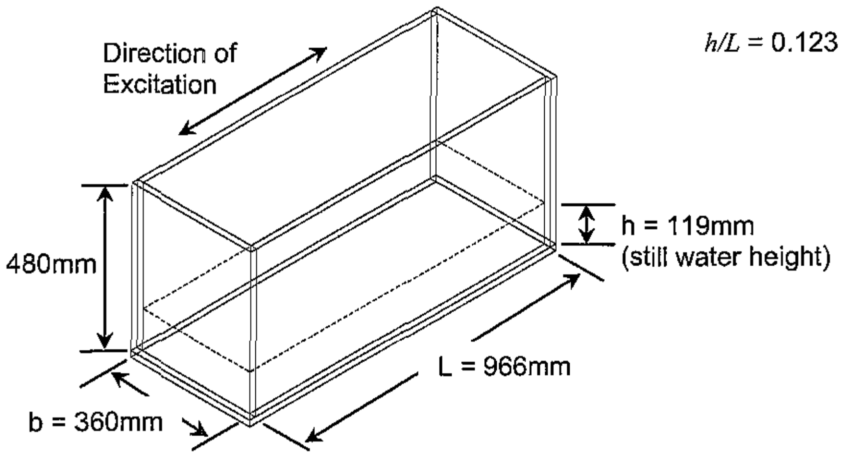

Figure 2.1. Schematic of 1-D TLD with inner dimensions.

The tank was fabricated of separate plastic acrylic panels (Plexiglas), ¾" (19.05mm) thick, bonded together using an adhesive. The measured dimensions for tank length, *L*, and tank width, *b*, are also shown in Figure 2.1.

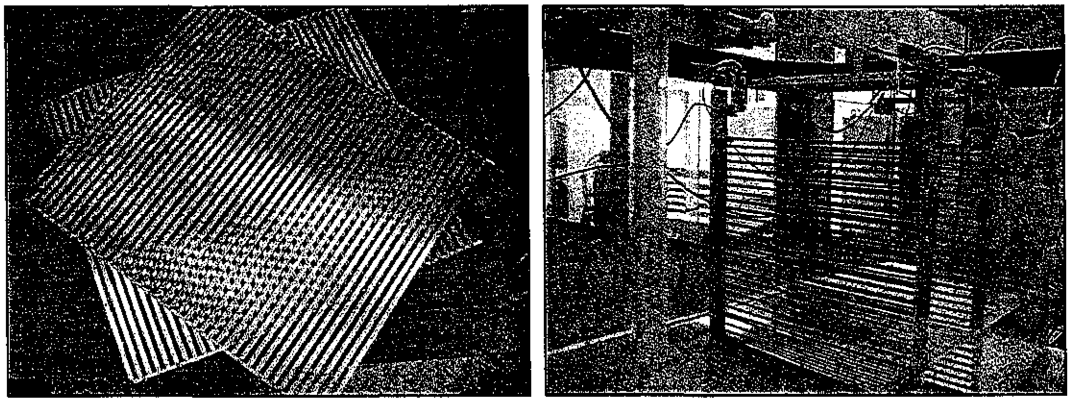

Figure 2.2. Stainless steel slat-screens (left). Slat-screens suspended inside TLD (right).

The focus of this study is the performance of fixed-angle and oscillating damping screens inside a TLD. Two different screen solidities were selected and are discussed in more detail in Chapter 3. The slat-screens used in this study are described by their nominal solidity ratio, S_n (expressed as a percentage), which is a characteristic of the screen and defined as the ratio of the slat width to the slat spacing,

$$S_n = \frac{d}{b_s} \tag{2.1}$$

where d is the slat width and b_s is the slat spacing (or on-centre spacing) as depicted in Figure 2.3.

Only a two-screen configuration was tested in this study. The screens, which were laser-cut from an approximately 1mm thick sheet of stainless steel,

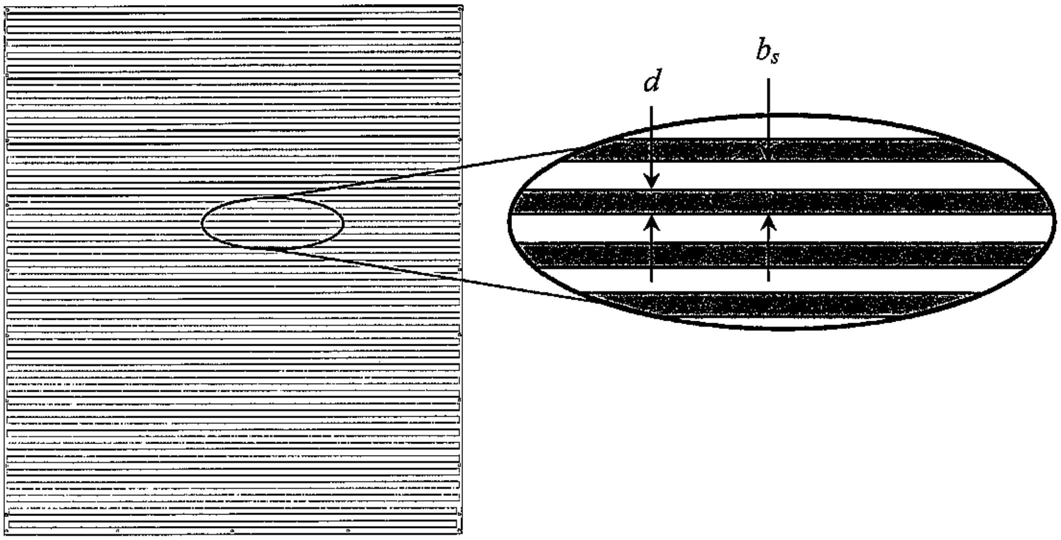

Figure 2.3. Thin sharp-edged horizontal-slat screen.

were attached to a frame by a hinge that allowed them to rotate (Figure 2.2/Figure 2.4). The frame was constructed of $\frac{3}{16}$" (4.7625mm) thick aluminum for rigidity and was suspended from load cells attached to the top of the tank walls with a 2mm gap between the frame and tank on all sides. Vertical aluminum stiffeners were used to reduce the screen flexibility. Small holes were laser-cut into the edges of the screens along the height and the screens were subsequently attached to the vertical aluminum stiffeners. The key aspect of the tests conducted was the angle of the screens, measured 0° at the vertical position shown in Figure 2.2 (right) to 90° rotated parallel to the tank bottom. In order to maintain symmetry, the two screens were tested at angles symmetric to each other.

All tests were conducted under sinusoidal excitation. A maximum of 8 amplitudes were tested over a range of approximately 41 frequencies to ensure sufficient resolution of the frequency-response curve. Five discrete screen angles

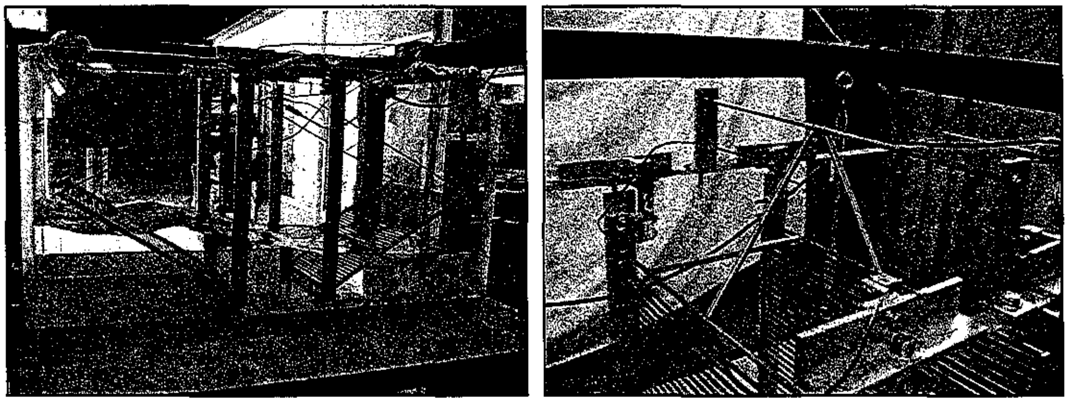

Figure 2.4. Screens at fixed-angle (left) and screens with a spring configuration (right).

were investigated, 0°, 15°, 30°, 45°, and 60°. In addition, a study was conducted to investigate *smart screens*. For this study, the screens were allowed to move with the oscillating flow under a spring configuration (Chapter 5). The left photo in Figure 2.4 depicts the screens being held at a fixed-angle. To achieve the desired angle, a rigid arm connection was made from the top of the frame below the load cells to the top of the vertical stiffeners of the screens, which allowed screen forces to be measured. The right photo in Figure 2.4 depicts the screens in a moving configuration test setup. The two screens were linked together between vertical stiffeners to ensure they remained parallel. A spring connection was made from a rod suspended above the centre of the tank to the screens below. Under this configuration the screen forces could not be measured as the connection scheme created a load transferring mechanism to the tank wall. However, this connection allowed sufficient screen motion and measurement of the screen forces was not as pertinent as achieving a particular screen angle, so screen forces for moving screens were not considered in this study. Moreover, the parallel configuration was chosen as opposed to a symmetric moving configuration (similar to fixed-angle arrangement) as it was considered to be the most likely arrangement for *passive* screen motion and was deemed a more viable option. For the regular vertical position, 0°, the screens were simply bolted into the sides of the frames through the vertical stiffeners (Figure 2.2, right).

The screens were sized such that all flow passed through the screens at the largest angle, 60°. This angle was chosen to be the largest angle tested as the screen losses were anticipated to be become minimal near this angle (Yeh and Shrestha 1989, Chwang and Chan 1998). At each excitation frequency, a 150sec time history was recorded. Data was not captured until the fluid attained a steady-state response. The scope of experimental tests can be found in the test matrix in Table 2.1, with 42% and 52% representing the nominal solidity ratios, S_n, of the two different sets of screens tested.

Table 2.1. Test Matrix

	Configuration											
Excitation Amplitude, A (mm)	0°		15°		30°		45°		60°		oscillating	
2.5	42%	52%	42%	52%	42%	52%	42%	52%	42%	52%	42%	52%
5	42%	52%	42%	52%	42%	52%	42%	52%	42%	52%	42%	52%
7.5	42%	52%	42%	52%	42%	52%	42%	52%	42%	52%	42%	52%
10	42%	52%	42%	52%	42%	52%	42%	52%	42%	52%	42%	52%
15	42%	52%	42%	52%	42%	52%	42%	52%	42%	52%	42%	52%
20	42%	52%	-	52%	42%	52%	-	52%	42%	52%	42%	52%
30	42%	52%	-	52%	42%	52%	-	52%	42%	52%	-	-
50	42%	-	-	-	42%	-	-	-	42%	-	-	-

2.3 Testing Rig and Shake-Table System

The tank was suspended in a testing rig fastened to the shake-table. Depicted in Figure 2.5, the unidirectional shake-table is bolted to a strong floor and has a surface area of 42ft^2 (3.9m^2). It is driven by an MTS 204.30 hydraulic actuator. The actuator is controlled by an MTS 407 Controller and powered through an MTS 448.16 Power Driver.

The testing rig was designed, considering the tank length and height, to be an overall 1.5m in height constructed of 3in (76.2mm) hollow structural steel sections, $\frac{3}{16}$" (4.7625mm) thick (CISC designation, HSS76x76x4.8). Inside, two platforms were hung by threaded rods with adjustable turnbuckles from corner plates bolted into the HSS. The top platform suspended the tank and the bottom platform suspended an equivalent "ballast" mass. Force transducers that were linked to the platform underside, as shown in Figure 2.5, measured the shear force that developed from the fluid sloshing motion.

In the northwest corner of the rig, two "dummy" force transducers (or load cells) were linked to the platforms undersides. One for the bottom platform and the other at the mid-height of the rig for the top platform, see Figure 2.5 (top). These three-point connections for each platform ensured that the platforms did not rotate in-plane and provided extra precautions in the unlikely event of a broken link to a force transducer. Negligible influence of the dummy connections was verified between the force transducers and accelerometer calibrated data.

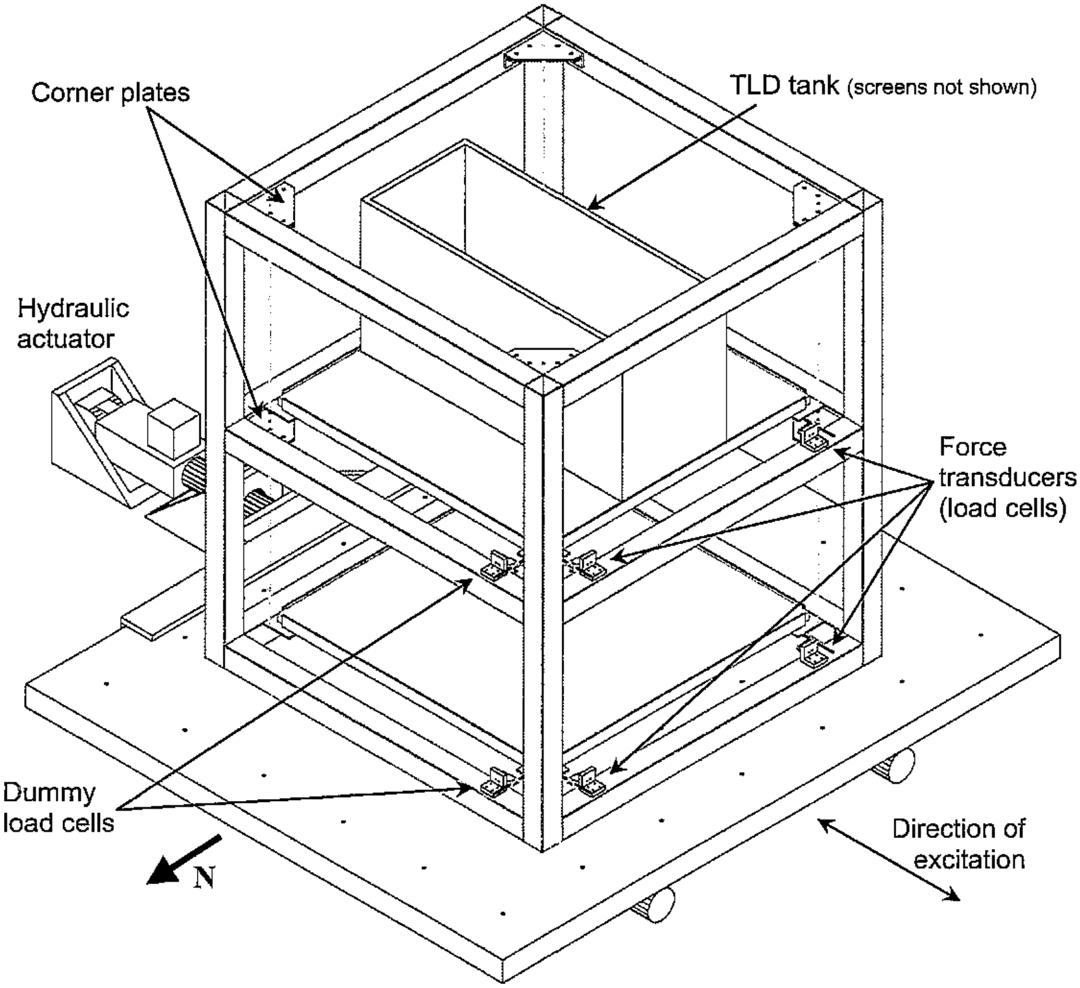

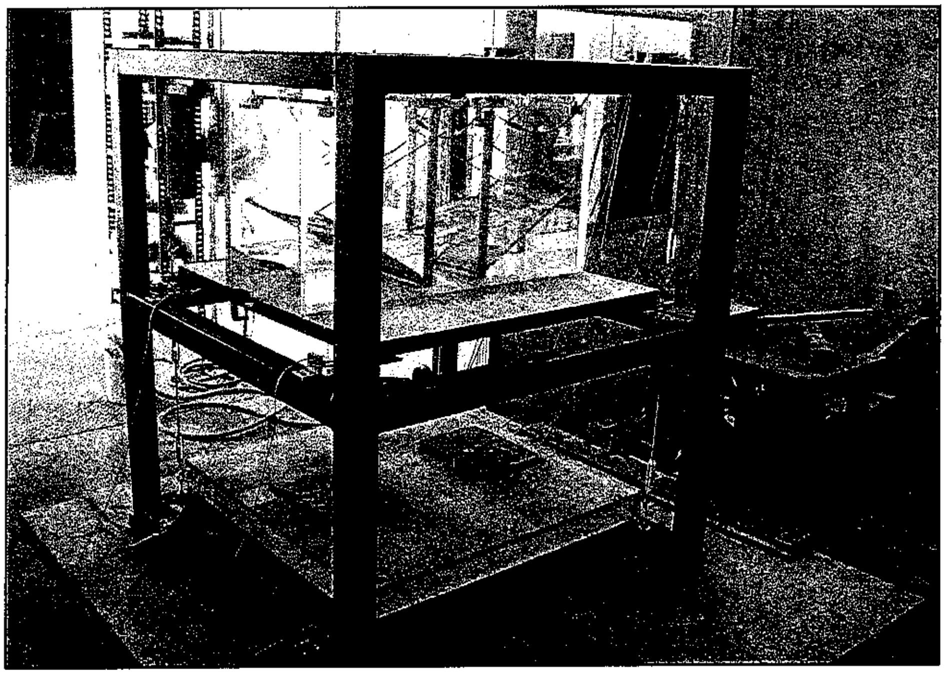

Figure 2.5. Testing rig on shake-table: schematic (top) & photo (bottom).

The primary function of constructing the testing rig with the double platform configuration was to measure the dynamic sloshing forces of the TLD. The top platform force transducers measured the inertial forces from the platform including the platform mass, tank mass, screen & frame mass, sloshing water mass, instrumentation mass, etc., while the bottom platform force transducers measured the inertial forces from the bottom platform, which included the platform mass and ballast mass. The ballast mass was selected such that the bottom platform mass plus the ballast mass equals all mass linked into platform force transducers above, including the still water mass. The additional experimental dynamic sloshing forces from the TLD, generated by the response of the liquid free-surface motion, were determined by subtracting the bottom force from the top force. Following Figure 2.6, the liquid sloshing forces, $F_{sw}(t)$, are

$$F_{sw}(t) = F_t(t) - F_b(t) \tag{2.2}$$

and the corresponding base shear forces, $F_w(t)$, which are the forces that the structure interacts with, were determined from

$$F_w(t) = F_t(t) - F_b(t) + F_c(t) \tag{2.3}$$

with $F_c(t)$ being the conservative force of the water mass.

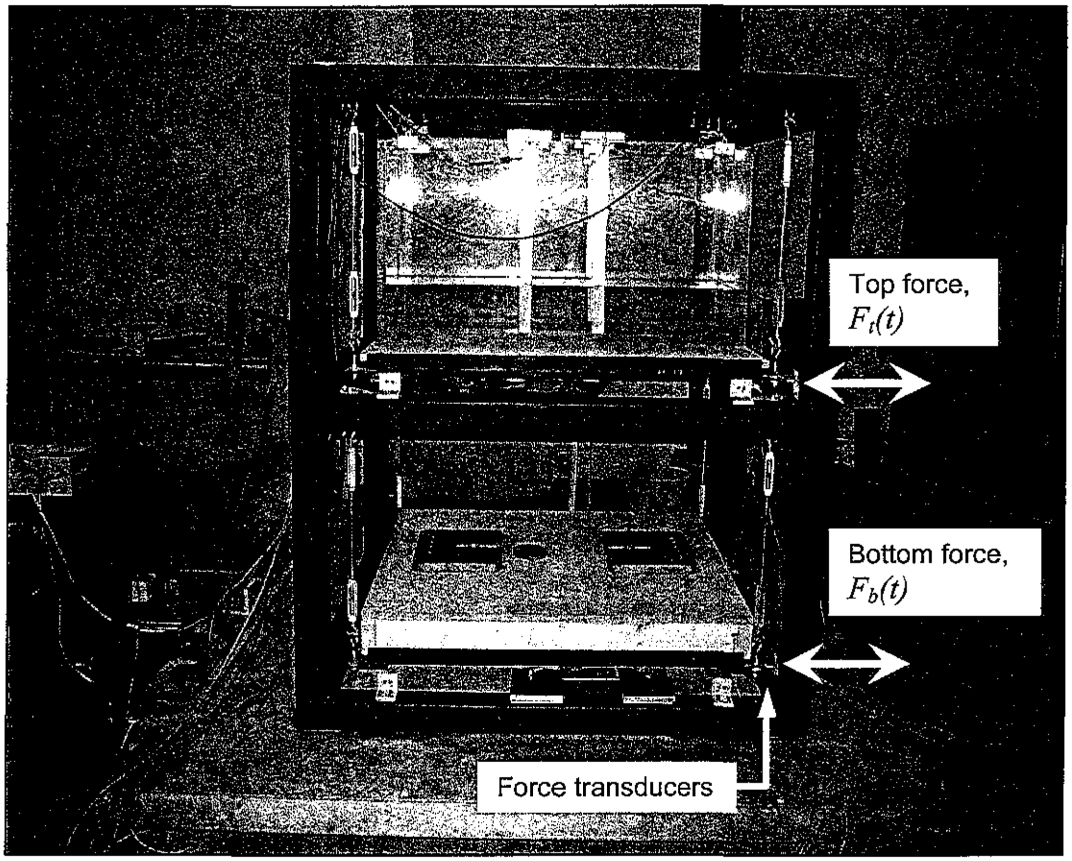

Figure 2.6. Side photo of testing rig on shake-table.

Since this is a dynamic system, the dynamic behaviour of the testing rig had to be predicted during the preliminary design stages to ensure its dynamic behaviour did not impinge on the frequency range of interest. SAP2000 was used to create a model of the testing rig and provide an estimate of the rig's fundamental natural frequency, which was found to be approximately 28.5Hz. Since the natural frequency of the sloshing fluid in the TLD tank was approximately 0.5Hz, the testing rig expected to have negligible influence over the range of excitation frequencies tested, which was confirmed after the rig was constructed.

2.4 Experimental Program

This section details the tools and instrumentation used to capture experimental data.

2.4.1 Instrumentation

The primary measurement of the experimental program was to capture the liquid sloshing force, F_{sw}, from the TLD. The load cells were linked to the platforms by #8-32 threaded rods. The threaded rod links had reduced diameters at two points designed to prevent overloading of the load cells.

Data was also acquired for the screen forces, wave heights, shake-table displacement, and shake-table acceleration. A component of this study was to capture all water forces onto the screens and to observe the variation of screen force with changing screen angle. The frames were bolted and hung from the load cells, which were connected from the top of the tank walls, as depicted in Figure 2.7.

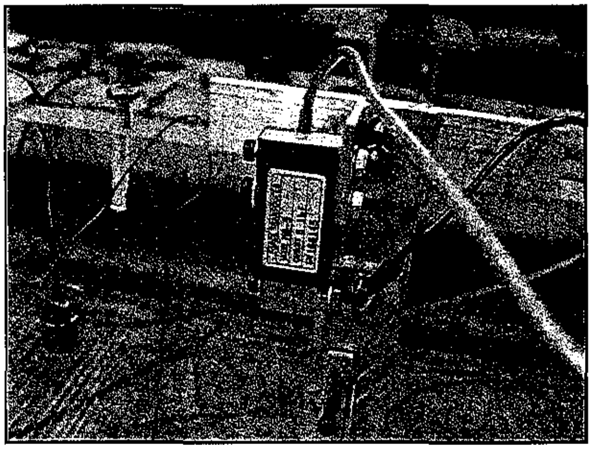

Figure 2.7. 5lbf (22.2N) Mini-Beam screen load cell.

The wave height was measured via wave probes consisting of capacitance-type bow-string sensors utilizing a taught loop of wire connected to an amplifier designed to convert the changes of capacitance to a measurable change in voltage.

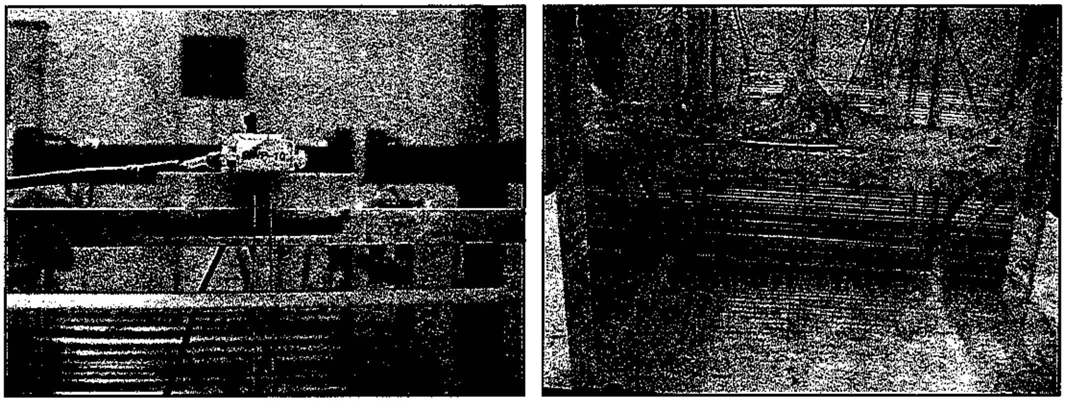

Figure 2.8. Wave Probe. Suspended over tank centreline (left) and in action (right).

Two wave probes were used to measure the wave height, η, at the ends of the tank. They were suspended at the tank centreline over the entire tank height and looped through a connection threaded into the bottom of the tank. Wave probes were only used at each end since the angled screens spanned throughout the rest of the tank length. The magnitude of the wave height at the end walls was found to be a good indicator of the level of response in the tank at a particular excitation amplitude. Also important for calculations and manipulation of data, the end wall wave height data can be used to predict the fluid velocity.

The shake-table displacement was measured by a stringpot attached from the solid actuator housing to the table. The stringpot data and the measured forces were used to generate energy dissipation or hysteresis graphs. For the final complete set of data used throughout the research, accelerometers were attached to the tank platform and the shake-table. The same subtraction scheme of §2.3

was used with the acceleration measured from the accelerometers to equivalently determine the ballast mass force, $F_b(t)$.

2.4.2 Data Acquisition

Two *data acquisition* (DAQ) systems were employed for capturing the experimental data. The first DAQ system used a DAQ program developed for this study in LabView 7.1, which included real-time displays of calibrated force time histories (Equation (2.2) or (2.3)) and force-displacement loops. The second used a supplied DAQ program from IMC DataWorks, Inc. Honeywell bridge amplifiers were used to amplify and filter the incoming signals.

2.4.3 Filtering

A *filter frequency-response* (FFR) test was conducted to determine a lower filtering frequency than provided by the bridge amplifiers for the digital filters in the DAQ systems. Low-pass digital filters were set at 5Hz accordingly, where the actual cut-off frequency remained well above the TLD resonant sloshing frequency and the entire range of frequencies tested, which were up to approximately 1Hz. A *power spectral density* (PSD) analysis also confirmed that the dynamic response of the complete test setup, measured through all instrumentation, did not impinge on experimental performance.

2.5 Summary

The core test specimen included: a 1.5m high testing rig constructed of HSS76x76x4.8 steel sections supporting an acrylic TLD tank, which was equipped with hinged stainless steel horizontal-slat screens.

The experimental program for this thesis has been described in this chapter, including the rationale for the design and construction of all test specimens as well as the use of data instrumentation and acquisition.

CHAPTER 3: EXPERIMENTAL PERFORMANCE OF SYMMETRIC FIXED-ANGLE HORIZONTAL-SLAT SCREENS IN A TUNED LIQUID DAMPER

3.1 Introduction

This chapter reports the results obtained from experimental tests conducted to investigate the effect of symmetrically-angled horizontal-slat screens on the dynamic response behaviour of a *tuned liquid damper* (TLD). Frequency-response curves, time histories, and force-displacement hysteresis loops are presented. Tests are conducted at five different screen angles (as described in Chapter 2) to determine the impact of free-surface response with increasing screen angle. The screens are held statically at a predetermined angle of inclination and, therefore, their angle (or pressure-drop) is not continuously varying in a passive or real-time controlled fashion. This configuration permits a viable study of the effect of angled screens—as opposed to an oscillating configuration—that will be compared to simulations in Chapter 4. The effect of excitation amplitude, screen angle, and screen solidity ratio shall be considered in this chapter.

3.2 Experimental Nomenclature

The following experimental nomenclature utilized throughout all experimental results presented in this thesis is introduced here:

- Non-dimensional free-surface response amplitude, η',

$$\eta' = \frac{\eta}{h} \tag{3.1}$$

where η is the free-surface response amplitude (h defined earlier in Figure 2.1).

- Non-dimensional excitation amplitude, Λ,

$$\Lambda = \frac{A}{L} \tag{3.2}$$

- Excitation frequency ratio, β,

$$\beta = \frac{f}{f_n} \tag{3.3}$$

where $f_n = \omega_n/2\pi$ is the natural sloshing frequency (in Hz) and $f = \omega/2\pi$ is the forcing frequency of the input base excitation to the TLD. Inversely, ω is the radial frequency, $\omega = 2\pi f$.

- Non-dimensional base shear force, $F_w'(t)$,

$$F_w'(t) = \frac{F_w(t)}{m_w A\omega^2} \tag{3.4}$$

where $F_w(t)$ is the measured base shear force that the fluid motion produces, see Equation (2.3). The denominator in Equation (3.4) is the maximum inertial force of the entire water mass, m_w, treated as a solid mass.

- Non-dimensional energy dissipation per cycle, E_w',

$$E_w' = \frac{E_w}{\frac{1}{2} m_w \left(A\omega\right)^2} \tag{3.5}$$

where the denominator is the maximum kinetic energy of the entire water mass treated as a solid mass and in the numerator,

$$E_w = \oint_T F_w(t)\,dx \tag{3.6}$$

is the energy dissipated per cycle.

3.3 Relationship Between Free-Surface Response, Force, and Energy

This initial section details the overall response of the TLD equipped with the symmetrically angled damping screens. The primary response of a traditional *tuned mass damper* (TMD) is the relative motion between the primary structure and the damper induced by external forces on the structure. The resultant damper force is the inertial force of the accelerating mass of the TMD. A TLD has a fixed base inside the primary structure. The primary response of a TLD is the motion of fluid with the amplitude of vertical displacement of the liquid free-surface denoted by, η. The resultant damper force, $F_w(t)$, is the dynamic liquid sloshing forces, $F_{sw}(t)$, generated by the free-surface motion, $\eta(t)$, plus conservative forces (contribution of water mass). The corresponding energy, E_w, over a period of excitation can be determined as in Equation (3.6). This first section of the experimental results demonstrates these various responses of the TLD.

3.3.1 TLD Equipped with Symmetrically Inclined Screens

Figure 3.1 through Figure 3.3 are the non-dimensional fundamental amplitudes (maximums) of the free-surface response measured near the tank end wall (at $0.05L$ & $0.95L$), η', the corresponding dynamic (non-conservative) sloshing force as a result of the free-surface response, F_{sw}', the base shear (damper) force including conservative forces, F_w', and the energy per cycle, E_w', plotted in the frequency domain. The *fundamental* response is extracted by digitally filtering the higher harmonics of the non-linear response in post-processing. Non-dimensional amplitudes of excitation, Λ = 0.005, 0.010, and 0.021, and screen angles, $\theta = 0°$, 30°, and 60°, are plotted representing the range of excitation amplitudes and extent of screen angles tested, for both sets of screens, 42% and 52% nominal solidity, S_n.

Since the dynamic sloshing force, F_{sw}', is generated from the fluid motion with free-surface response amplitude, η', their peak amplitudes occur at the same β. These peaks can be seen in the frequency-response plots in Figure 3.1 through Figure 3.3. The base shear force, F_w', peaks at lower β values than the peak of η' and F_{sw}' due to the addition of the inertial component of the water mass and crosses the F_{sw}' curve near its peak response where the dynamic resonant response is greatest. The peak frequency (peak β) of energy, E_w', corresponds to the peak frequencies of the dynamic components of fluid response, η' and F_{sw}'. For example, for S_n = 42% and Λ = 0.005 in Figure 3.2, at $\theta = 0°$ and 30° the peaks of η' and F_{sw}' are at $\beta \approx 1.00$. For $\theta = 60°$ the peaks shift slightly to the right at $\beta \approx 1.02$. These values of β for each screen angle can be seen in the corresponding E_w' plot in the same figure, especially noting the slightly increased β for $\theta = 60°$.

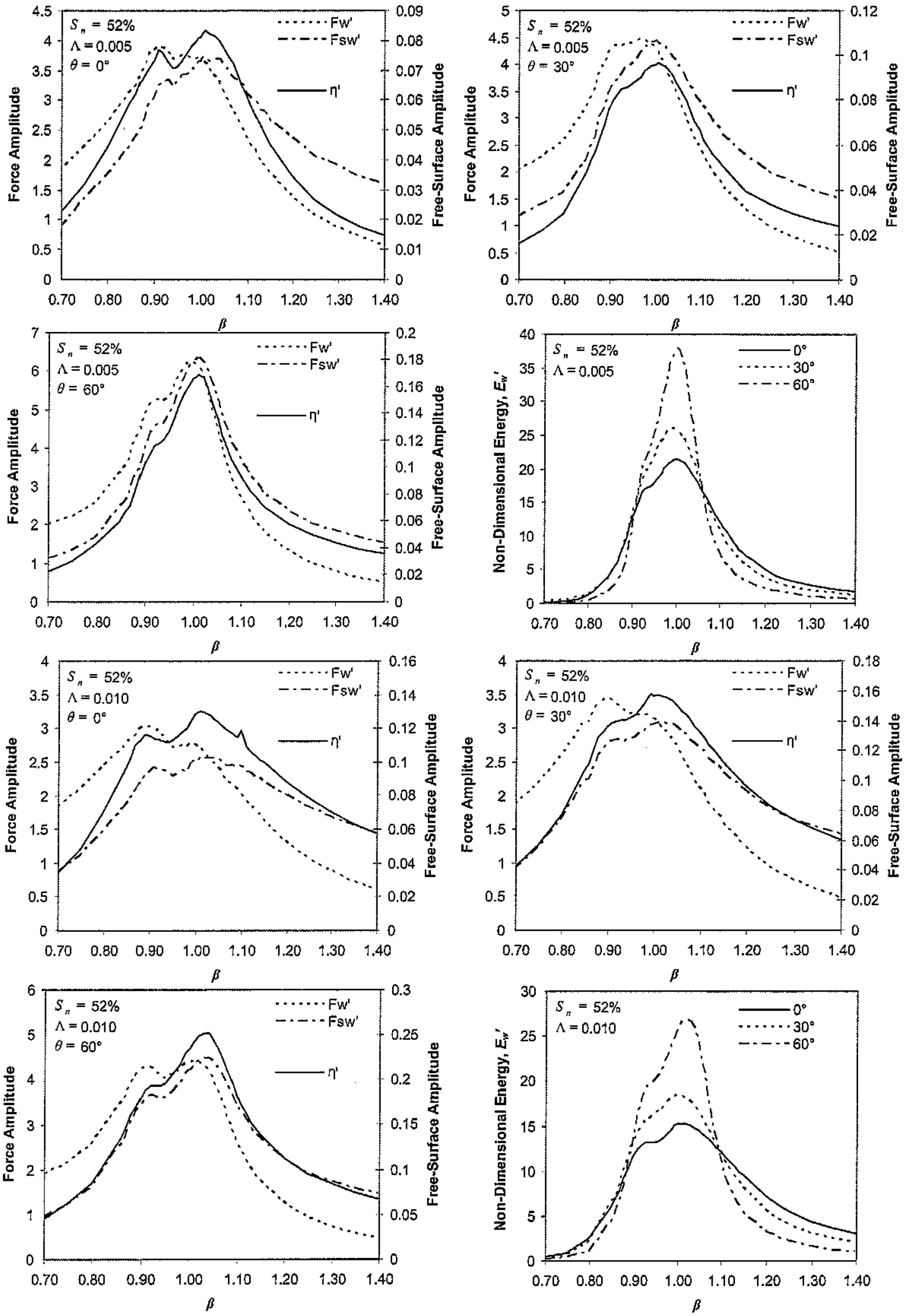

Figure 3.1. Fundamental frequency-response of free-surface, forces, and energy.

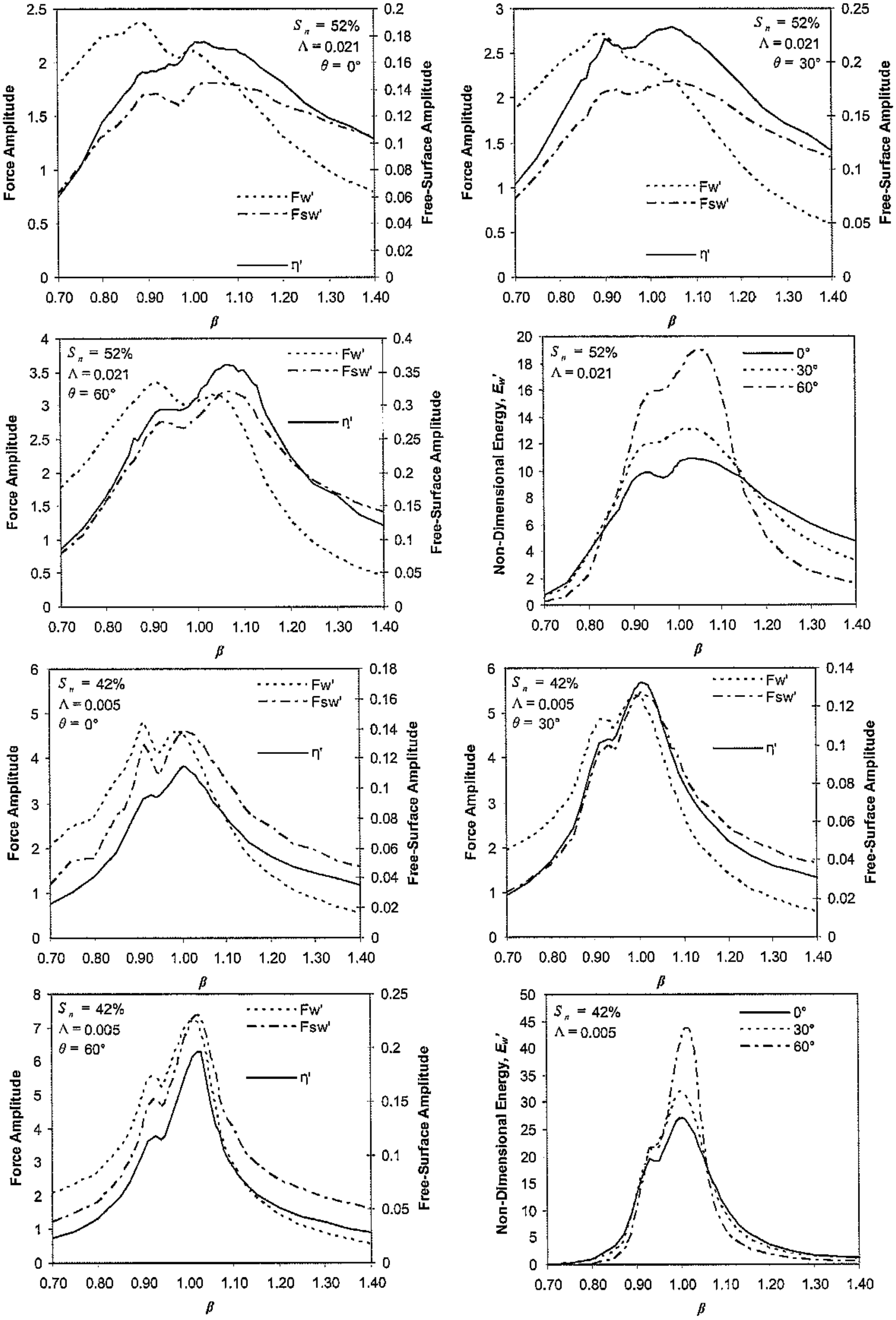

Figure 3.2. Fundamental frequency-response of free-surface, forces, and energy (continued).

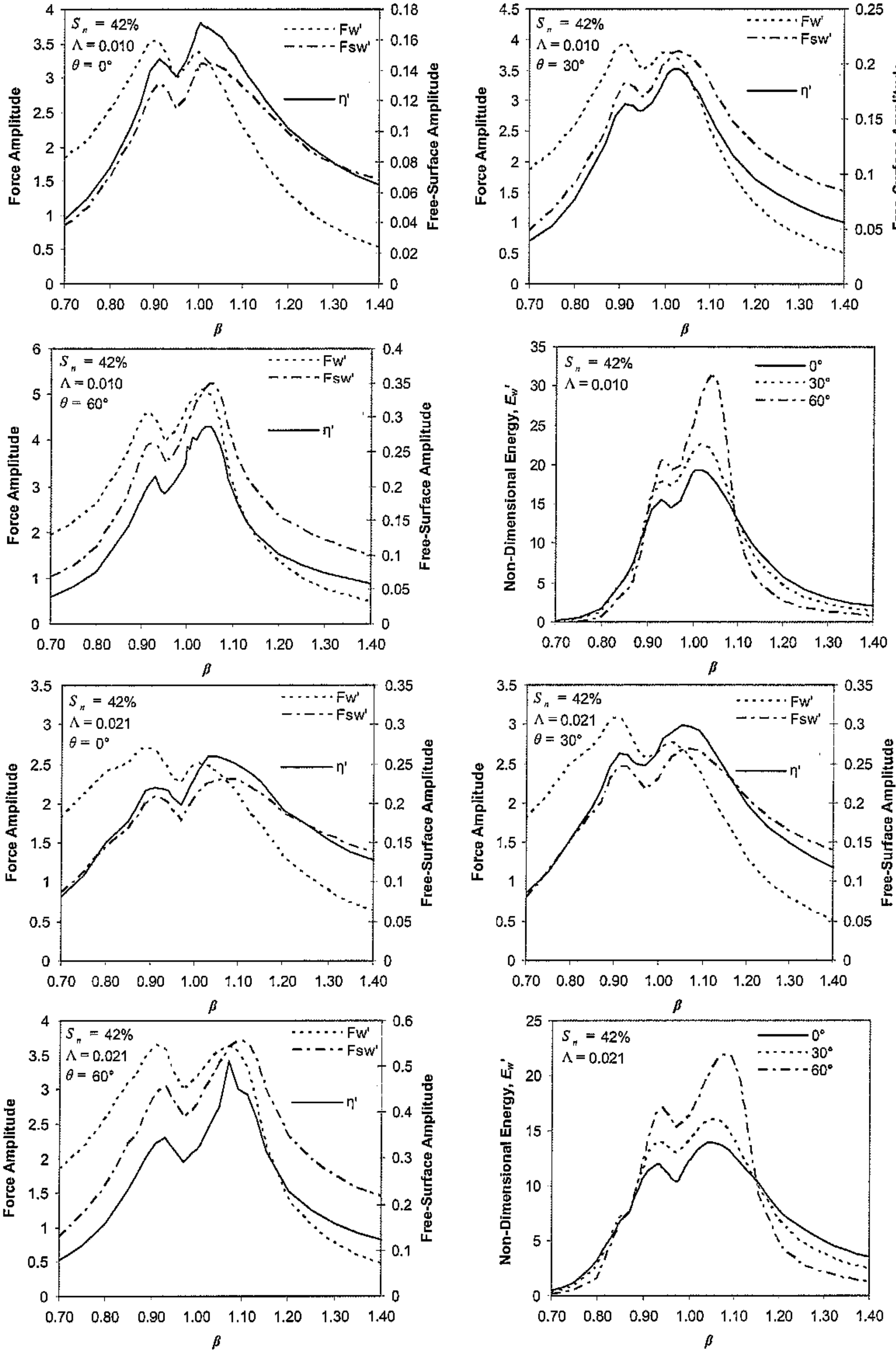

Figure 3.3. Fundamental frequency-response of free-surface, forces, and energy (continued).

It can be observed (especially in the β-E_w' plots) that symmetrically angled screens exhibit a small frequency-hardening behaviour (peak-frequency shifting) up to a very high angle of 60° (for $h/L = 0.123$); the importance of this finding shall be addressed throughout this thesis.

From Figure 3.1 and Figure 3.2, the following observations with respect to the free-surface response can be made. For $\Lambda = 0.005$, as the screens are rotated from $\theta = 0°$ to 60° the peak η' value approximately doubles in amplitude indicating a reduction in the damping provided by the screens. The same trend can be found for all three amplitudes for each screen solidity. For $S_n = 52\%$, $\Lambda = 0.005$ at $\theta = 60°$ and $\Lambda = 0.021$ at $\theta = 0°$ (4 times excitation amplitude), the free-surface peak amplitudes are approximately the same, this indicates that adjusting θ permits the maximum response amplitude of the free-surface to be held nearly constant over a range of excitation amplitudes. Therefore, it can be concluded that the level of damping can be adjusted to control the TLD response over a range of excitation amplitudes.

From Figure 3.2 and Figure 3.3, for $S_n = 42\%$, $\Lambda = 0.005$ at $\theta = 60°$ and $\Lambda = 0.010$ at $\theta = 0°$, it can be seen that although η' for $\Lambda = 0.010$ is less than that of $\Lambda = 0.005$, the multi-peak response is more pronounced due to the non-linear response behaviour of the sloshing fluid.

The energy dissipation, E_w', plots from Figure 3.1 through Figure 3.3 for both screens clearly indicate the increased response, which results in increased E_w', due to adjusting the screen angle, θ.

3.3.2 TLD Without Damping Screens

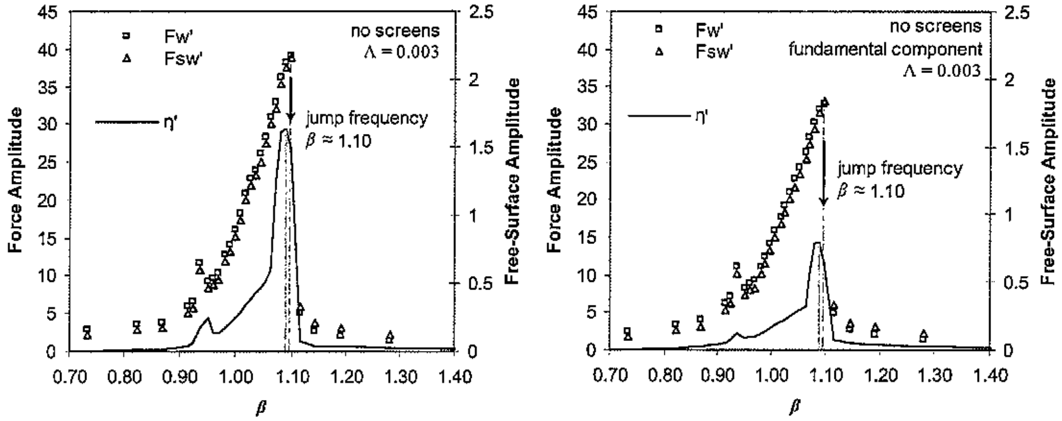

Figure 3.4. Frequency-Response with no screens (forward sweep). Filtered 1^{st}-mode (right).

The influence of screens can be contrasted with Figure 3.4 that shows the frequency-response of the tank with no screens. Figure 3.4 shows the frequency-response of F_w', F_{sw}', and η' for the smallest amplitude of excitation tested in this study, $\Lambda = 0.003$ ($A = 2.5$mm), including the fundamental response. This figure shows the effect of damping screens on reducing the free-surface response and dissipating energy (contrasted with Figure 3.1 through Figure 3.3). It can be noted that for small Λ the peak response is found to occur at $\beta \approx 1.10$ indicating significant hardening at low Λ. In addition, a jump frequency phenomenon (Reed et al. 1998) is also found to occur with no screens present. This jump

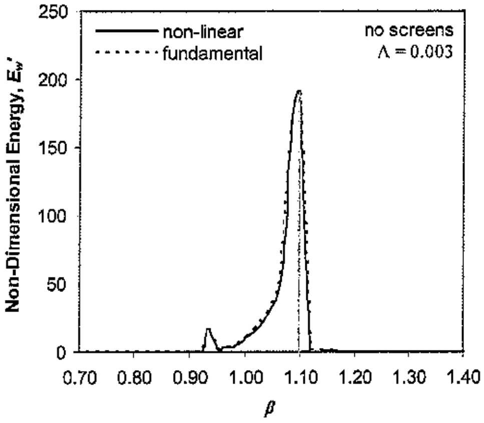

Figure 3.5. Energy dissipation of TLD with no screens.

frequency does not occur when the screens are inserted in the tank. The significantly larger normalized energy, E_w', plotted in Figure 3.5 compared to those found in Figure 3.1 through Figure 3.3 can be attributed to the negligible damping found in the fluid alone as mentioned in Chapter 1. Damping screens provide a significant and often required amount of inherent TLD damping, ζ_a.

3.4 Phase Angle

Figure 3.6 shows the phase angle for the tank end wall free-surface amplitude, η', for both sets of screens at amplitudes of excitation, Λ = 0.005, 0.010, and 0.021, and screen angles, $\theta = 0°$, 30°, and 60°. For increasing Λ, a hardening behaviour is indicated by a shifting phase angle ($\varphi = 90°$) to a higher peak frequency than the linear $\beta = 1.00$ (theoretical). The increased amount of damping, ζ_a, provided by the screens due to increasing Λ can be seen by the clockwise rotation of the curves over increasing excitation amplitudes. Note that only at high screen angles, $\theta \approx 60°$, does the value of β at $\varphi = 90°$ display a slight increase of no more than approximately 3% of the β value for $\theta = 0°$.

The peak E_w' value can be used to determine the resonant sloshing frequency instead of using the phase angle, φ, from η' or F_{sw}'. It is for this reason that the principal descriptor used in this thesis to describe the response of the TLD will be the energy, E_w'. In addition, a change in peak E_w' indicates a change in TLD damping, ζ_a. Therefore, E_w' shall be used to evaluate and compare the response behaviour of the TLD.

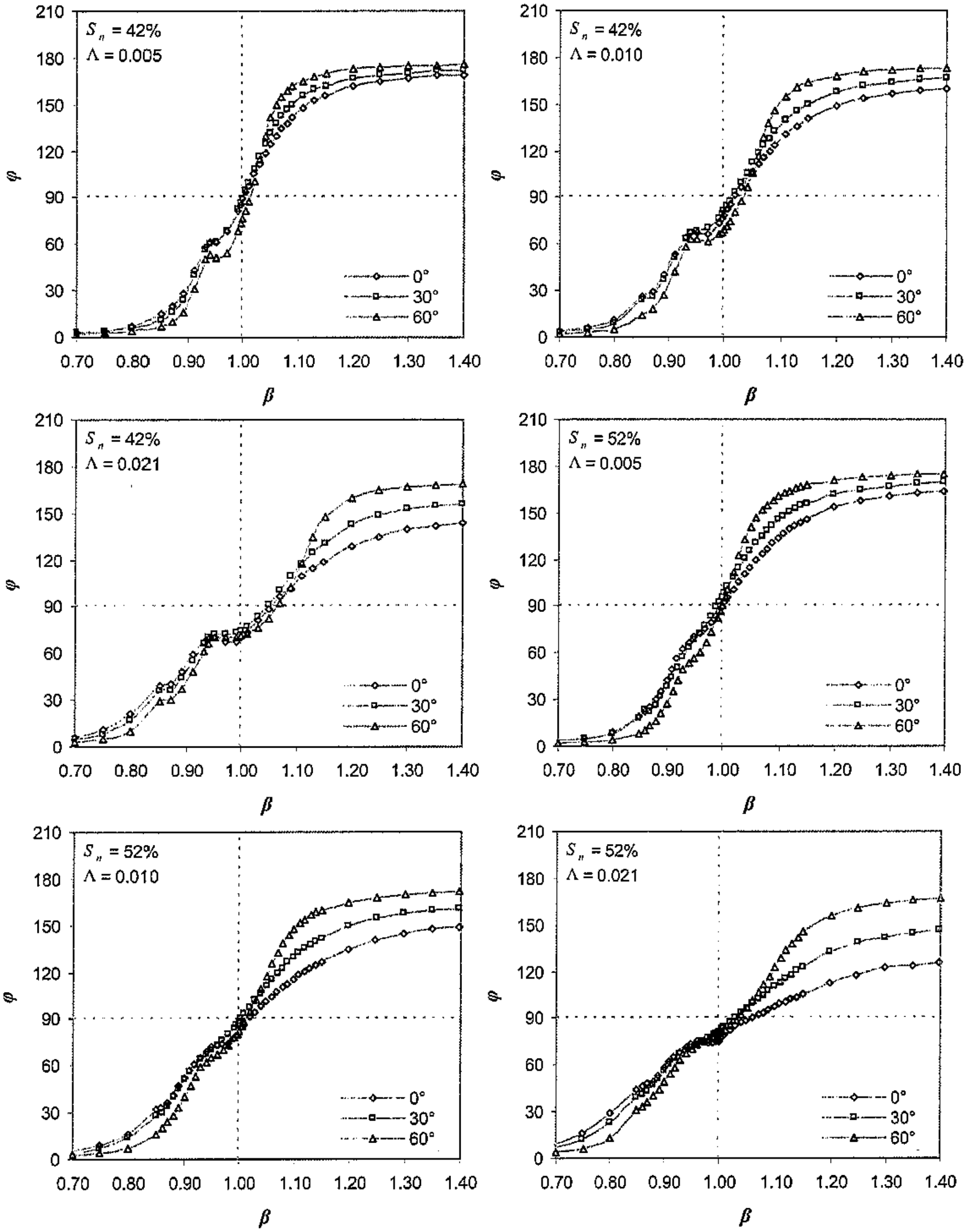

Figure 3.6. Phase angles for tank end wall η' at various screen angles.

3.5 Amplitude-Dependency of a TLD

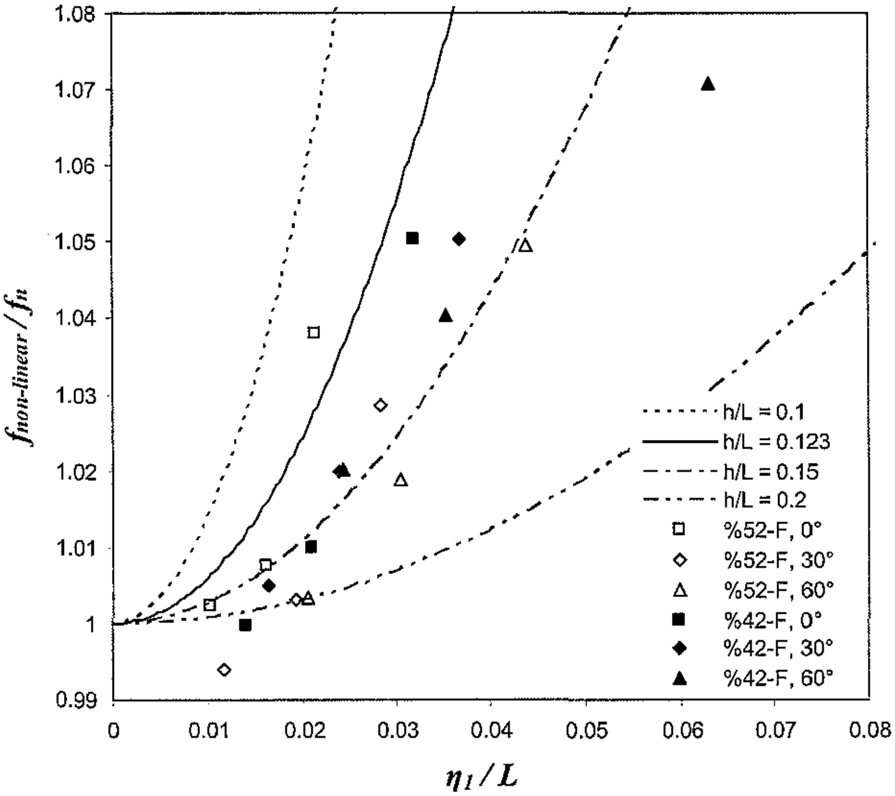

Figure 3.7. Non-Linear peak natural frequency versus η_1/L.

The fundamental sloshing frequency for the tank used in this study and dimensions given in Figure 2.1, expressed in Hertz is, f_n = 0.546Hz. However, the amplitude-dependent nature of the TLD is well described by the following equation from Bauer (1969),

$$\frac{f_{non-linear}}{f_n} = 1 + \frac{\pi^2}{64}\left(\frac{\eta_1}{L}\right)^2 \left(9\tanh^{-4}\frac{\pi h}{L} - 12\tanh^{-2}\frac{\pi h}{L} - 2\tanh^2\frac{\pi h}{L} - 5\right) \quad (3.7)$$

where $f_{non-linear}$ is the resonant non-linear frequency, dependent on the amplitude of fundamental free-surface response, η_1.

Equation (3.7) is plotted at various h/L values over the free-surface amplitude normalized by the tank length in Figure 3.7. Equation (3.7) with h/L = 0.123 used in this study is also plotted in the figure. The resonant frequency values and corresponding fundamental free-surface amplitudes, η_1, are also plotted in Figure 3.7 for both sets of screens at various inclinations for various excitation amplitudes.

Figure 3.7 shows the amplitude-dependent hardening behaviour of the TLD. For both screen solidities the hardening behaviour is generally found to reduce with increasing screen angle. This is particularly evident for the 52% screen solidity ratio. It is postulated that this would improve the performance of a TLD as the tuning ratio between the damper and the structure would be maintained over a larger range of structural response amplitudes.

3.6 The Effect of Screen Inclination on E_w'

This section concentrates on the change in non-dimensional energy dissipation, E_w', with screen angle (see Figure 2.4 (left)). Figure 3.8 and Figure 3.9 are energy dissipation frequency-response curves showing the effect of angled screens in a tuned liquid damper, with Figure 3.8 showing results from the 42% screen tests and Figure 3.9 showing those from the 52% screen tests. Both figures include families of curves for differing screen angles, θ, covering a range of excitation amplitudes. Lower excitation amplitudes, 2.5mm, 5mm, and 10mm, are representative of *root-mean-square* (RMS) wind-induced structural response levels. The lower excitation amplitudes correspond to expected serviceability level motions. The inherent TLD damping, ζ_a, resulting from the screens is typically evaluated in this excitation range. The larger excitation amplitude of $A = 20$mm ($\Lambda = 0.021$) represents the expected response behaviour for larger return periods. Larger normalized excitation amplitudes, including $\Lambda = 0.021$, correspond to peak structural response amplitudes. Design forces including TLD base shear forces, $F_w(t)$, and screen forces are typically estimated from these tests. $\Lambda = 0.021$ was also chosen so that comparisons can be drawn between the peak excitation amplitude of the oscillating screens results of Chapter 5.

Figure 3.8 and Figure 3.9 clearly show that screen angle directly affects the normalized energy dissipated by the TLD. This is demonstrated by the change in the frequency-response curves, for a particular Λ, where the level of non-dimensional energy dissipation, E_w', is found to increase with increasing screen angle, θ, for both S_n. The increasing height and decreasing width of E_w' can be attributed to the effect of the change in the damping, ζ_a, due to the angled screens. With increasing screen angle there is a decrease in TLD damping, which is a result of the change in the pressure-loss coefficient, C_θ. The pressure-loss coefficient decreases with increasing screen angle, which correspondingly reduces the damping provided by the screens. This decrease in TLD damping, due to the increased screen angle, results in larger sloshing water response, larger wave heights, larger base shear force (recall Figure 3.1 through Figure 3.3), and increased E_w'—clearly evident in Figure 3.8 and Figure 3.9.

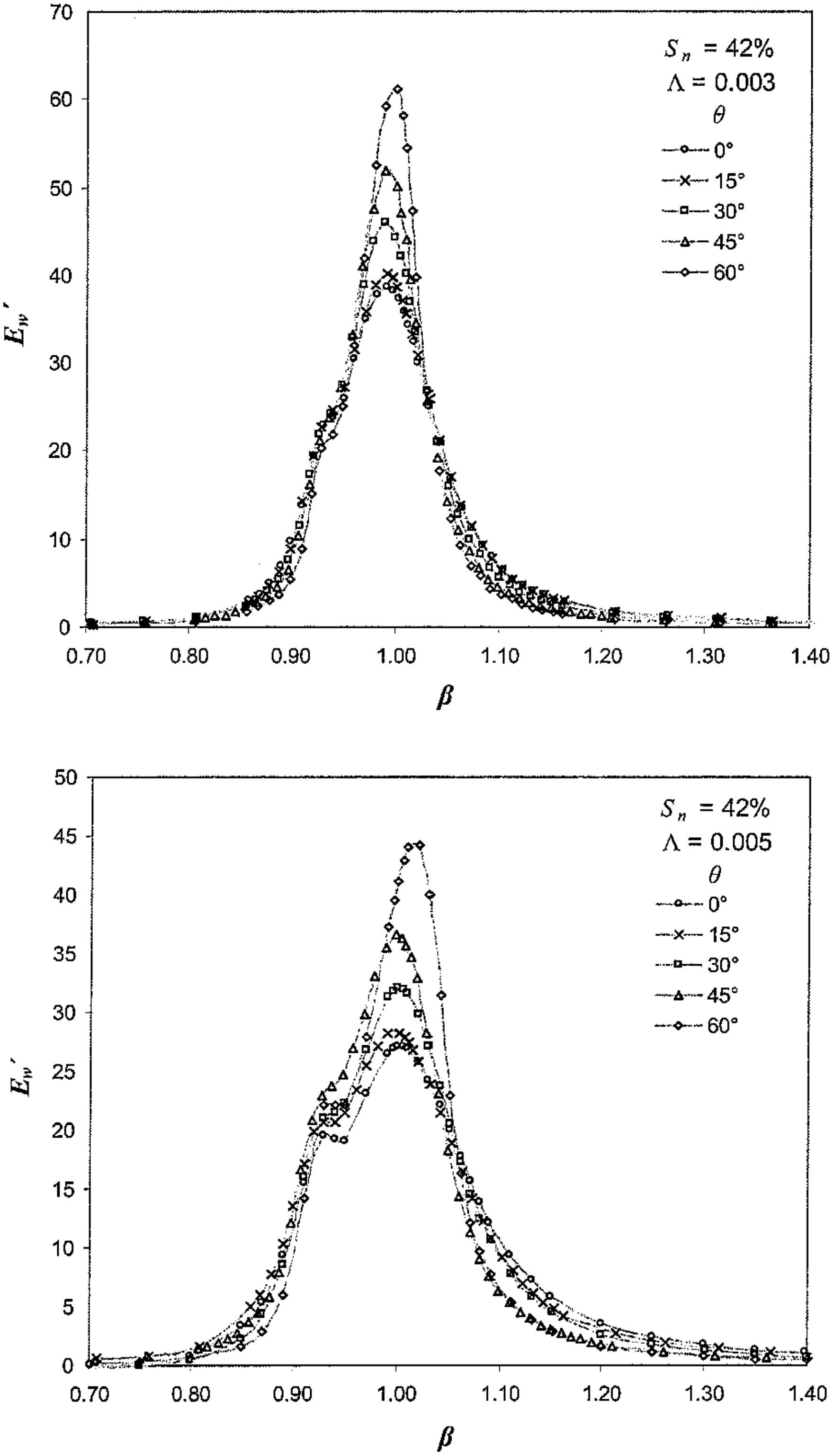

Figure 3.8. Experimental non-dimensional energy results over θ, 42% screens.

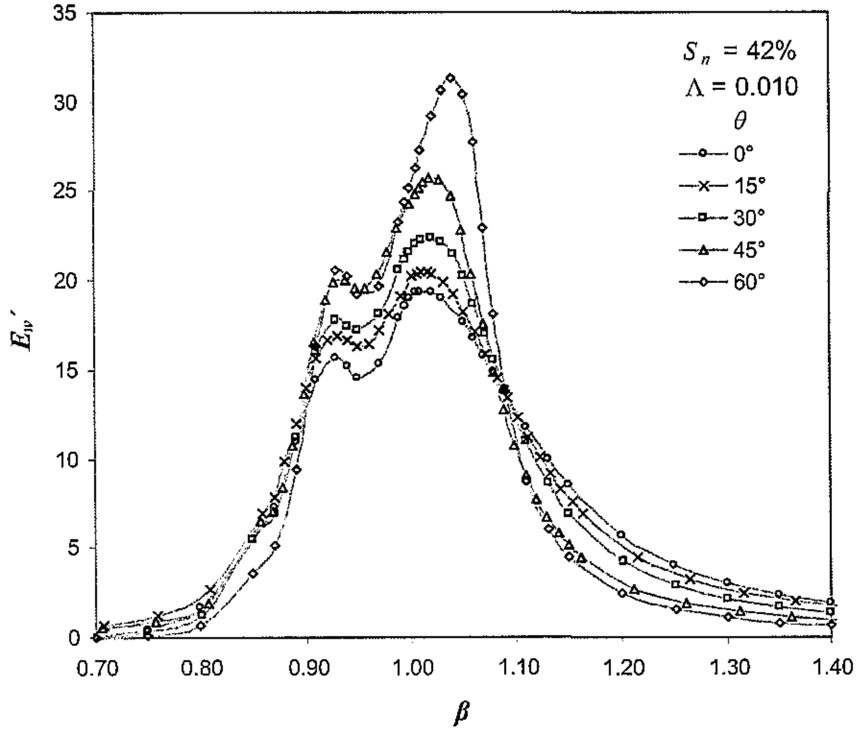

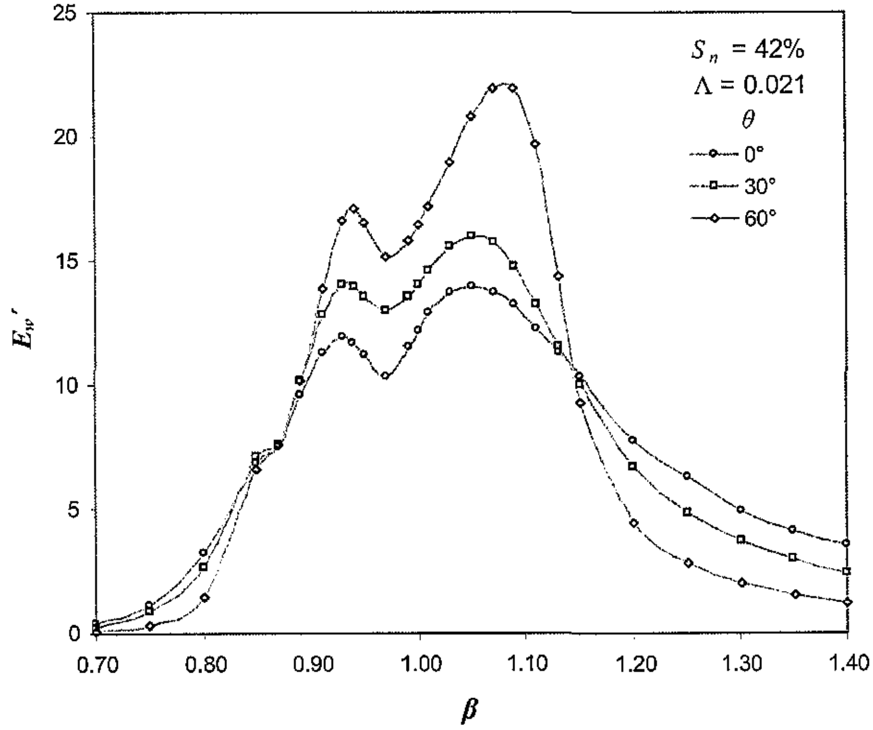

Figure 3.8 (continued)

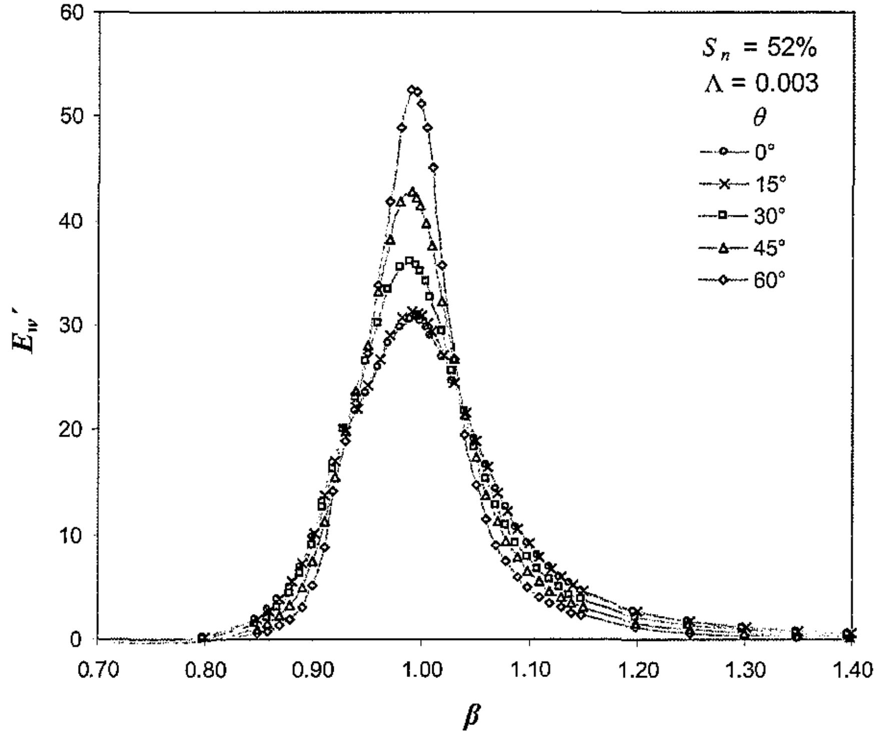

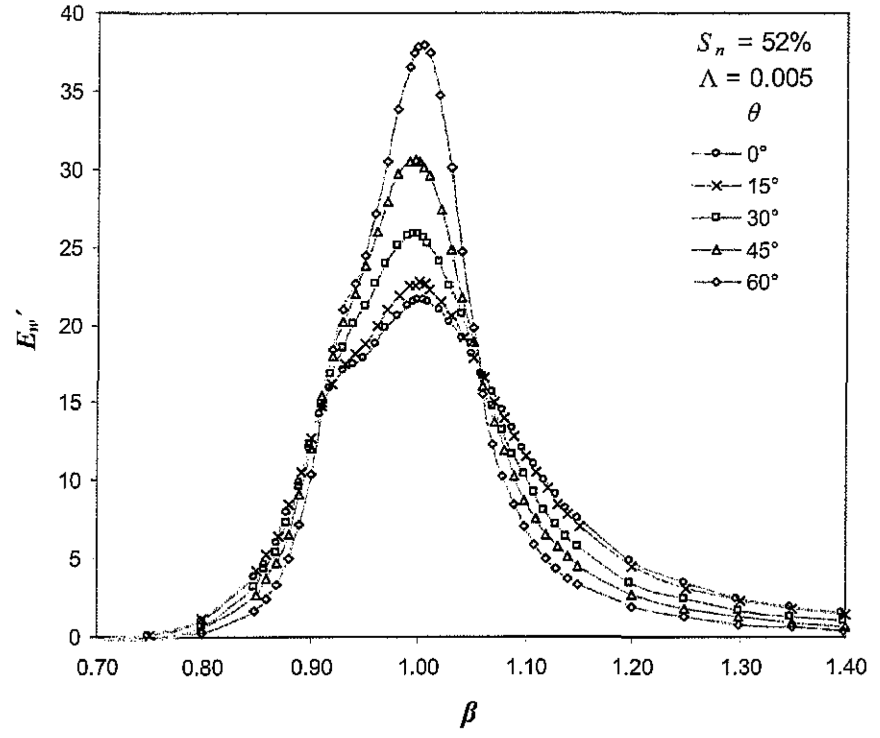

Figure 3.9. Experimental non-dimensional energy results over θ, 52% screens.

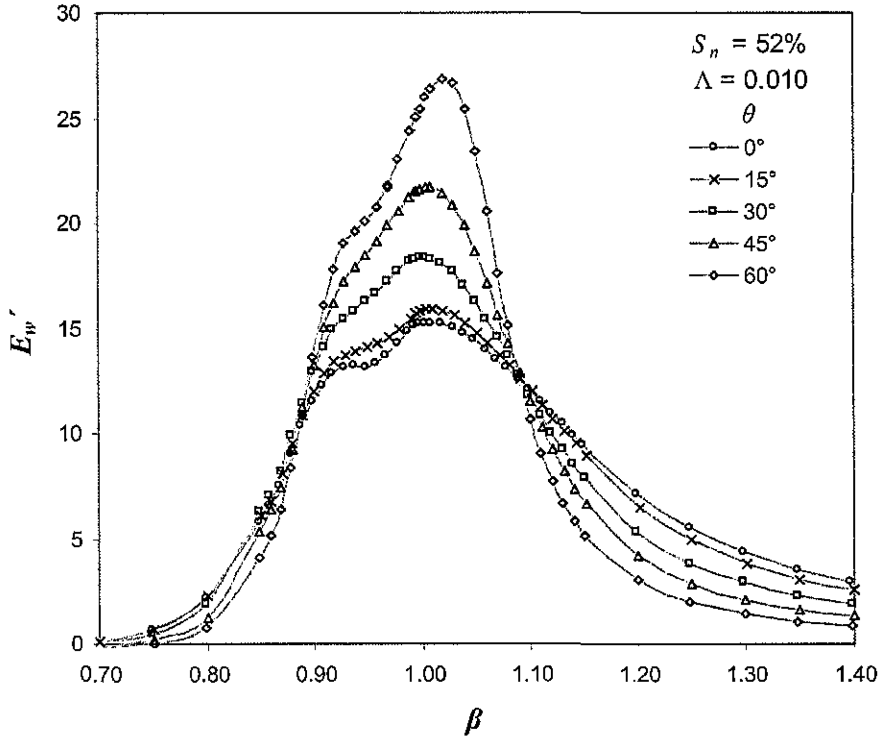

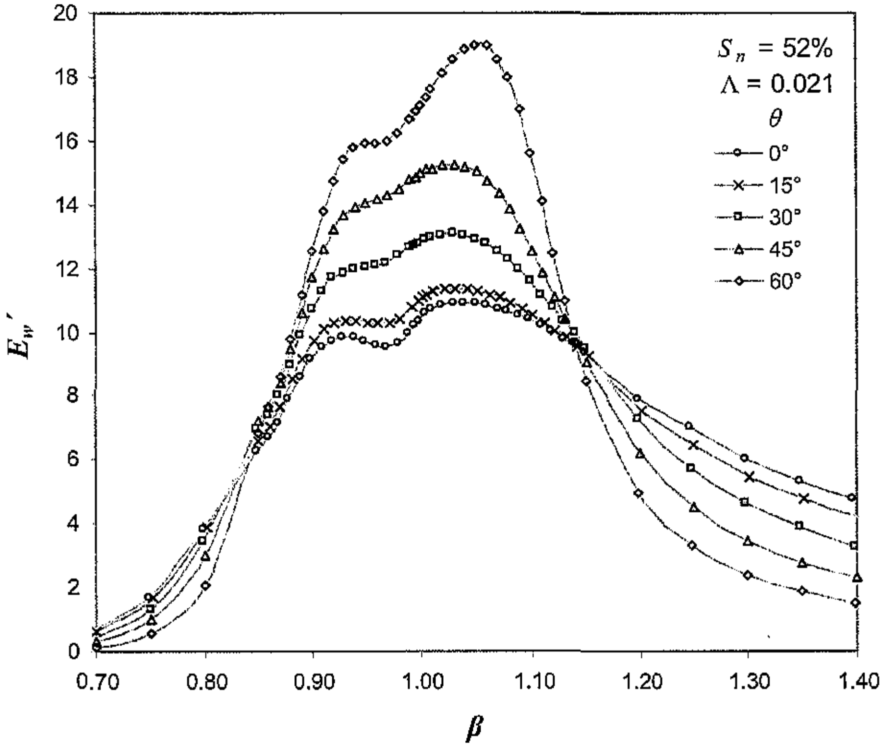

Figure 3.9 (continued)

It is observed that the percentage increase in non-dimensional energy dissipation with each increase in screen angle is relatively consistent throughout the range of amplitudes tested, $0.003 \leq \Lambda \leq 0.031$. For the 42% screens, for example, the percentage increase at peak E_w' from the 0° peak for 30° and 60° is 15-18% and 60-63%, respectively. Similarly for the 52% screens, the percentage increase at peak E_w' is 18-21% and 73-76% for 30° and 60°, respectively. The E_w' increase due to θ was found to be higher for the 52% screens than that of the 42% screens.

An interesting observation from these experimental results (Figure 3.8 and Figure 3.9) was the fact that a peak frequency shift was observed only to occur at the 60° screen angle for $0.003 \leq \Lambda \leq 0.031$. The percentage increase of peak frequency was 1-3% at 60° for the previous values of Λ, calculated between the peak frequencies of the angled arrangement versus the vertical screen configuration. This negligible shift in peak frequency—especially for $\theta \leq 45°$—will have an effect on the ability of a TLD equipped with angled screens (as in this chapter) to remain tuned to the target tuning frequency, which is typically at or very close to the natural sloshing frequency, f_n, at $\beta = 1.00$. The importance of maintaining the tuning ratio between the TLD and a structure for performance and efficiency issues shall be addressed in a later chapter and the impact of the findings here will be assessed.

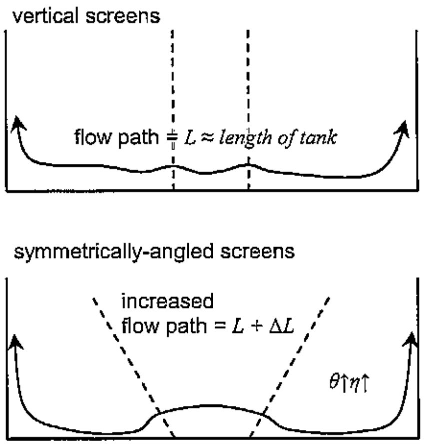

Figure 3.10. Effect of inclined screens on sloshing frequency.

The reduced shift in the peak frequency may be attributed to an increased flow path of the fluid in the tank. Figure 3.10 shows a plausible depiction of the increased fluid particle travel inside the tank when the screens are symmetrically angled. Examining the sloshing frequency of Equation (4.39), fundamental with $n = 1$, it is reasonable to postulate that the increased flow path with symmetrically angled screens, $L + \Delta L$, may aid in reducing the hardening behaviour.

3.7 Selection of Solidity Ratios

This section focuses on the rationale for the selection of the two sets of screen types defined by their solidity. The 42% screens were selected as a benchmark as numerous experimental studies have been conducted using screens with a similar solidity (Tait 2004, Yeh and Shrestha 1989, Baines and Peterson 1951). One of the main goals of this study is to demonstrate replacing a single set of vertical screens with a set of screens that can be inclined such that they can be designed for a particular level of excitation, oriented vertically (0°), and adjust to a different angle to mimic the damping of the original vertical-only screens, through a range of excitation amplitudes. A screen angle of approximately 45°

was selected to be the target screen angle in which to determine the selection of a second set of screens and their solidity (by matching peak E_w'). Using initial experimental data from the 42% angled screens tests and the observed percentage increase in peak energy dissipation (as discussed in the previous section), simulations were carried out with higher solidities using the initially developed shallow water wave theory program described later in §4.4. This program was used to determine the peak of E_w' at an angle between 40-50° that would match the peak of E_w' for the vertical 42% solidity (at $\theta = 0°$). The $S_n = 52\%$ nominal solidity was determined accordingly. Experimentally this solidity was found to be suitable and results for $S_n = 42\%$ at $\theta = 0°$ and $S_n = 52\%$ at $\theta = 45°$ are shown in Figure 3.11 to confirm the selection process. From Figure 3.11 it can be seen that for a particular excitation amplitude the peak E_w' values for the 52% screens inclined at $\theta = 45°$ are approximately 20% larger than the peak E_w' values for the vertically oriented (0°) 42% screens. Therefore, the curves shown in Figure 3.11 indicate that the damping provided by the 42% screens at 0° is similar to that of the 52% screens at 45°. It is expected that at an angle slightly less than 45° the E_w' (and ζ_a) values for the 52% screens would match the E_w' (and ζ_a) values for the 42% screens at 0°.

Results from Figure 3.11 indicate that η' for a particular Λ will be larger for $S_n = 52\%$ at $\theta = 45°$ than $S_n = 42\%$ at $\theta = 0°$. However, the value of the frequency at peak E_w' is less than that of $S_n = 42\%$. This behaviour is postulated as being attributed to an increased flow path indicated previously (Figure 3.10).

Increased non-linear response behaviour with lower screen solidity is also evident in Figure 3.11 by the difference in the multiple-peak response between the 52% and 42% screens. The higher solidity screens (S_n = 52% at θ = 45°) results in a more predominant single-peak response compared to the more double-peak behaviour of the TLD equipped with lower solidity screens, with the first peak around β = 0.94. This is also evident when comparing the differences in the multiple-peaked frequency-response curves shown in Figure 3.8 and Figure 3.9. Examination of Figure 3.9 reveals that screen angle also suppresses the higher harmonics (and corresponding multiple peak response). The multiple-peak response is least apparent at 30°-45°, which is also observed in Figure 3.11 versus

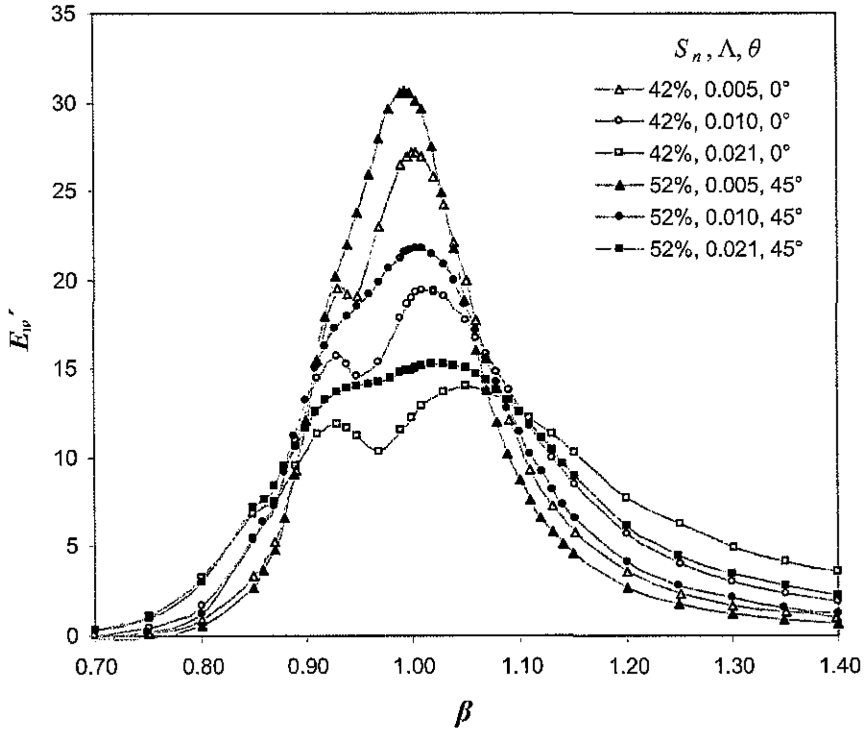

Figure 3.11. Frequency-Response revealing choice scheme between solidities.

the 42% screens at 0°. The span along the length of the tank of the screens (location) from $\theta = 30°$ to 45° indicate that these angles aid in suppressing the response of higher harmonics as well, considering the parametric study on screen location conducted by Tait (2004). The effectiveness of a damping screen depends on its location in the tank. For example, the velocity-squared dependent damping of the screen will be greatest for the first mode ($n = 1$) of fluid response when placed at the location of maximum velocity in the centre of the tank ($0.5L$). Figure 3.12 demonstrates the spatial influence of the damping screens with the two screen locations and the 5 fixed-angles used in this study superimposed on a plot of the normalized (linear) horizontal fluid velocity amplitude for the first three sloshing modes, $n = 1, 2, 3$ (§4.5). The 30-45° angle mentioned earlier can be seen in Figure 3.12 aiding in suppressing the second and third higher harmonics, which reduces the response associated with higher sloshing modes (Chester 1968, Szemplinska-Stupnicka 1968).

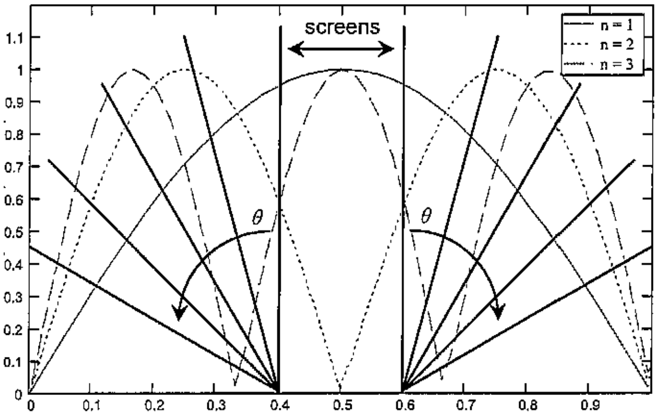

Figure 3.12. Normalized fluid velocity amplitude mode shapes, $n = 1, 2, 3$ (ordinate) vs. Normalized tank length (abscissa). Inclined screens superimposed.

3.8 The Effect of Excitation Amplitude on E_w'

The energy dissipated by the tuned liquid damper, over a range of applied sinusoidal base excitation amplitudes, is addressed in this section. Presented in

Figure 3.13 and Figure 3.14 are the experimental non-dimensional energy dissipation, E_w', frequency-response curves for the 42% and 52% screens, respectively, for a range of excitation amplitudes, $0.003 \leq \Lambda \leq 0.052$, and all screen angles except for 15°. At $\theta = 15°$ no significant increase in E_w' was found (for example, recall Figure 3.9) and is therefore omitted. The frequency-response curves decrease in height with increasing excitation amplitude, since these non-dimensional plots are normalized by the maximum kinetic energy of the water mass (Equation (3.5)). The non-dimensional curves indicate the amplitude-dependency of the damping in a TLD as opposed to the linear viscous damping of a TMD. For a dynamic system having velocity-square damping, η is proportional to $\sqrt{A}$ and ζ_a is a function of η (Tait 2007). Therefore, as the amplitude increases so does the damping, which lowers the non-dimensional energy dissipation. However, for the case of increasing screen angle, E_w' increases as there is less damping provided by the screens, for a particular excitation amplitude.

As expected, the typical hardening characteristics associated with increased excitation amplitude (Tait 2004) can be observed in the following two figures. This is emphasized in the $\theta = 0°$ curves in Figure 3.13 and Figure 3.14 by a dashed line drawn approximately through the peaks of the frequency-response curves. For all experimental results including both sets of solidities, the natural sloshing frequency equation (Equation (4.39), $n = 1$) predicts the peak frequency very well up to a normalized excitation amplitude of approximately $\Lambda = 0.010$.

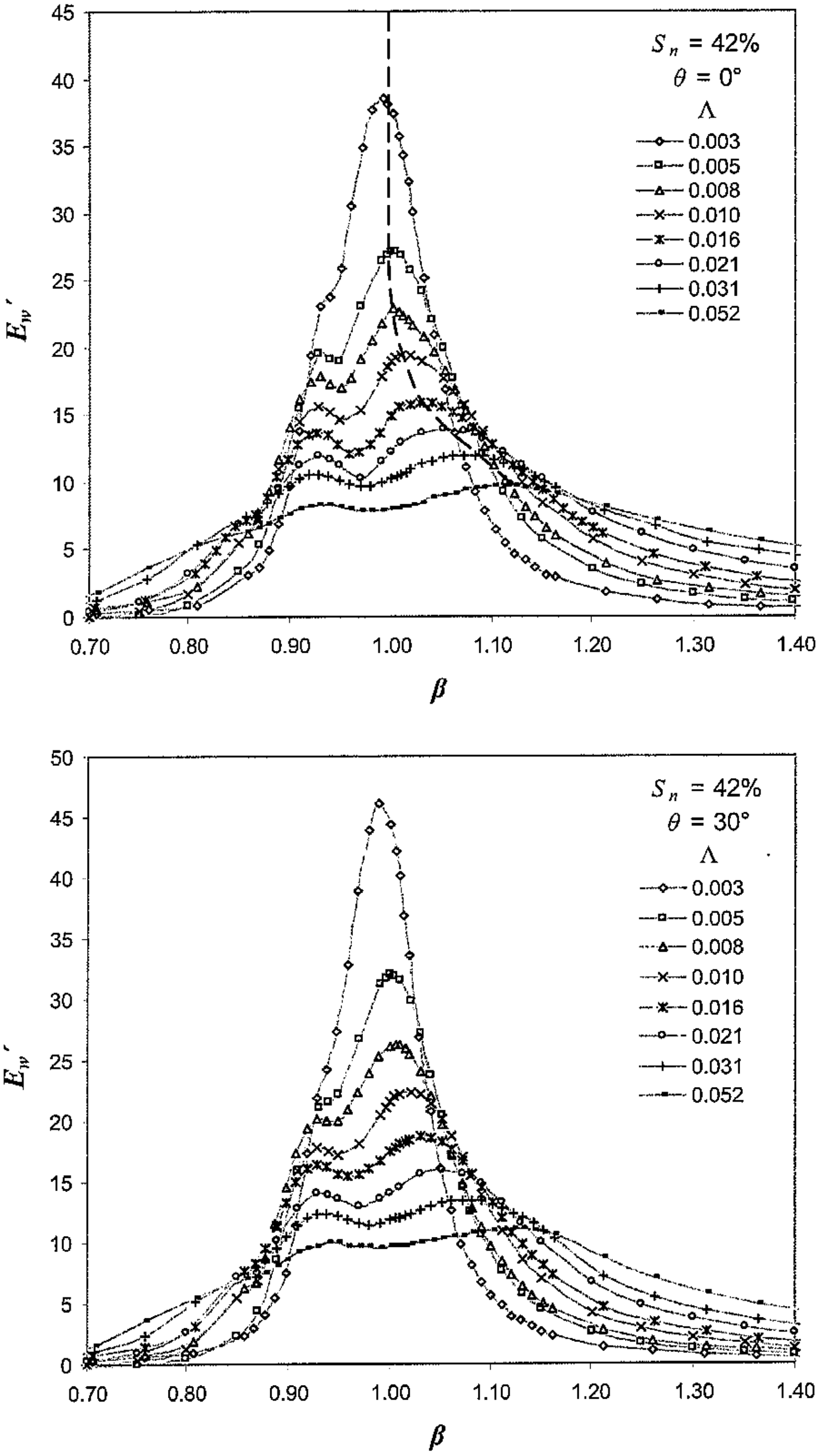

Figure 3.13. Experimental frequency-response for 42% screens (0° & 30°).

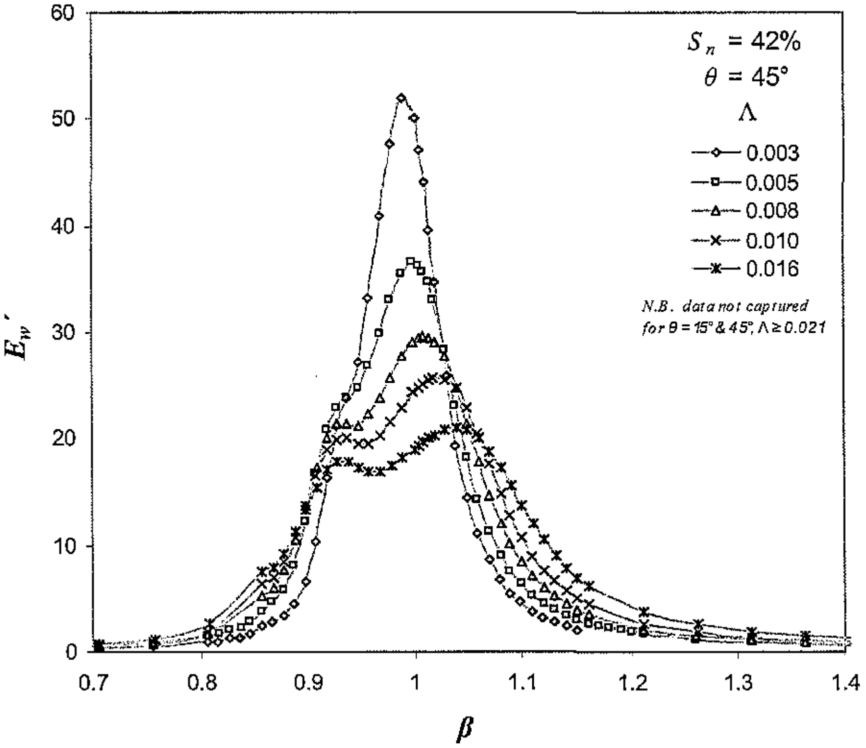

N.B. data not captured for $\theta = 15°$ & $45°$, $\Lambda \geq 0.021$

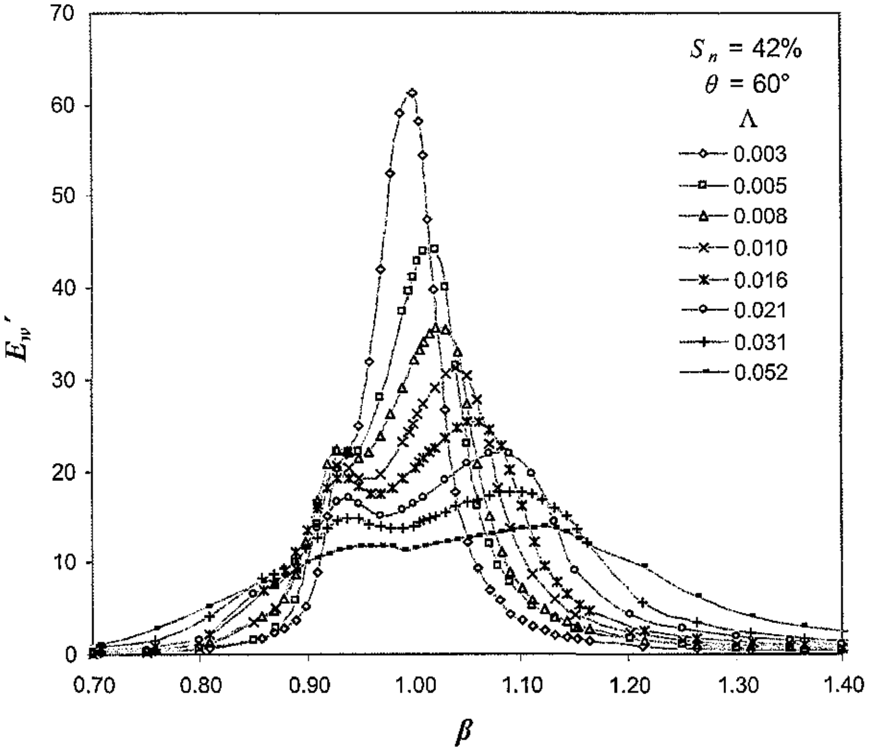

Figure 3.13 (continued, 45° & 60°)

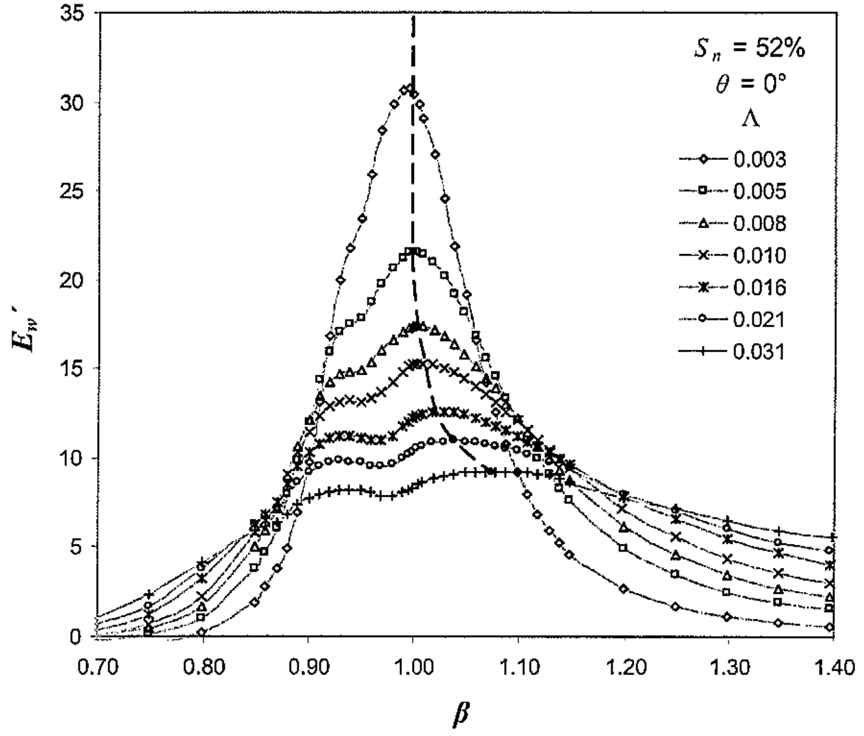

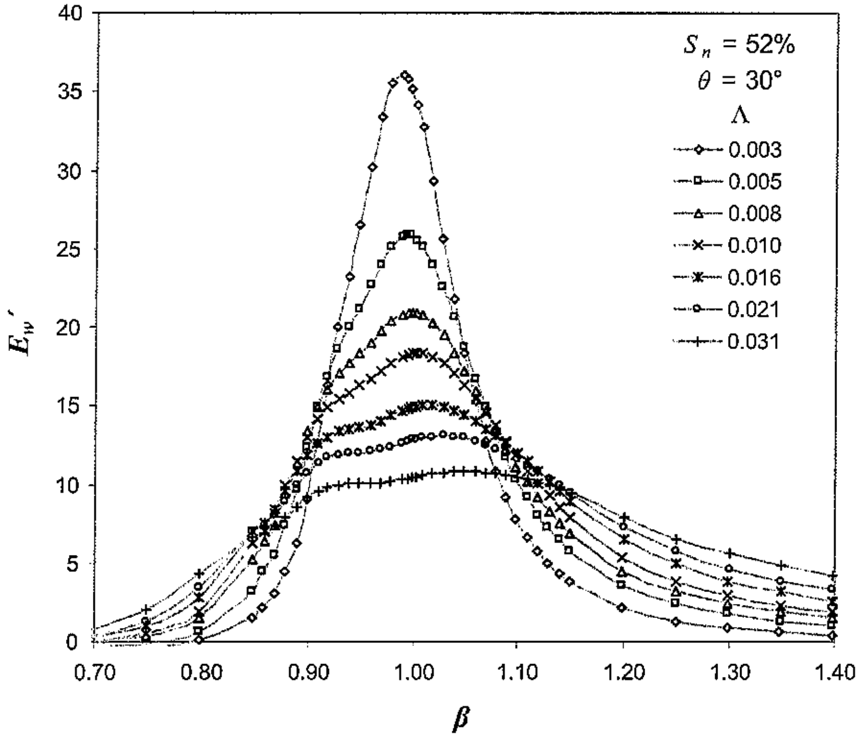

Figure 3.14. Experimental frequency-response for 52% screens (0° & 30°).

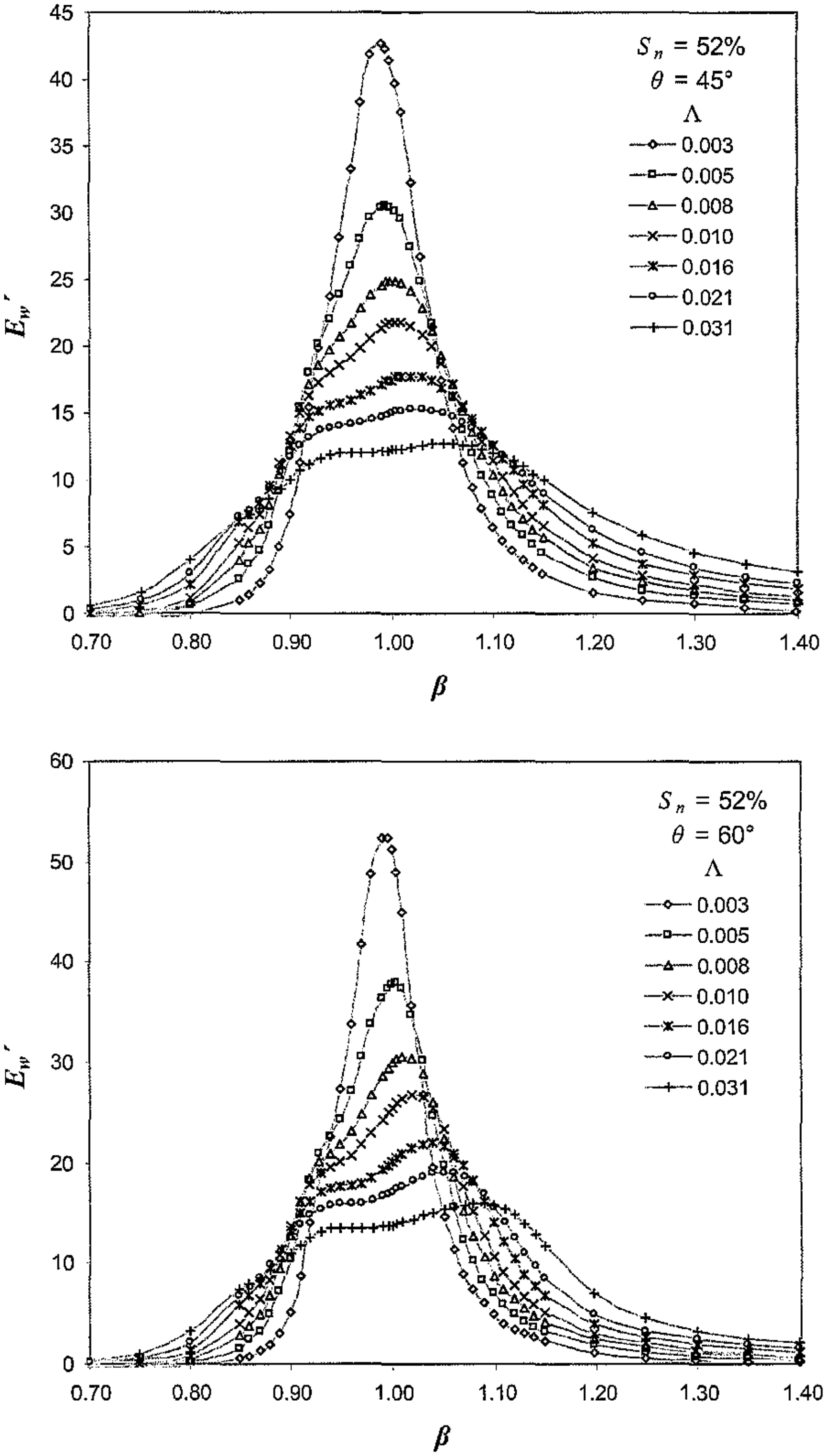

Figure 3.14 (continued, 45° & 60°)

Comparing Figure 3.13 and Figure 3.14 with the frequency-response curves presenting the effect of screen angle, θ, over a single excitation amplitude in Figure 3.8 and Figure 3.9, it can be seen that the shift in peak frequency is predominately due to the increasing excitation amplitude and not to an increase in screen angle.

3.9 Screen Forces

Experimentally measured screen forces using load cells (see §2.4.1) for various θ are presented in Figure 3.15 and Figure 3.16, which is important when determining the design loads on the damping devices utilized. $\Lambda = 0.005$, 0.010, and 0.021 are selected for both solidities (screens), where the intermediate angles of 15° and 45° are not shown for $S_n = 42\%$.

Both figures display the velocity-squared drag force characteristics, which can be seen by the common shape of all the curves, similar to screen force characteristics on flat plates from other authors (Keulegan and Carpenter 1958, Okajima et al. 1998). As θ increases, the curves tend to stretch out and multiple peaks begin to occur at $\theta \geq 30°$ for large excitation amplitudes ($\Lambda = 0.021$).

Similar increase in peak screen forces (at resonance)—for $\Lambda = 0.005$ at $\beta = 1.01$, both figures—indicate that the fluid pressure-loss may be independent (or weakly-dependent) of the direction of flow. This assumption shall be taken into account for the development of C_D in Chapter 4. Analogous trends are found for other Λ (at differing peak β).

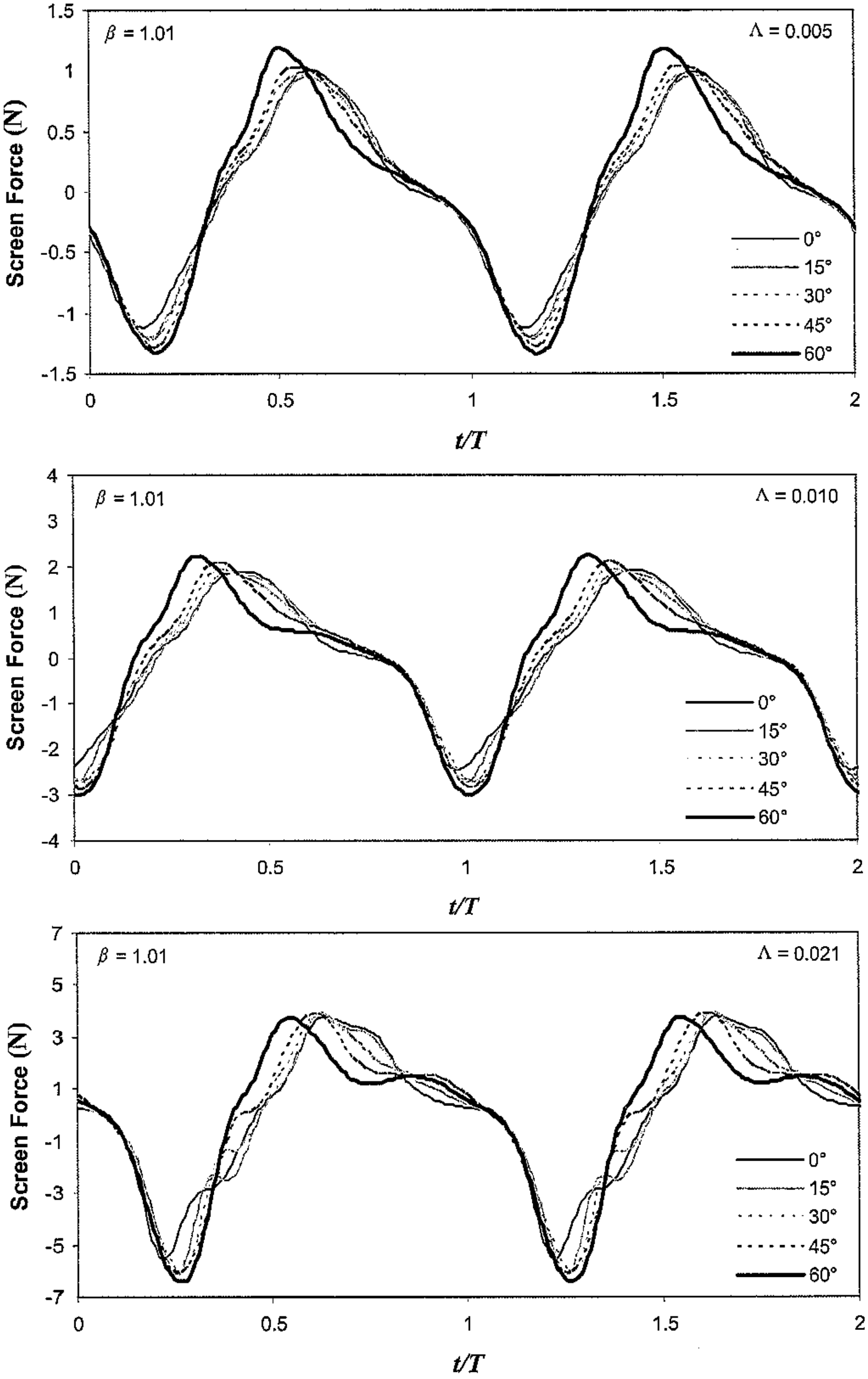

Figure 3.15. Experimental screen forces for 52% screens at $\beta = 1.01$.

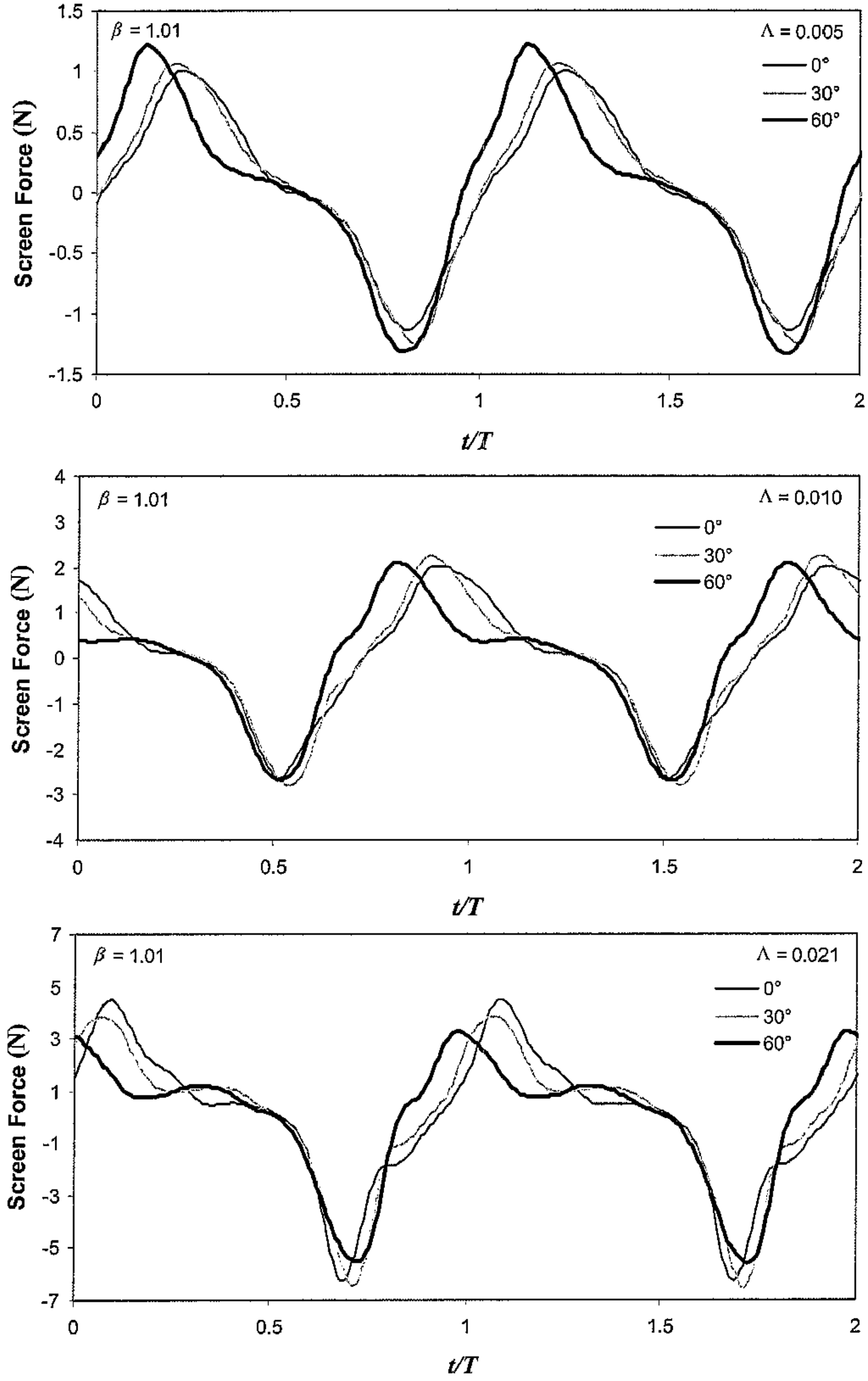

Figure 3.16. Experimental screens forces for 42% screens at $\beta = 1.01$.

3.10 Free-Surface Response

Figure 3.17 and Figure 3.18 display the normalized free-surface response over the same excitation amplitudes and frequency as in the previous section. These waveforms may be contrasted with their low-pass filtered counterparts in Figure 4.19 and Figure 4.20 of §4.7.2. The influence of increasing excitation amplitude and resulting higher harmonics on $\eta(t)$ is evident in the figures when contrasted with the fundamental component shown in §4.7.2.

As can be seen in Figure 3.17 and Figure 3.18, a significant increase in $\eta(t)$ is observed for $\theta = 30°$ to $60°$, as opposed to $0°$ to $30°$. As will be seen in Chapter 4, the pressure-loss coefficient is not a linear function of screen inclination, θ.

3.11 Force-Displacement Hysteresis

In Figure 3.19 and Figure 3.20, the E_w' energy loops (or hysteresis loops) for different screen angles, θ, are shown. Intermediate angles, 15° and 45°, are not shown for the 42% screens. Non-dimensional base shear force, F_w', is plotted in the y-axes and non-dimensional shake-table displacement, $\Lambda = A/L$, is plotted in the x-axes. Recurring amplitudes, 0.005, 0.010, and 0.021, are displayed over four frequency ratios, $\beta = 0.95$, 1.01, 1.07, and 1.15.

Increased non-linear response is present in the (less solid) 42% screens as seen by the increased waviness in the hysteresis loops due to the presence of higher harmonics. At $\beta = 1.01$, the resonant frequency can be seen shifting

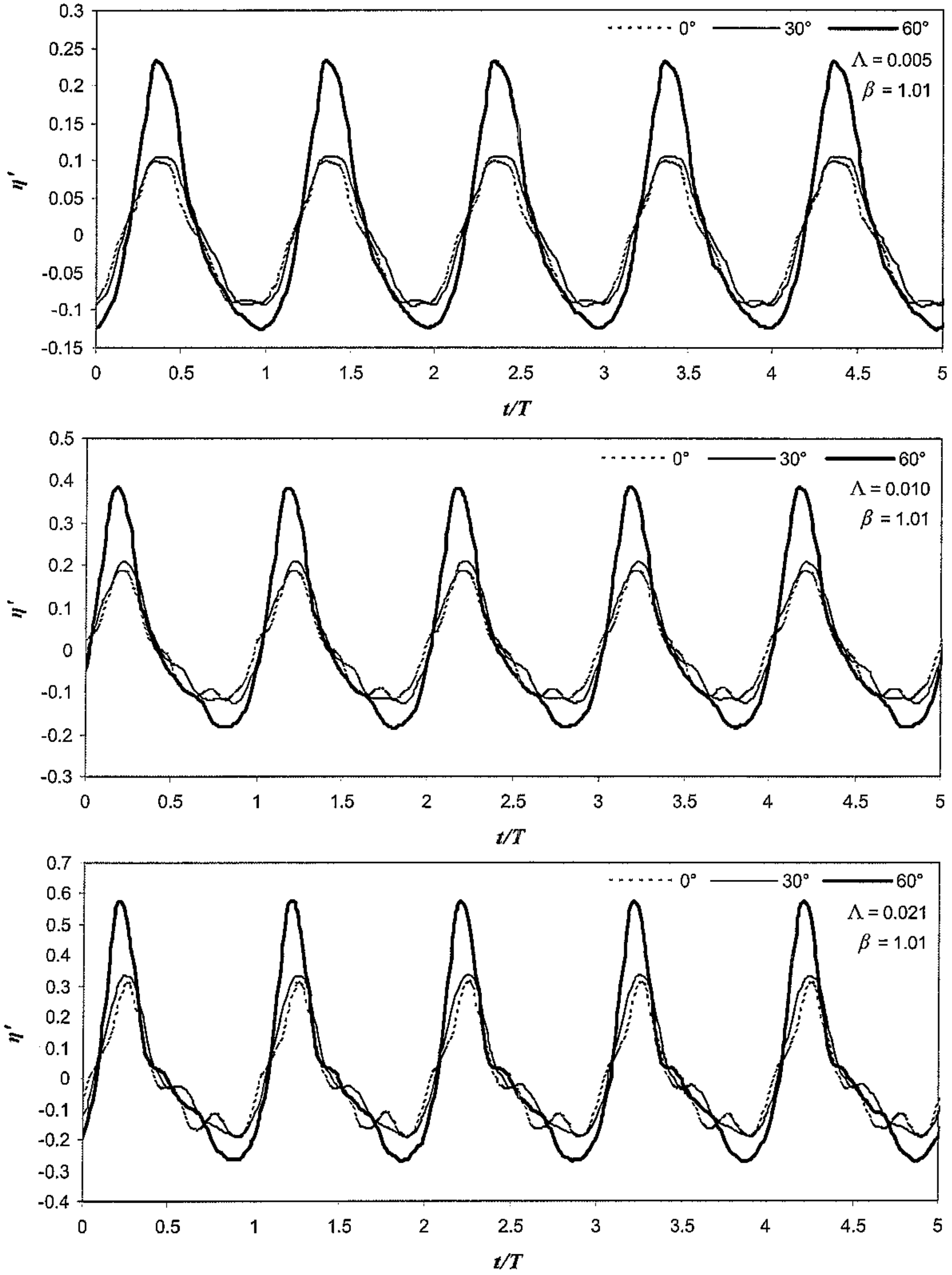

Figure 3.17. Experimental free-surface response for 52% screens.

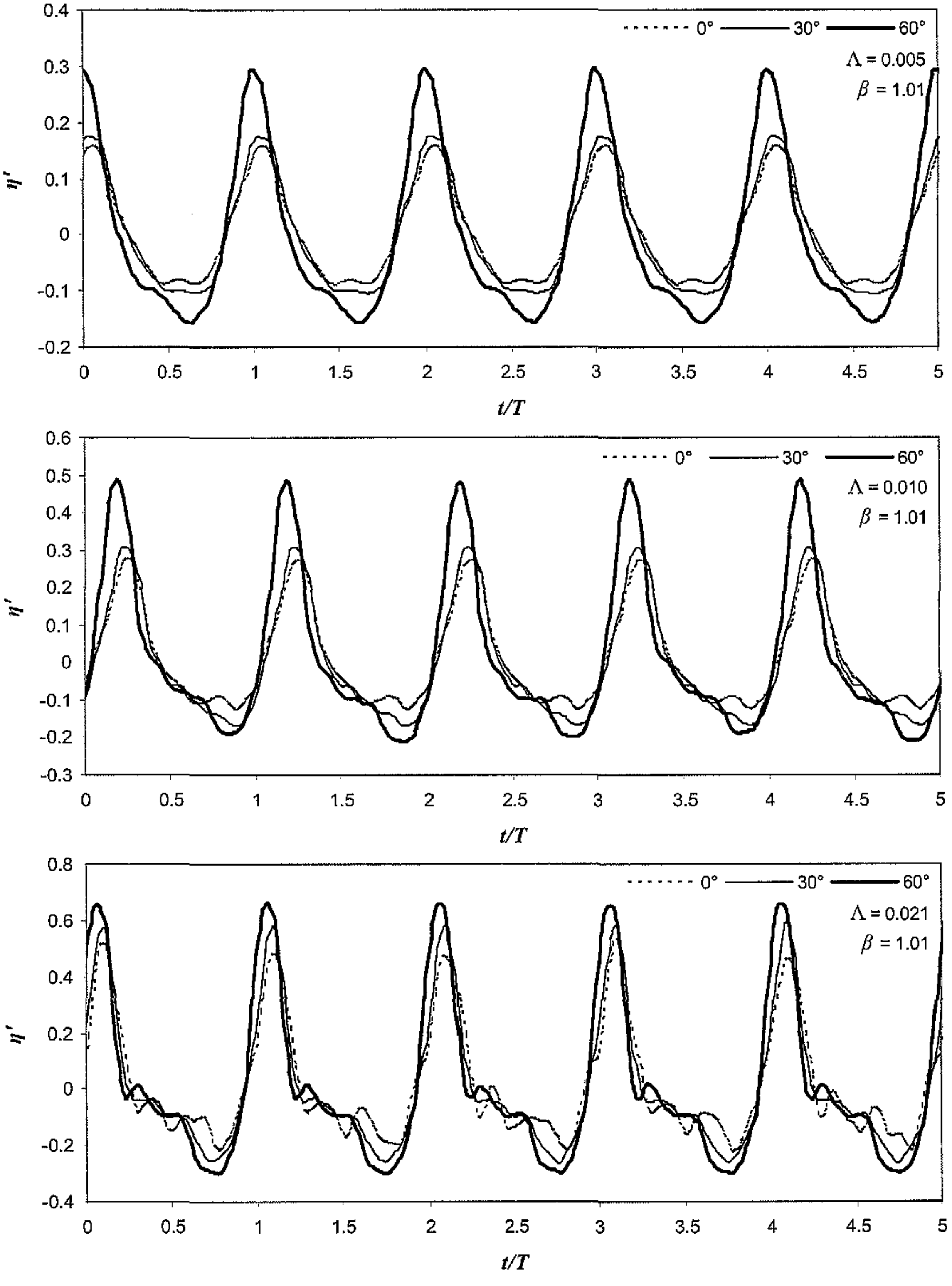

Figure 3.18. Experimental free-surface response for 42% screens.

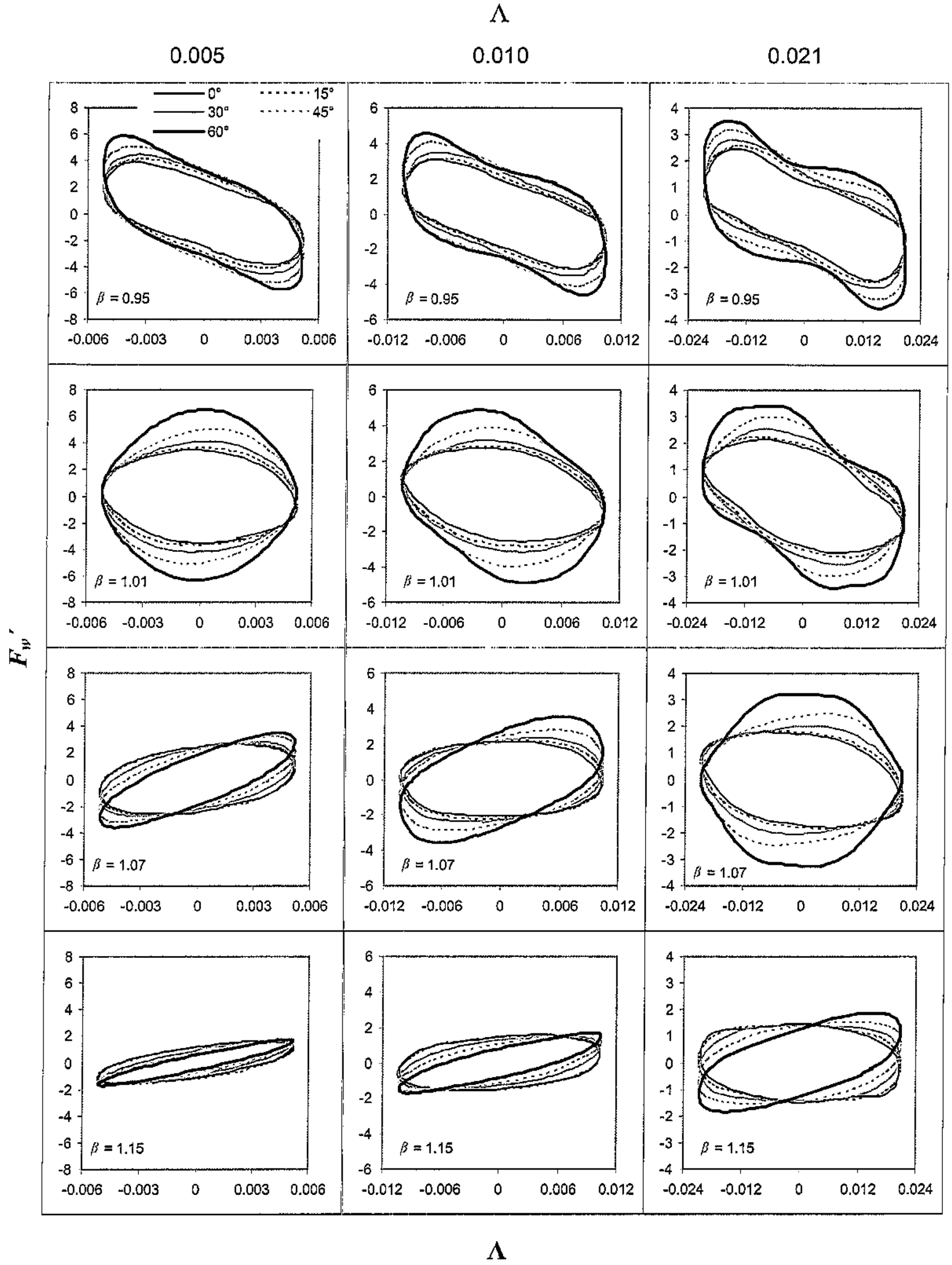

Figure 3.19. Non-Dimensional energy loops, F_w'-Λ (ordinate-abscissa), for 52% screens over θ.

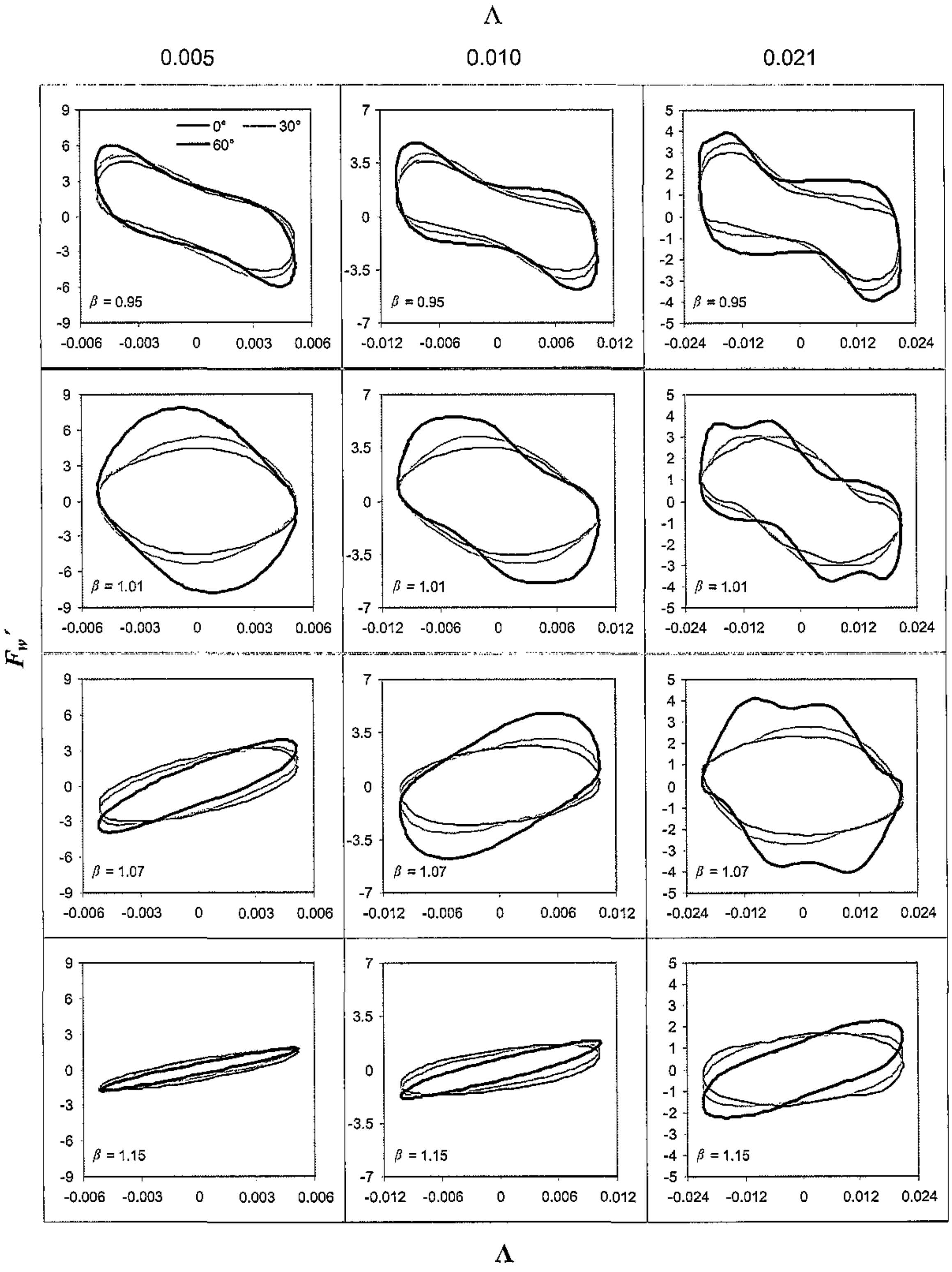

Figure 3.20. Non-Dimensional energy loops, F_w'-Λ (ordinate-abscissa), for 42% screens over θ.

over excitation amplitudes, for example, the hysteresis loop for $\Lambda = 0.005$ at $\theta = 0°$ rotates and appears more elliptical at $\Lambda = 0.021$ at $\theta = 0°$. Resonance for $\Lambda = 0.021$ at $\theta = 0°$ occurs around $\beta = 1.07$.

The slight hardening at higher screen angles is evident in both figures. For a particular excitation amplitude, Λ, the counter-clockwise trajectory of the loops increases appreciably only for $\theta > 45°$. The clockwise trajectory of the loops is attributed to changes in Λ and correspondingly the response of the TLD. The simultaneous influences of Λ and θ on the phase angle (loop trajectory), φ, of the response are both attributed to their respective changes in damping, ζ_a ($\Lambda\uparrow\zeta_a\uparrow$, while $\theta\uparrow\zeta_a\downarrow$). This further explains the influence of θ against the effect of Λ in the non-linear fluid response. The marked difference in loop area from $\theta = 30°$ to 60° as opposed to $\theta = 0°$ to 30° can be seen in the figures, which is reflected in the increased values of peak E_w' at high θ, as opposed to $\theta = 0$ to 15°, for example (recall Figure 3.8 or Figure 3.9).

3.12 Constant Peak Energy over Various Fixed-Angles

The impetus for this study is to achieve invariable TLD damping, ζ_a, over a range of excitation amplitudes by altering the screen angle, θ. Figure 3.21 presents experimental results from the fixed-angle tests demonstrating a level of peak response that is nearly constant over a range of amplitudes from 0.005 to 0.016 at different screen angles, particularly 0.005 at 0°, 0.008 at 30°, 0.010 at 45°, and 0.016 at 60°. The same amplitudes and angles are displayed for both the

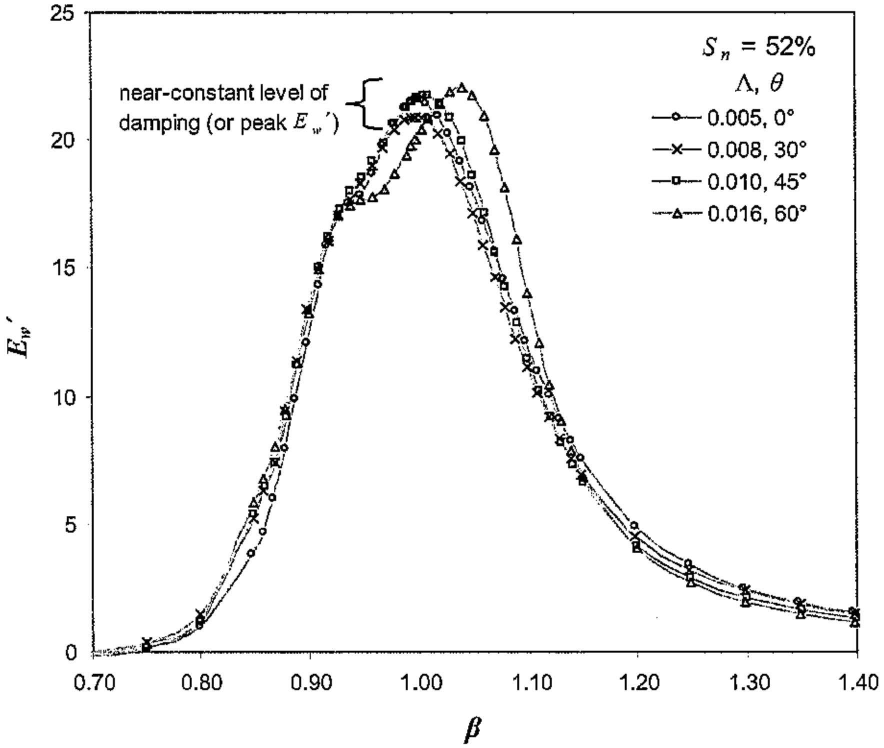

Figure 3.21(a). Fixed-Angle β-E_w' curves yielding near-constant peak E_w'.

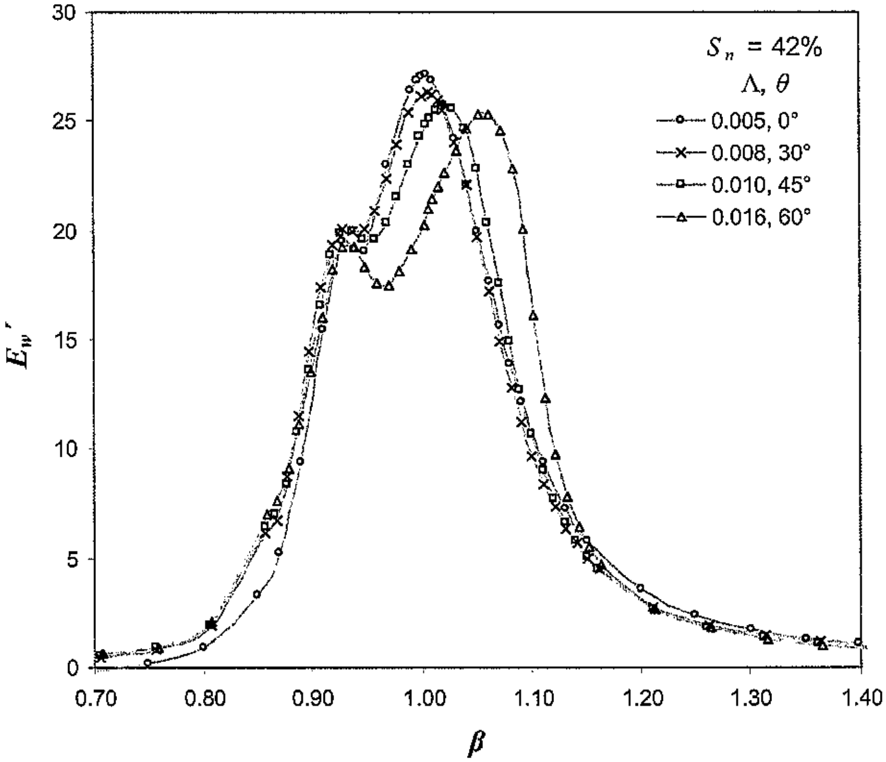

Figure 3.21(b). Near-constant E_w' for 42% screens.

52% screens (in Figure 3.21(a)) and the 42% screens (in Figure 3.21(b)). Similar families of peak E_w' curves can be extracted from Figure 3.13 or Figure 3.14 at higher amplitudes; however, frequency-shifting due to excitation amplitude is more pronounced.

Figure 3.21 reinforces the experimental finding of only slight hardening with increasing screen angle (for $\theta < 60°$). Also, the excitation amplitude at 60° is 3 times that of 0°; however, there is only a 4-5% shift in peak frequency from 0.005 at 0°. Note that for Figure 3.21(b), the 42% screens, the frequency-shift (particularly at 60°) is more than that shown in Figure 3.21(a), which once again can be attributed to an increase in η due to a lower solidity.

3.13 Summary and Conclusions

This chapter presented results from experiments conducted on a TLD equipped with symmetrically-angled horizontal-slat screens. Two different sets of screens with differing solidity ratios were investigated. TLD energy, screen forces, and free-surface response have been shown. The following conclusions can be drawn:

- For the frequency domain, the overall TLD performance was examined using energy dissipation. The average work done per cycle at each frequency is a convenient way of examining the frequency-dependent performance of a damper in general, rather than force vectors, their direction, and their minima or maxima.

- Screen angle reduces the damping effect of the screens with increasing angle and change in energy dissipation is found to be relatively consistent over the range of amplitudes tested (for each increment in inclination)
- The effect of inclined screens on the inherent TLD damping, ζ_a, has demonstrated that one set of screens can dissipate an equivalent amount of energy as another set of screens having a different solidity (§3.7). This makes it possible to replace multiple sets of screens with one, conceivably adjusting its angle with excitation amplitude to target an optimal design performance through a *range* of excitation amplitudes
- Experimental results show that despite the natural amplitude-dependent peak frequency hardening due to increasing free-surface response, more significant free-surface response due to increased screen angle does not lead to a significant change in the resonant frequency, which aids in keeping the TLD in-tune with a structure
- In conjunction with the forth point, the free-surface response amplitude, η, increases greatly with increasing θ without significant frequency-hardening, unlike the behaviour of increasing η linked with increasing excitation amplitude, A. The phase, φ, of η was shown to harden (increase in β) only slightly at high screen angles early in the chapter (Figure 3.6)
- Symmetrically inclined screens maintained near-constant inherent TLD damping (or peak energy dissipation) over a three-fold range of excitation

amplitudes at varying angles. This would have an advantageous influence on the interaction with a structure (Chapter 6).

CHAPTER 4: LINEAR SIMULATION OF SYMMETRIC FIXED-ANGLE SLAT-SCREENS IN A TUNED LIQUID DAMPER

4.1 Introduction

A drag (or pressure-loss) coefficient is often used to model the influence of a damping device on the response of a *tuned liquid damper* (TLD). For vertical screens, this drag coefficient can be expressed as a sole function of the screen solidity (Tait 2004).

The drag coefficient—or related fluid pressure-loss coefficient—for vertical damping screens has been investigated by numerous researchers such as Cornell (1957), Baines and Peterson (1951), and Prandtl (1933). However, there is little consensus on the details of the pressure-loss characteristics through angled screens, especially in oscillatory flow.

This chapter investigates the details of flow through angled screens, including a review of past research and extending the derivation of the pressure-loss coefficient based on solidity, S, to include the screen angle, θ. Two linear flow models based on shallow water wave theory and potential flow theory, respectively, will be presented. The results of the fixed-angle experiments (presented in the previous chapter) are compared with results from the two flow models, including the models' ability to predict the sloshing water response utilizing a single pressure-loss coefficient, C_θ (each screen), for the damping effects of the angled screens based on S and θ.

First, some further details of the damping slat-screens pertinent to this chapter are explained in the following section.

4.2 Slat-Screens

The type of damping device used in the TLD studied is a slat-screen. The screen is made up of identical individual rectangular slats approximately a millimetre thick, which are spaced evenly apart to form a slotted plate of stainless steel (§2.2). An important parameter that determines the primary influence of screens in fluid flow is the solidity ratio, S (Schubauer et al. 1950). As mentioned in Chapter 2, the slat-screens used in this study are described by their nominal solidity ratio, S_n (expressed as a percentage), which is a characteristic of the screen and defined as the ratio of the slat width to the slat spacing,

$$S_n = \frac{d}{b_s} \tag{4.1}$$

where d is the slat width and b_s is the slat spacing (or on-centre spacing) as was depicted in Figure 2.3. The actual solidity ratio after accounting for all other structural components (required to suspend the screens in the tank as described in Chapter 2) that block fluid flow will be higher and is denoted as the fraction (expressed as a decimal number),

$$\frac{A_s}{A_g} \tag{4.2}$$

where A_s is the total solid portion of the screen submerged in water and A_g is the total gross area of the screen submerged in water. The two pairs of screens tested in this study have nominal and actual solidity values of 42% at 0.4740 and 52% at 0.5605, respectively.

Two screens of equal solidity were placed at locations of 0.4*L* and 0.6*L* inside the tank. The screen locations and solidity ratios used in this study are expected to provide sufficient damping (§3.7). As shown in Figure 4.1, these particular screen locations were also chosen for physical reasons. The maximum screen angle was 60° and the wave height (η) was measured at locations near the ends of the tank at 0.05*L* and 0.95*L*. A large range of screen angles can be investigated using these particular screen locations as well as allowing for adequate space for the screens to oscillate in their passive control mode (investigated in Chapter 5). The fixed screen inclinations selected (see Table 2.1) for this study are $\theta = 0$, 15°, 30°, 45°, and 60°.

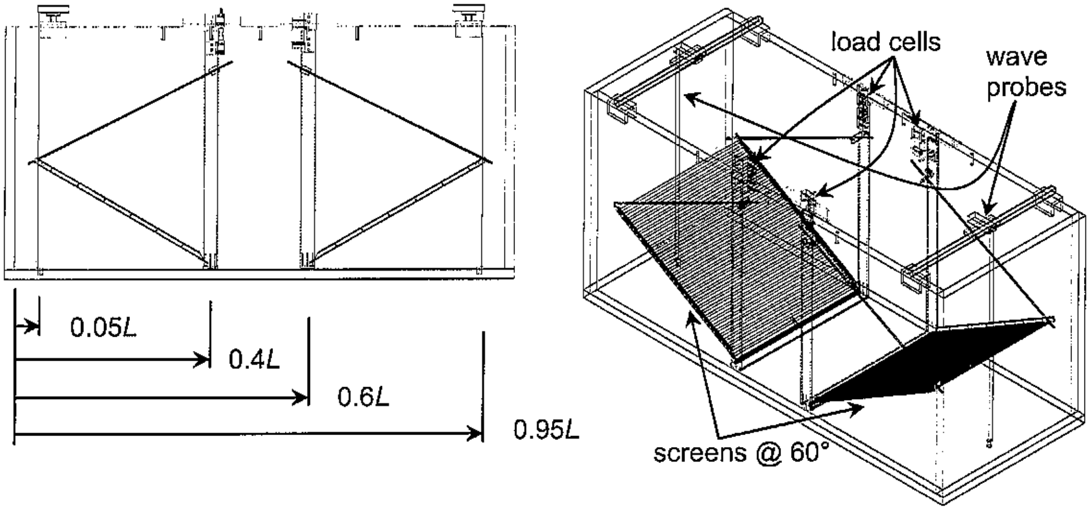

Figure 4.1. Location of screens and wave probes.

4.3 Loss Coefficient for Slat-Screens in Oscillatory Flow

A single parameter, the pressure-loss coefficient, is used to describe the influence of the damping screens in oscillating fluid flow. First, a pressure-loss coefficient, which describes the behaviour of regular vertical (0°) slat-screens in oscillatory flow, C_l, is described. Subsequently, various pressure-loss coefficients that vary with screen angle, C_θ, are investigated and evaluated.

4.3.1 Pressure Loss Coefficient for Vertical (0°) Slat-Screens, C_l

For steady (non-oscillating) flow, Baines and Peterson (1951) suggest using the following equation to estimate C_l,

$$C_l = \left(\frac{1}{C_c\left(1-S\right)} - 1 \right)^2 \tag{4.3}$$

where S is the solidity ratio and C_c is the contraction coefficient for the screen type. As the type of sharp-edged slat-screens utilized throughout this study are the same as those utilized by Tait (2004), a contraction coefficient suggested by Tait (2004) solely as a function of S is used based on the experimental work by Weisbach (1855), which is,

$$C_c = 0.405e^{-\pi S} + 0.595 \tag{4.4}$$

The drag coefficient, C_D, is related to the loss coefficient, C_l, as follows,

$$C_D = \frac{C_l}{S} \tag{4.5}$$

It should be noted that for a screen similar to those used in this study with a solidity ratio higher than 0.30, Equations (4.3) and (4.5) can be used to estimate the coefficients C_l and C_D without the need of the modified curves presented in Baines and Peterson (1951). C_D is the parameter used to determine the drag force, F_D, being exerted on the screen, normal to the screen plane,

$$F_D = \frac{1}{2}\rho C_D u^2 A_s \tag{4.6}$$

where ρ is the density of water and u is the fluid velocity.

4.3.2 Pressure-Loss Coefficient for Angled Slat-Screens, C_θ

A more detailed explanation for the losses through an angled screen than that introduced in Chapter 1 is presented here. The pressure-loss coefficient for inclined slat-screens depends primarily on the normal component of fluid flow through a screen; even though the flow approaches with an angle of incidence assumed to be equivalent to the screen angle, θ, and leaves with the deflection angle, ψ, on the leeward side of the screen (Schubauer et al. 1950). Little literature exists with a detailed analysis on the pressure-loss through an angled screen, which is mainly found to focus on inclined woven-wire screens in steady flow and not on inclined slat-screens in oscillatory flow. For this reason, three different C_θ values will be presented and subsequently evaluated. The values of C_θ have been determined using: (1) a common description of oblique fluid flow on any object or structure; (2) an empirical method based on experimental findings attempting to capture the overall losses found at low and very high screen angles; and (3) an angled pressure-loss coefficient based on the well established use of C_l by Baines and Peterson (1951) in Equation (4.3) for vertical screens.

For screens whose normal direction vector (perpendicular to the plane of the screen) is at an angle, $0° \leq \theta \leq 45°$, to the incident flow, Schubauer et al. (1950) reported the pressure drop to be proportional to the square of the component of U_o, the average fluid velocity throughout the depth, normal to the screen (otherwise known as the cross-flow principle), i.e.,

$$\Delta P = \frac{1}{2}\rho C_\theta \left(U_o \cos\theta\right)^2 \tag{4.7}$$

Garrison (1985) also states the cross-flow principle, referred to by Hoerner (1964), in which the force acting in the direction normal to the axis of a cylinder placed at some oblique angle to the direction of steady flow is expressed in terms of the normal component of the flow only, and the axial component is disregarded; the drag coefficient used in this formulation is considered to be independent of the angle of incidence. Steady flow represents the limiting case of oscillating flow when the Keulegan-Carpenter number becomes large (Garrison 1985). The range of Keulegan-Carpenter numbers covered in this study will be detailed later as well as the experimental affirmation of the use of steady flow equations for oscillatory flow. There exist many similarities regarding drag (and pressure-loss) between cylinders and flat plates (slats) (Okajima et al. 1998) and the cross-flow principle has been applied to both. Equation (4.7) combined with the well-known Equation (1.4) for the pressure-drop coefficient yields,

$$C_\theta = C_l \cos^2 \theta \tag{4.8}$$

therefore, C_l equals C_θ at $\theta = 0°$ ("$C_{0°}$"), a vertical screen. Richards and Robinson (1999) and Laws and Livesey (1978) also find the pressure-loss through a screen to be proportional to the square of the cosine of the angle of incidence (assumed to be the angle of the screen), which is a well-known trend. However, at high angles greater than 45°, it has been found that this simple relationship underpredicts fluid losses (Carrothers and Baines 1965), which is examined in §4.7.1.

Carrothers and Baines (1965) provide an empirical (experimental) solution to correct for the underprediction of losses at angles greater than 45°. They maintain that C_θ in Equation (4.8) is suitable for $\theta \leq 45°$ but have corrected for $\theta > 45°$. Blevins (1984) provides a table of the reduction in losses as a fraction of the losses for a vertical screen at 0° and his values selected from experimental results by Carrothers and Baines (1965) are shown in Table 4.1 below,

Table 4.1. Fraction of C_l with Angle.

θ (degrees)	0	10	20	30	40	50	60	70	80	85
γ_θ	1.00	0.97	0.88	0.75	0.59	0.45	0.30	0.23	0.15	0.09

where γ_θ is a fraction of the vertical loss coefficient, C_l. The γ_θ values in Table 4.1 from 0° to 40° are exactly $\cos^2\theta$, whereas 50° to 85° are from the experimental results and deviate from the $\cos^2\theta$ trend. Neither source provides a formula or equation for this finding but from a 3rd order polynomial regression one can obtain a relationship for γ_θ from Table 4.1 as,

$$\gamma_\theta = 0.46\theta^3 - 1.05\theta^2 - 0.06\theta + 1 \tag{4.9}$$

where θ is expressed in radians. Therefore, the second estimated angled screen loss coefficient—which is essentially an extension of the pressure-loss relationship of Equation (4.8)—that will be considered in this study is,

$$C_\theta = C_l \cdot \gamma_\theta \tag{4.10}$$

The third estimate of the loss coefficient to be analyzed is one developed based on the established use of that provided by Baines and Peterson (1951) in Equation (4.3) with modifications based on the analytical and experimental work of Yeh and Shrestha (1989). Tait (2004) has shown experimentally that Equation (4.3) is valid for oscillating flow in the practical excitation amplitude range the author worked in (for S_n = 42%), $\Lambda \geq 0.003$, having corresponding KC values equivalent to those used in this study, which will be detailed later in this chapter. Since Equation (4.3), originally formulated based on steady-flow, can be employed for oscillatory flow, formulating a loss coefficient for angled screens based on Baines and Peterson (1951) and introducing the concept of angled steady-flow is the approach taken. Yeh and Shrestha (1989) developed a prediction model for the head loss through an inclined screen that is placed in steady-flow. The following derivation description combines these two concepts.

It is assumed that the angle of incidence, ϕ, of the approaching flow to the screen is uniform and equal to the angle of inclination, θ. The exiting flow is deflected at an angle, $\psi(\theta) \propto \theta$, which is measured from the leeward screen normal to the horizontal and is always less than the screen angle, $\theta \geq 0°$. Figure 4.2 sketches the three key angles of consideration by depicting the passage of streamlines through an angled screen at a theoretically small distance apart, δh, a fraction of the overall still water depth, h. Considering the screen inclination and the flow contraction, the effective flow area per unit width of the screen at the vena contracta, A_c, detailed in Figure 4.2 is (Yeh and Shrestha 1989),

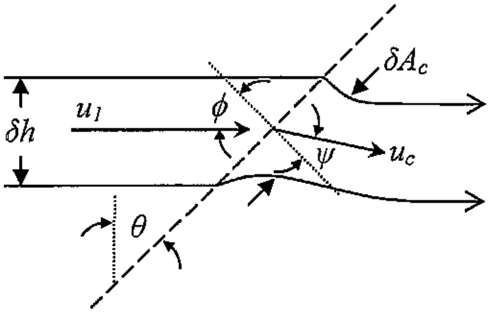

Figure 4.2. Streamlines through screen.

$$A_c = \frac{(1-S)C_c h}{\cos\theta} \tag{4.11}$$

u_1 is the flow velocity upstream of the screen and u_c is the velocity at the vena contracta. Using Equation (4.11), continuity, and the Bernoulli equation, the pressure difference across the screen is found to be (Yeh and Shrestha 1989)

$$\Delta P = \frac{1}{2}\rho u_1^2 \left(\frac{\cos^2\theta}{(1-S)^2 C_c^2 \cos^2\psi} - 1 \right) \tag{4.12}$$

Next, the momentum equation (Baines and Peterson (1951)) is applied and introducing the notation, $C = (1 - S)\cdot C_c$, a third estimate of the pressure-loss coefficient for an angled screen is obtained,

$$C_\theta = \left(\frac{\cos\theta}{C \cdot \cos\psi} - 1 \right)^2 \tag{4.13}$$

Note that for $\theta = 0°$, Equation (4.13) reduces to the pressure-loss equation for a vertical screen obtained by Baines and Peterson (1951), Equation (4.3). According to Taylor and Batchelor (1949), the value of the deflection angle, ψ, is insensitive to the flow velocity and, for a given screen, the value of ψ/ϕ is nearly constant, recall that $\theta = \phi$. Yeh and Shrestha (1989) have shown through flow-visualization that this is not entirely accurate; however, it was demonstrated by measuring the flow deflection with screen inclination that a constant value of $\psi/\theta = 0.8$ in their study describes the overall deflection throughout the depth of the screen sufficiently for screen angles up to 45-50°.

It must be noted that in order to improve the accuracy of the loss coefficient corresponding to a particular experiment, one must measure the deflection angle throughout the screen depth for the particular screen and flow (velocity) being studied. However, for simulations conducted in this study, it was necessary to estimate $\psi(\theta)$, which follows the approach taken in Yeh and Shrestha (1989).

Figure 4.3 is an array of photos captured from video of 15mm excitation amplitude tests (mid-range) at resonance at screen angles of 15° to 60°.

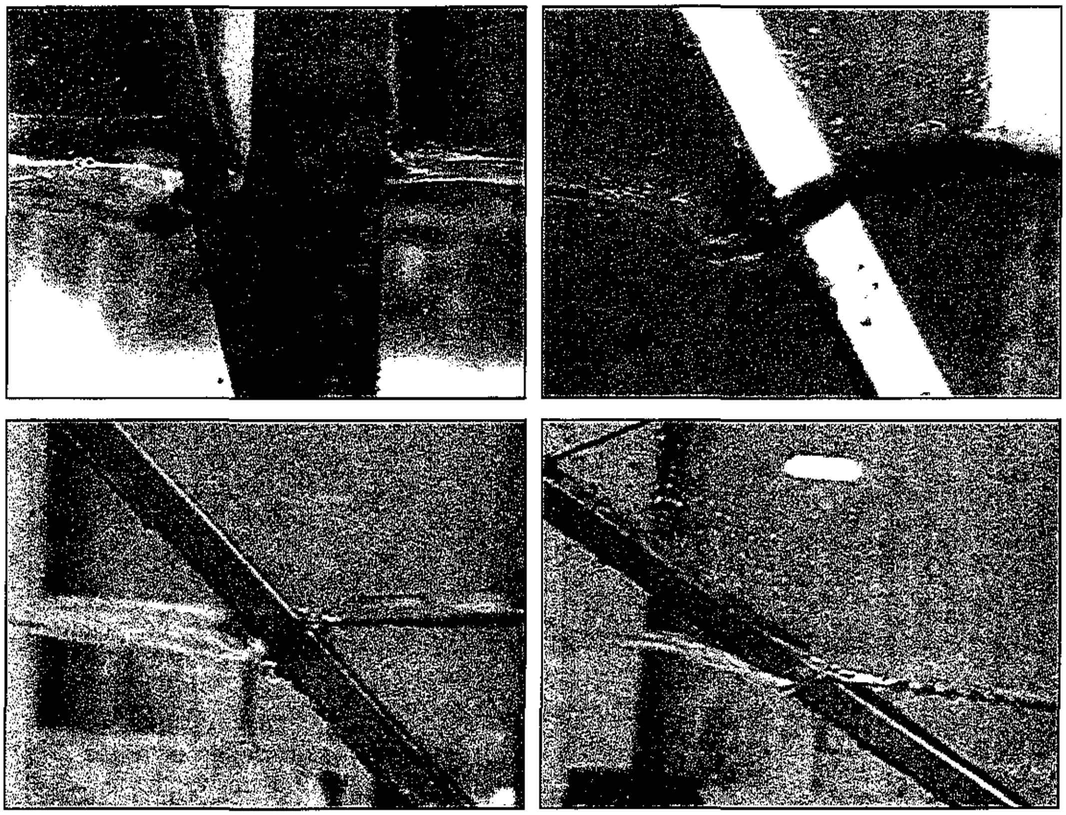

Figure 4.3. 15mm amplitude flow deflection (clockwise from top-left, $\theta = 15°, 30°, 60°, 45°$).

From observations made during testing and from numerous photographs, including the ones in Figure 4.4, it has been assumed that a value of $\psi/\theta \approx 0.7\text{-}0.9$ is sufficient for describing the deflecting behaviour of the fluid throughout most tests conducted, although consideration for an increased deflection angle, $\psi(\theta)$, may be warranted for high screen angles, given the deflection visible at 60° in Figure 4.3 compared to the rest of photos in Figure 4.3 and Figure 4.4.

Figure 4.4 shows photographs of flow deflection for a wide range of amplitudes up to a high excitation amplitude of 50mm. Again, a flow deflection of $\psi/\theta \approx 0.7\text{-}0.9$ is considered appropriate for $\theta \leq 60°$. A value of $\psi/\theta < 1$ is visibly predominant at the higher amplitudes, emphasized in Figure 4.4.

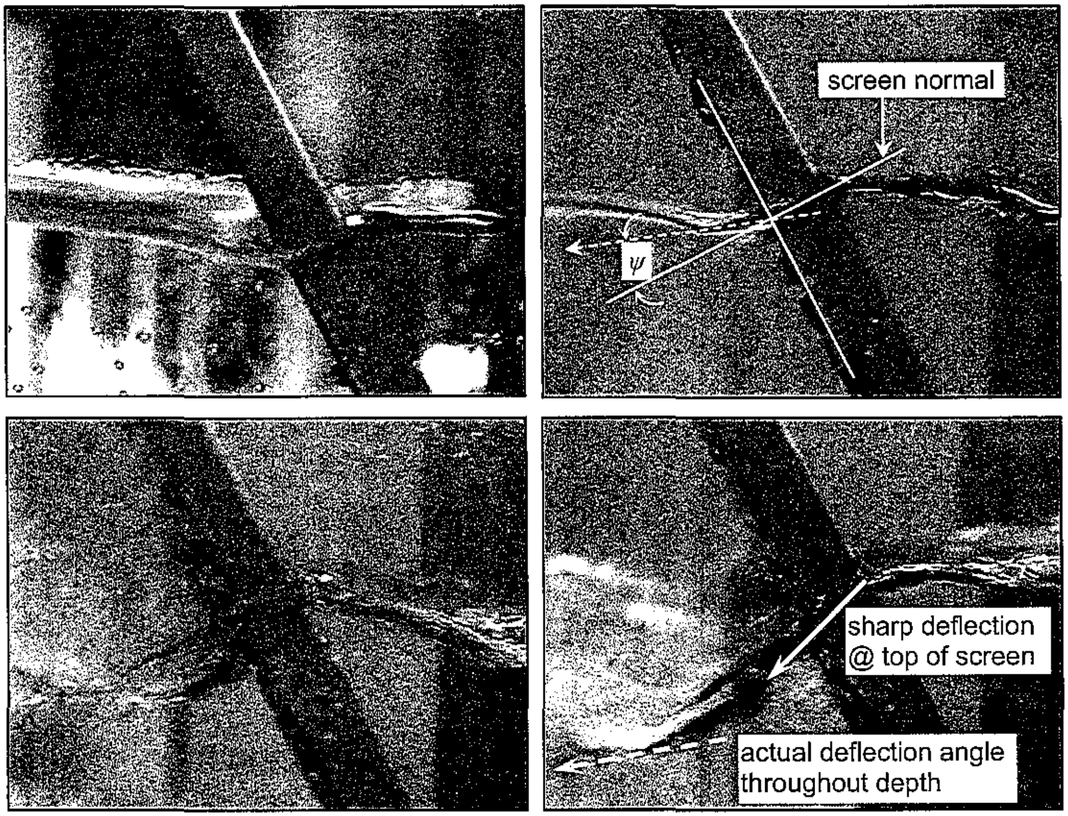

Figure 4.4. Flow deflection at 30° (clockwise from top-left, A = 7.5, 10, 50, & 30mm).

The deflection angle should not be confused with the sharp angle visible across the aluminum vertical stiffener, this angle is the initial acute deflection at the top of the screen and is not representative of the smaller deflection angle(s) along the screen height, which is more evident in the higher amplitude photos as the water splashes through the screen (50mm, Figure 4.4). Similar deflection behaviour is shown through flow-visualization by Yeh and Shrestha (1989); in particular, they show that the top deflection of a vertical screen is not representative of the deflection throughout the height, which is zero for a vertical screen. The contracted flow velocity, u_c, at the leeward side of an inclined screen is greater than the incident velocity, u_I. According to the Bernoulli theorem the pressure in front of the screen must be greater than that at its leeward side, which creates a vertical pressure gradient owing to the screen inclination and causes the flow deflection toward the normal direction of the screen along the screen height (Yeh and Shrestha 1989). Although the photos shown in Figure 4.3 and Figure 4.4 were taken at resonance, the deflection angle was observed to be relatively consistent over the frequency sweep and any additional analysis of change in ψ with frequency (or velocity) is not considered in this study (Taylor and Batchelor 1949).

To summarize, presented below—and plotted in Figure 4.5—are the three equations introduced in this section to estimate the pressure-loss coefficient,

$$C_{\theta_1} = C_l \cos^2\theta \qquad \text{(a)}$$

$$C_{\theta_2} = C_l \cdot \gamma_\theta = C_l\left(0.46\theta^3 - 1.05\theta^2 - 0.06\theta + 1\right) \qquad \text{(b)} \qquad (4.14)$$

$$C_{\theta_3} = \left(\frac{\cos\theta}{C\cdot\cos\psi} - 1\right)^2 \qquad \text{(c)}$$

As can be seen in Figure 4.5, $C_{\theta 2}$ reflects the curve of $C_{\theta 1}$ except for $\theta > 45°$ that is the range of the adjustments for the $\cos^2\theta$ losses made by Carrothers and Baines (1965). $C_{\theta 3}$, the loss coefficient developed in this study, is plotted with various ψ/θ values, with 0.6 being the lowest bound essentially limited by the $\cos^2\theta$ losses and 0.9 being selected as upper bound since, theoretically, $\psi \neq \theta$ or $\psi/\theta \neq 1$. Given the knowledge that $C_{\theta 1}$ tends to underestimate the pressure-loss at practical high screen angles ($45° \leq \theta \leq 70$), $C_{\theta 2}$ and $C_{\theta 3}$ both appear to estimate the pressure-loss coefficient more accurately, particularly $C_{\theta 3}$ with $\psi(\theta)$.

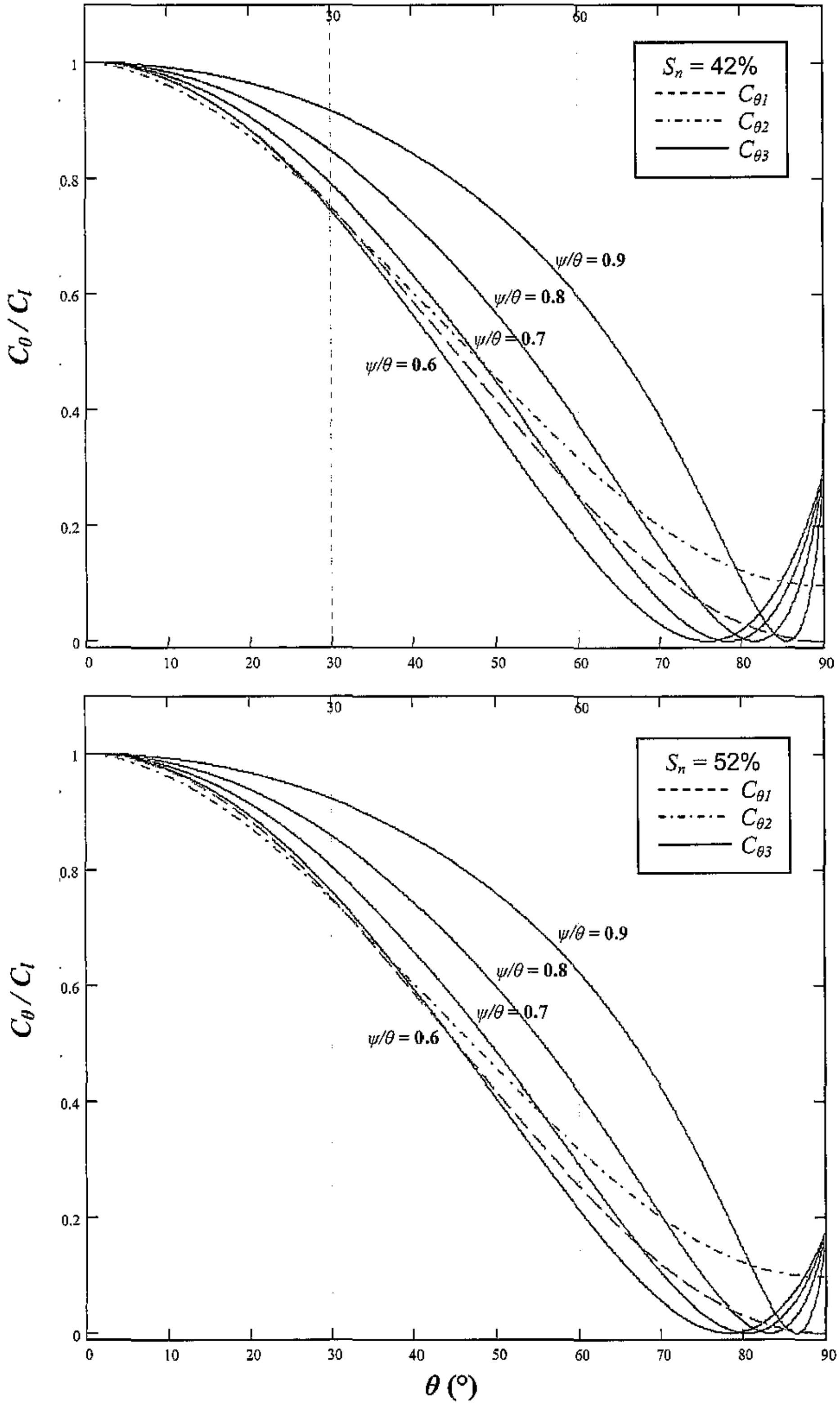

Figure 4.5. Normalized various C_θ from Equation (4.14) for both screens.

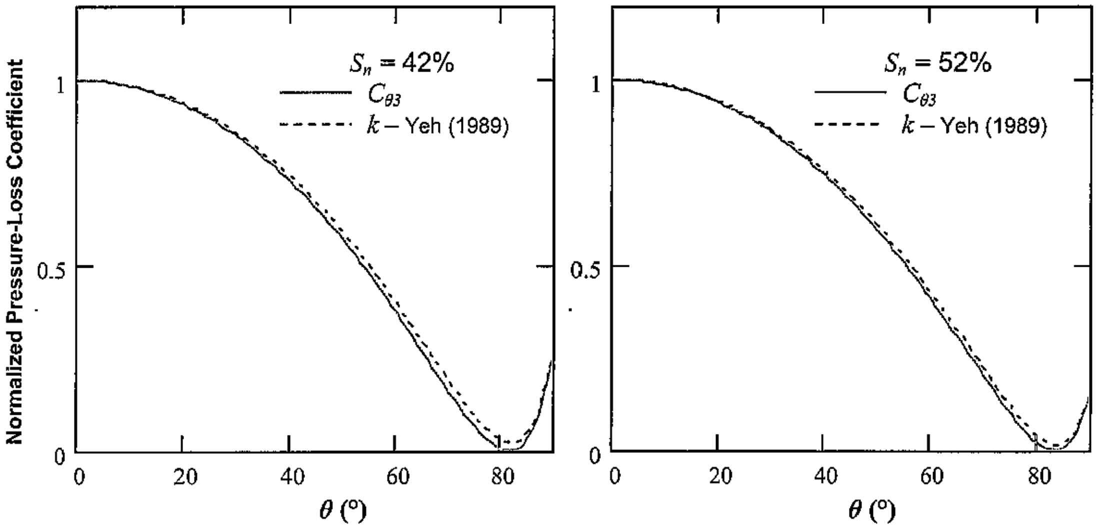

Figure 4.6. Comparison of pressure-loss coefficients, $C_{\theta 3}$ vs. k from Yeh (1989).

Figure 4.6 compares the pressure-loss coefficient of Equation (4.13) for both S_n versus that of Yeh and Shrestha (1989). The pressure-loss coefficients are normalized by their respective loss coefficient at 0°. The formulation of the pressure-loss coefficient, denoted as k by Yeh and Shrestha (1989), has been reproduced (ψ/θ = 0.80) at Λ = 0.005 (u_1 = 0.12m/s) with the properties for both sets of screens used in this study. k is a function of the approach velocity, u_1; however, this sensitivity is small for a large range of excitation and $C_{0°} \approx k$ especially at low excitation amplitudes ($\Lambda \leq 0.010$), which is suitable for linear models such as those used in this study. $C_{\theta 3}$ is found to be in good agreement with k for both the 42% and 52% screens. For the practical values of $0.40 \leq S \leq 0.60$ and $\theta \leq 60°$ used in this study, Figure 4.6 suggests that $C_{\theta 3}$ is valid. Note that $\theta > 70°$ is not recommended for practical application and is ignored in this study.

4.4 Linear Shallow Water Wave Theory Model Description

A modified linear model similar to the linear model developed by Fediw (1992) for steady-state sinusoidal excitation is described in this section. It is the initial simulation model used in this study (Cassolato and Tait 2005). The difference between the formulation by Fediw (1992) and the one presented here is the equations of motion are formulated directly using the fluid velocity, u, instead of the fluid particle displacement, e, which is intended to be a more representative formulation based on the assumption of average fluid velocity through the fluid depth. The theory assumes that the wave height, η, is small in comparison to the mean water level, h, and that the water is inviscid, irrotational, and incompressible. Moreover, given that this is a first-order linear analysis, all higher-order terms are neglected. By applying these additional assumptions to the non-linear shallow water equations, the well-known *one-dimensional* (1-D) linear wave equation is obtained,

$$\frac{\partial^2 u}{\partial t^2} - gh\frac{\partial^2 u}{\partial x^2} = 0 \tag{4.15}$$

From kinematics, the wave height, η, can be determined via,

$$\frac{\partial \eta}{\partial t} = -h\frac{\partial u}{\partial x} \tag{4.16}$$

where η is a function of time, t, and space, x.

The tank is divided into a number of subtanks, *i*, defined by the tank end walls and the screen locations. For this study, the tank containing the two 42% or two 52% damping screens would be divided into three subtanks as shown in Figure 4.7.

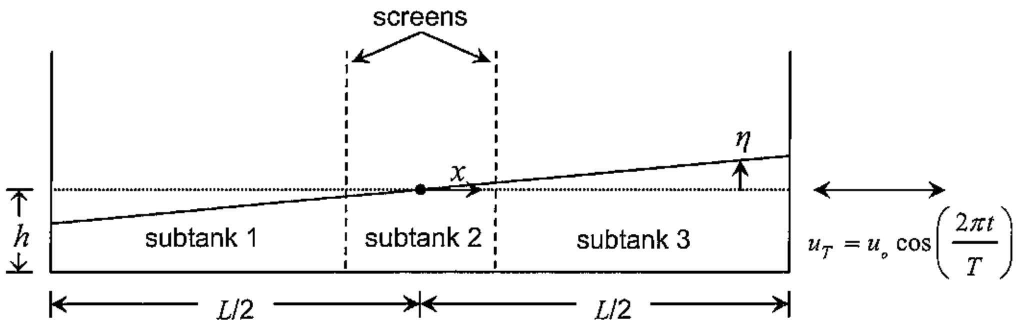

Figure 4.7. Shallow water wave theory linear model notation & coordinate system.

For the subtank arrangement in Figure 4.7, the average fluid velocity through the depth, $u(x,t)$, in any subtank satisfying Equation (4.15) can be expressed as

$$\begin{aligned} u_i(x,t) = {} & A_{4(i-1)+1}\cos\left(\frac{2\pi x}{\lambda}-\frac{2\pi t}{T}\right)+A_{4(i-1)+2}\cos\left(\frac{2\pi x}{\lambda}+\frac{2\pi t}{T}\right) \\ & +A_{4(i-1)+3}\sin\left(\frac{2\pi x}{\lambda}-\frac{2\pi t}{T}\right)+A_{4(i-1)+4}\sin\left(\frac{2\pi x}{\lambda}+\frac{2\pi t}{T}\right) \end{aligned} \tag{4.17}$$

where T is the period of excitation, i is the subtank number, and the A constants are to be evaluated. Note that a general equation for N screens (and therefore $i = N+1$ amount of subtanks) can be derived as in Fediw (1992); however, the response equation used throughout for this model for each subtank is the one displayed in Equation (4.17).

The response is evaluated in each subtank with the A coefficients in each response equation. The coefficients are solved by applying the following boundary conditions on the liquid motion: (1) the velocity of the fluid at the ends of the tank walls equals the input excitation velocity; (2) the velocity of the fluid into a screen equals the velocity out of the screen (assuming $\Delta\eta << h$); and (3) the pressure-loss across a screen (or drop in wave height, η) is equal to a linearized velocity loss coefficient, C_u, times the relative velocity across the screen, where C_u is (Tait 2005)

$$C_u = \frac{8}{3\pi}\frac{C_\theta}{2g}\left(u_{i+1} - u_T\right) \tag{4.18}$$

where u_T is the excitation velocity (tank velocity) and C_θ is the pressure-loss coefficient (for a vertical or inclined screen). The linearized velocity loss coefficient, C_u, is solved by iteration along with the unknown coefficients of Equation (4.17) in the subtank response equations. Applying the above boundary conditions and equating coefficients results in 12 ($4i$) equations or a 12×12 ($4i \times 4i$) matrix equation with constants A_1 through A_{12} to be solved. A computer program using MATLAB has been written, which calculates the constants along with the corresponding wave heights, η, resulting sloshing forces, F_{sw}, base shear forces, F_w, and total energy dissipated by the TLD, E_w. Once an initial value of C_u was assumed, it was found that C_u converged to a unique solution for all simulations considered in this study. The program completes execution within a few seconds. The overall solution is solved with a fine frequency sweep to produce smooth theoretical frequency-response curves and time histories of the various response parameters such as η or E_w', for example.

4.5 Potential Flow Theory Linear Model Description

This section describes the second flow model utilized in this study, one that is more complex than the linear shallow water wave theory model outlined in the previous section. It was developed to determine the damping ratio of the TLD and the response of the sloshing fluid including discrete vertical and horizontal fluid velocities. Moreover, a method developed that separates the horizontal and vertical damping components due to an inclined screen is presented and the impact of the vertical damping component is addressed.

4.5.1 Sloshing Fluid Response Equations

The coordinate system employed in this section is shown below in Figure 4.8.

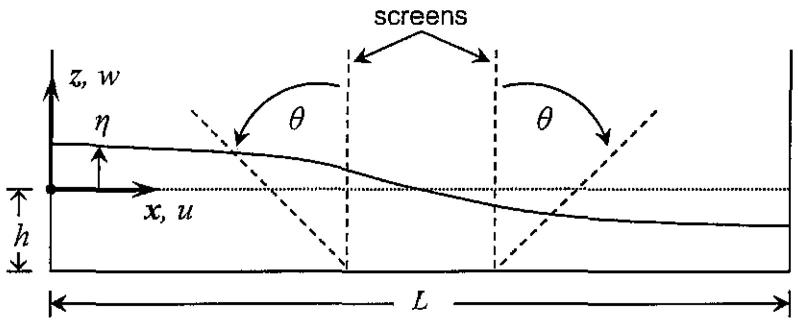

Figure 4.8. Potential flow linear model notation and coordinate system.

For a given input excitation amplitude, the fluid undergoes a sloshing motion with damping provided by the damping screens at a particular angle, which is formulated in §4.5.2. Although the characteristics of liquid sloshing in a TLD are non-linear, this model is intended to provide an initial linearized estimate of the steady-state fluid response—as with the previous model (§4.4). As in the previous section, the assumption of inviscid, incompressible, irrotational flow, and negligible surface tension are made. Additionally, it is assumed that the screens do not alter the overall flow of the sloshing fluid. The velocity of a liquid particle relative to the tank can be expressed as a gradient velocity potential, $\Phi(x,z,t)$. By kinematic continuity of incompressible flow,

$$\frac{\partial^2\Phi}{\partial x^2}+\frac{\partial^2\Phi}{\partial z^2}=0 \qquad \text{(Laplace's Equation)} \qquad (4.19)$$

The kinematic boundary conditions, fluid velocity equals zero at the tank walls and bottom, are given as

$$\begin{aligned} u(x,z,t)\big|_{x=0,x=L} &= \left.\frac{\partial\Phi}{\partial x}\right|_{x=0,x=L} = 0 \qquad &\text{(a)} \\ w(x,z,t)\big|_{z=-h} &= \left.\frac{\partial\Phi}{\partial z}\right|_{z=-h} = 0 \qquad &\text{(b)} \end{aligned} \qquad (4.20)$$

The linearized boundary condition at the free surface is given as

$$\frac{\partial\eta}{\partial t}=\left.\frac{\partial\Phi}{\partial z}\right|_{z=0} \qquad (4.21)$$

The potential, Φ, which satisfies the above boundary conditions, can be expressed in the generalized form as a sum of infinite sloshing modes,

$$\Phi(x,z,t)=\dot{q}_n(t)\cdot\cos\frac{n\pi x}{L}\cdot\frac{\cosh\frac{n\pi(z+h)}{L}}{\frac{n\pi}{L}\sinh\frac{n\pi h}{L}} \tag{4.22}$$

where the free surface is expressed as,

$$\eta(x,t)=\sum_{n=1}^{\infty}q_n(t)\cos\frac{n\pi x}{L} \tag{4.23}$$

The kinematics of liquid sloshing can be completely described by the set of generalized coordinates, $q_n(t)$, where n = 1, 2, 3,… (Warnitchai and Pinkaew 1998). The energy of a system of simple harmonic standing waves can be expressed in terms of the gravitational and kinematic energy (Coulson and Jeffrey 1977), respectively,

$$\begin{aligned} &V=\frac{1}{2}\rho bg\int_0^L\eta^2(x,t)dx && \text{(a)} \\ &T=\frac{1}{2}\rho b\int_{-h}^{0}\int_0^L\left[\left(\dot{X}+\frac{\partial\Phi}{\partial x}\right)^2+\left(\frac{\partial\Phi}{\partial z}\right)^2\right]dxdz && \text{(b)} \end{aligned} \tag{4.24}$$

where $\dot{X}$ is the horizontal velocity of the structure at the TLD location.

4.5.2 Influence of Damping Screens

Screens are placed at discrete locations inside the tank, x_j, with constant pressure-loss and inertia coefficients, C_θ and C_m, respectively. The force exerted by the fluid on the screens can be expressed as the addition of a drag component proportional to the square of the velocity and a virtual mass component proportional to the horizontal component of the acceleration force exerted on the mass of the liquid displaced by the screen (Morison et al. 1950)

$$f(x,z,t) = f_D(x,z,t) + f_i(x,z,t) \tag{4.25}$$

This conservative inertial force, f_i, dissipates no energy; however, it does contribute to the overall kinetic energy of the sloshing liquid, which is given by (Warnitchai and Pinkaew 1998),

$$f_i(x_j,z,t) = \rho A_{cs} C_m \frac{\partial u(x_j,z,t)}{\partial t} \tag{4.26}$$

Since the inertial component of a thin sharp-edged horizontal-slat screen is insignificant and negligibly affects the fluid energy, it will not be considered in this study (Tait 2004).

The horizontal drag force resulting in additional damping due to the insertion of a screen is given by (Warnitchai and Pinkaew 1998),

$$f_{D_n}(x_j,z,t) = \frac{1}{2}\rho b_s C_\theta \sin^2\frac{n\pi x_j}{L}\left[\frac{\cosh\frac{n\pi(z+h)}{L}}{\sinh\frac{n\pi h}{L}}\right]^2 \left|\dot{q}_n(t)\right|\dot{q}_n(t) \tag{4.27}$$

Applying virtual work by the non-conservative drag forces acting through virtual displacements by variations in the generalized coordinates, $q_n(t)$ (Tait 2007), in discreet x and z directions leads to

$$\begin{aligned}\delta q_{nx}(x_j,z,t) &= -\frac{\cosh\dfrac{n\pi(z+h)}{L}}{\sinh\dfrac{n\pi h}{L}}\cdot\sin\frac{n\pi x_j}{L}\cdot\delta q_n(t)\\ \delta q_{nz}(x_j,z,t) &= \frac{\sinh\dfrac{n\pi(z+h)}{L}}{\sinh\dfrac{n\pi h}{L}}\cdot\cos\frac{n\pi x_j}{L}\cdot\delta q_n(t)\end{aligned}\tag{4.28}$$

$$\delta W_{nc} = -\sum_{j=1}^{ns}\int_{-h}^{0} f_{D_{nx}}\cdot\delta q_{nx}(x_j,z,t) + f_{D_{nz}}\cdot\delta q_{nz}(x_j,z,t)dz$$

$$\begin{aligned}\delta W_{nc} = \Bigg[& -\frac{1}{2}\rho b_s C_\theta\sum_{j=1}^{ns}\sin^3\frac{n\pi x_j}{L}\int_{-h}^{0}\left(\frac{\cosh\dfrac{n\pi(z+h)}{L}}{\sinh\dfrac{n\pi h}{L}}\right)^3 dz\left|\dot{q}_n(t)\right|\dot{q}_n(t)\\ & -\frac{1}{2}\rho b_s C_{\theta z}\sum_{j=1}^{ns}\cos^3\frac{n\pi x_j}{L}\int_{-h}^{0}\left(\frac{\sinh\dfrac{n\pi(z+h)}{L}}{\sinh\dfrac{n\pi h}{L}}\right)^3 dz\left|\dot{q}_n(t)\right|\dot{q}_n(t)\Bigg]\cdot\delta q_n(t)\end{aligned}\tag{4.29}$$

where the pressure-loss coefficient in the z-direction, $C_{\theta z}$, is formulated in the same manner as the horizontal pressure-loss coefficient but with the assumption that the loss characteristics in the vertical direction are 90° to the x-direction, i.e.,

$$C_{\theta z} = C_\theta\left(\theta = \frac{\pi}{2} - \theta\right)\tag{4.30}$$

It is important to recognize that the angled screens span over the height *and* length of the tank. Following Figure 4.9, in order to capture the effect of the damping force over the length *and* height of an angled screen, the following equation for the variation of the non-conservative drag force of the screen over x and z is introduced,

$$x_j(x_j, z, h, \theta) = x_j + (z+h)\tan\theta \qquad (4.31)$$

Also, for another screen such as the one depicted on the left of Figure 4.8, taking into account the coordinate system and its symmetry to the one shown in Figure 4.9, a similar equation for that screen spanning the length of the tank is simply,

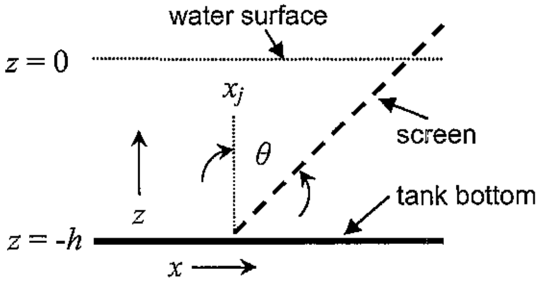

Figure 4.9. Angled screen detail.

$$x_j(x_j, z, h, \theta) = x_j - (z+h)\tan\theta \qquad (4.32)$$

Introducing nomenclature to simplify Equation (4.29),

$$\delta W_{nc} = Q_n \cdot \delta q_n$$

results in the non-conservative damping force, Q_n, for angled screens derived from potential flow theory,

$$\begin{aligned} Q_n = &-\frac{1}{2}\rho b_s C_\theta \int_{-h}^{0} \sum_{j=1}^{ns} \sin^3 \frac{n\pi(x_j \pm (z+h)\tan\theta)}{L} \left(\frac{\cosh\frac{n\pi(z+h)}{L}}{\sinh\frac{n\pi h}{L}} \right)^3 dz |\dot{q}_n| \dot{q}_n \\ &-\frac{1}{2}\rho b_s C_{\theta z} \int_{-h}^{0} \sum_{j=1}^{ns} \cos^3 \frac{n\pi(x_j \pm (z+h)\tan\theta)}{L} \left(\frac{\sinh\frac{n\pi(z+h)}{L}}{\sinh\frac{n\pi h}{L}} \right)^3 dz |\dot{q}_n| \dot{q}_n \end{aligned} \qquad (4.33)$$

Note that ns is the number of screens, where $ns = 2$ in this study. Instead of the single integrand terms of Equation (4.29), which would be the case for a vertical screen (or $\theta = 0°$), the damping force for an angled screen incorporates two integrand terms both as a function of the variable of integration, z. To clarify, the notation $\Theta_{nx}(x_j, h, L, \theta)$ and $\Theta_{\mathrm{nz}}(x_j, h, L, \theta)$ are introduced, which are the integration terms of Equation (4.33),

$$\begin{aligned}
\Theta_{nx}(x_j,h,L,\theta) &= \int_{-h}^{0} \sum_{j=1}^{ns} \sin^3 \frac{n\pi(x_j \pm (z+h)\tan\theta)}{L} \left(\frac{\cosh \dfrac{n\pi(z+h)}{L}}{\sinh \dfrac{n\pi h}{L}} \right)^3 dz \quad \text{(a)} \\
\Theta_{nz}(x_j,h,L,\theta) &= \int_{-h}^{0} \sum_{j=1}^{ns} \cos^3 \frac{n\pi(x_j \pm (z+h)\tan\theta)}{L} \left(\frac{\sinh \dfrac{n\pi(z+h)}{L}}{\sinh \dfrac{n\pi h}{L}} \right)^3 dz \quad \text{(b)}
\end{aligned} \tag{4.34}$$

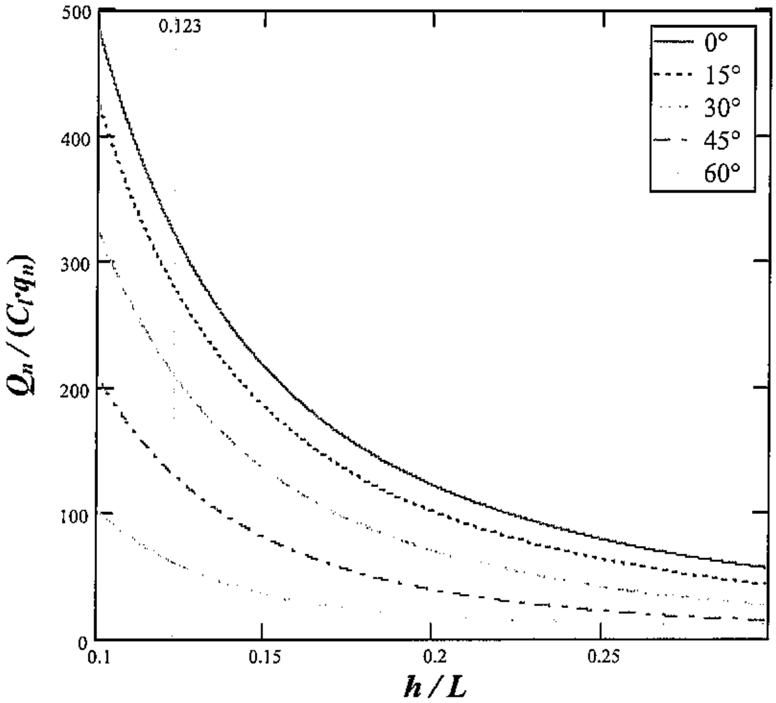

Figure 4.10. Damping force versus depth ratio.

While no relatively simple closed-form algebraic simplification of this integration—or Equation (4.33)—was found in this study, the onerous result can be computed using advanced symbolic mathematics programs such as Mathcad.

The normalized damping force, Q_n, is plotted in Figure 4.10 versus the depth ratio, in the typical design range of $0.1 \leq h/L \leq 0.3$, for all angles. Q_n utilizes $C_{\theta 2}$ and is normalized by $C_l \cdot q_n$. The depth ratio used in this study, h/L = 119mm/966mm = 0.123, is marked in Figure 4.10. The figure clearly shows that the model's damping force decreases with increasing screen angle. The decreasing trend with increasing h/L depicts the model's ability to account for the variation of velocity through the fluid depth *and* along the tank length.

4.5.3 Generalized TLD Properties

The generalized response of the liquid sloshing can be determined using Lagrange's equations of motion, which are expressed as,

$$\frac{\partial}{\partial t}\left(\frac{\partial T}{\partial \dot{q}_n}\right) - \frac{\partial T}{\partial q_n} + \frac{\partial V}{\partial q_n} = Q_n \tag{4.35}$$

T and V are the total kinetic and potential energy of the system, respectively, as defined in Equation (4.24). The ensuing equations of motion are,

$$m_n^* \ddot{q}_n(t) + c_n^* \dot{q}_n(t) + k_n^* q_n(t) = \gamma_n^* \ddot{X}(t) \tag{4.36}$$

where the generalized mass is,

$$m_n^* = \frac{1}{2} \frac{\rho b L^2}{n\pi \tanh \dfrac{n\pi h}{L}} \tag{4.37}$$

the generalized stiffness is,

$$k_n^* = \frac{1}{2} \rho b L g \tag{4.38}$$

the corresponding modal natural frequency from $\omega_n{}^2 = \dfrac{k_n^*}{m_n^*}$ is,

$$\omega_n = \sqrt{\frac{n\pi g}{L}\tanh\frac{n\pi h}{L}} \tag{4.39}$$

and the generalized excitation factor is,

$$\gamma_n^* = \rho b\left(\frac{L}{n\pi}\right)^2 (1-\cos n\pi) \tag{4.40}$$

The modal participation factor can be expressed as,

$$\Gamma_n = \frac{\gamma_n^*}{m_n^*} = \frac{2}{n\pi}(1-\cos n\pi)\tanh\frac{n\pi h}{L} \tag{4.41}$$

4.5.4 Linearization of Damping Term

The generalized damping term from the equations of motion, Equation (4.36), is found to be,

$$c_n^* = \frac{1}{2}\rho b\left(C_\theta \Theta_{nx} + C_{\theta z}\Theta_{nz}\right)\left|\dot{q}_n\right| \tag{4.42}$$

where Θ_{nx} and Θ_{nz}, Equation (4.34), are the integrands in the damping force, Q_n. A method for formulating an equivalent linear viscous damping, c_{eq}^*, for a sinusoidal excitation can be found in Chopra (2001) and is applied here to yield,

$$c_{eq}^* = \frac{4}{3\pi}\rho b\left(C_\theta \Theta_x + C_{\theta z}\Theta_z\right)\left|\dot{q}\right| \tag{4.43}$$

For simplicity, in the linear analysis only the first mode is considered, i.e., $n = 1$. The corresponding equivalent linear viscous damping ratio is,

$$\zeta_{eq} = \frac{4}{3L^2}\left(C_\theta \Theta_x + C_{\theta z}\Theta_z\right)\tanh\frac{\pi h}{L} q = \zeta_o \cdot q \tag{4.44}$$

where $\zeta_o = \zeta_{ox} + \zeta_{oz}$ and,

$$\zeta_{ox} = \frac{4}{3L^2} C_\theta \Theta_x \tanh\frac{\pi h}{L} \quad \text{and} \quad \zeta_{oz} = \frac{4}{3L^2} C_{\theta z}\Theta_z \tanh\frac{\pi h}{L}$$

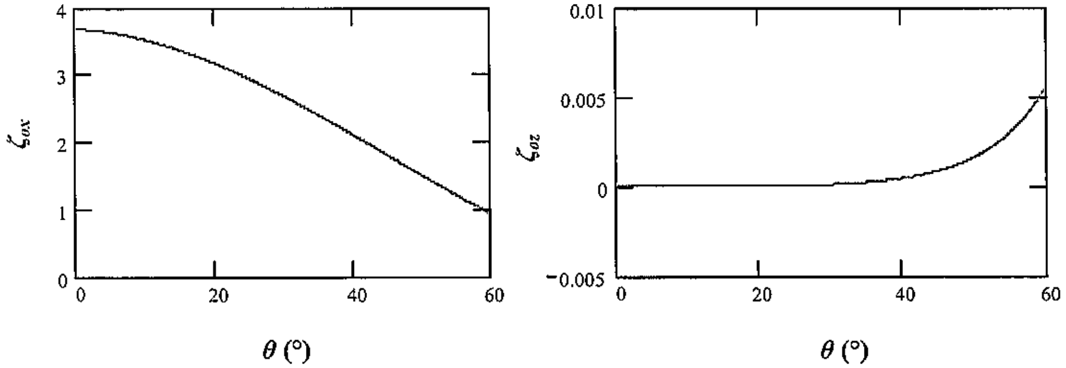

Figure 4.11. *x*- and *z*-components of equivalent linear viscous damping ratio.

The *x*- and *z*-components of the linearized damping ratio, ζ_{ox} and ζ_{oz}, respectively, are shown separately in Figure 4.11 (for the tank used in this study equipped with 42% screens utilizing $C_{\theta 2}$) versus screen angle. Evident in this figure is the dominance of the horizontal component, even at 60°, which shows that the vertical damping component is negligible and the dominance of the horizontal (or normal) component. However, in fullness for this study on angled damping screens, the vertical damping component is included whenever potential flow theory is used for simulation or comparison with experimental results.

For completeness, the boundary layer damping provided by the viscosity of the water is also included and is expressed as (Sun 1992),

$$\zeta_w = \frac{1}{2h}\sqrt{\frac{\nu}{2\omega_n}}\left(1+\frac{2h}{b}+SC\right) \tag{4.45}$$

where ν is the kinematic viscosity of water and SC is a surface contamination factor, often taken as unity (Miles 1967).

4.5.5 Equivalent Tuned Mass Damper Response Equations

This subsection formulates the response of the sloshing fluid of the TLD with damping screens, permitting it to be modelled as an equivalent linear *tuned mass damper* (TMD). The TLD is subjected to a sinusoidal base excitation, $X(t)$, with amplitude, A, and frequency, ω,

$$X(t) = A\sin\omega t \tag{4.46}$$

The steady-state response solution, $q(t)$, of the generalized coordinates, $q_n(t)$, is

$$q(t) = q_o\sin(\omega t-\varphi) \tag{4.47}$$

where φ is the phase angle with the forced frequency ratio, $\beta = \omega/\omega_n$,

$$\varphi = \tan^{-1}\left(\frac{2\zeta_{eq}\beta}{1-\beta^2}\right) \tag{4.48}$$

q_o is the response amplitude,

$$q_o = \frac{\beta^2\Gamma A}{\sqrt{\left(1-\beta^2\right)^2+\left(2\zeta_{eq}\beta\right)^2}} \tag{4.49}$$

Since $\zeta_{eq} = \zeta_o \cdot q_o$, the solution to Equation (4.49) can be expressed as (Tait 2007),

$$q_o = \sqrt{\frac{2\Gamma^2 A^2 \beta^4}{\left(1-\beta^2\right)^2 + \sqrt{\left(1-\beta^2\right)^4 + \left(4\beta^3 \zeta_o \Gamma A\right)^2}}} \tag{4.50}$$

The dynamic sloshing force, $F_{sw}(t) = m_{eff} \cdot \ddot{x}_r(t)$, can be found by calculating the effective mass, m_{eff}, and applying a coordinate relationship to the relative motion, x_r, for an equivalent linear TMD,

$$q(t) = \Gamma \cdot x_r(t) \tag{4.51}$$

The effective mass is defined as,

$$m_{eff} = \frac{\left(\gamma_n^*\right)^2}{m_n^*} = \frac{8}{\pi^3}\rho b L^2 \tanh\frac{\pi h}{L} \qquad (n=1) \tag{4.52}$$

Therefore, the sloshing force is found to be,

$$F_{sw}(t) = 2\rho b\left(\frac{L}{\pi}\right)^2 \omega^2 q(t) = \gamma^* \omega^2 q_o \sin\left(\omega t - \varphi\right) \tag{4.53}$$

The corresponding base shear force including the inertial component of the water mass is then,

$$F_w(t) = F_{sw}(t) + m_w \omega^2 A \sin\omega t \tag{4.54}$$

The energy dissipated by the base shear force of the water sloshing motion, E_w, is defined as the work done by this force during one cycle of the base excitation, T,

$$E_w = \int_T F_w(t)dx = \left(\gamma^* \omega^2 q_o\right) A\pi \sin\varphi = 2\rho b\left(\frac{L}{\pi}\right)^2 \omega^2 q_o A\pi \sin\varphi \tag{4.55}$$

Close inspection of Equation (4.55) reveals that the conservative force of the water mass, $m_w\omega^2 A\sin\omega t$, dissipates no energy. These equations permit rapid generation of frequency-response curves. This is carried out in §4.7 and the experimental results are compared with simulations based on potential flow theory and linear shallow water wave theory.

4.6 Experimental Evaluation of Drag Coefficient for Vertical Screens (0°)

As the first section of the experimental results presented in this chapter, the drag coefficient, C_D, for vertical screens (0°) is evaluated experimentally and compared to theoretical formulations. As mentioned before, the theoretical drag coefficients presented earlier were formulated based on steady open-channel flow. This section validates the application of these equations to oscillating flow inside a TLD. The excitation amplitudes in these tests cover the range of serviceability accelerations for buildings subjected to wind loads (McNamara et. al 2002) and larger excitation amplitudes indicative of earthquake motion (Yu et al. 1999).

The tests are conducted as described in Chapter 2 with the tank mounted to a shake table (Figure 2.5) filled with water to a depth, h (Figure 2.1), with the screens located at $\pm 0.1L$ from the centre. The forces on the screens are measured using loads cells and the free-surface elevation is measured at two points near the ends of the tank walls (§2.4.1), as illustrated in Figure 4.1.

The following procedure is used to experimentally estimate the value of the drag coefficient, C_D, corresponding to a particular excitation amplitude, A, and frequency around the resonance frequency, f_n.

- The time history of the free surface elevation is measured at the ends of the tank by the two wave probes used to represent the generalized coordinate, q_n, for the fluid response. The free-surface profile of a TLD can be represented as a Fourier series at any instant in time, as shown earlier by Equation (4.23),

$$\eta(x,t) = \sum_{n=1}^{\infty} q_n(t) \cos\frac{n\pi x}{L}$$

where

$$q_n(t) = q_n \cos n\omega_n t \tag{4.56}$$

Only the fundamental response is taken ($n = 1$) to estimate the fluid velocity at the screen locations. q is taken as the measured free-surface response amplitude, η, the wave height measured at the location of the wave probes (Figure 4.1).

- The fluid velocity, $u(x,z,t)$, can be estimated from the velocity potential, $\Phi(x,z,t)$, as

$$u(x,z,t) = \frac{\partial\Phi}{\partial x} = \omega\eta \frac{\cosh\frac{\pi(z+h)}{L}}{\sinh\frac{\pi h}{L}} \sin\frac{\pi x}{L} \sin\omega t \tag{4.57}$$

- Equation (4.57) is integrated throughout the depth, z, divided by the depth, h, and simplified, to obtain the average fluid velocity, U(x,t),

$$U(x,t) = \frac{\eta\omega L}{\pi h} \sin\frac{\pi x}{L} \sin\omega t \tag{4.58}$$

- The location of a screen, x_j, is substituted in Equation (4.58) to obtain the amplitude of the average horizontal fluid velocity, U_o, at x_j,

$$U_o(x_j) = \frac{\eta \omega L}{\pi h} \sin \frac{\pi x_j}{L} \tag{4.59}$$

- As shown earlier in Equation (4.25), the force acting on a submerged body in oscillating flow is given by the Morison equation,

$$F = \frac{1}{2} \rho u |u| C_D D + C_m \rho \frac{\pi D^2}{4} \frac{\partial u}{\partial t} \tag{4.60}$$

which is a function of a drag and inertial component. In view of §4.5.2, the inertial component for thin horizontal-slat screens can be ignored and only the drag, C_D, is evaluated experimentally.

- Keulegan-Carpenter (1958) formulated an equation for determining the drag coefficient of a plate in oscillating flow as

$$C_D = -\frac{3}{4} \int_0^{2\pi} \frac{F(\theta) \cos \theta}{\rho U_o^2 d} d\theta \tag{4.61}$$

where $\theta = \frac{2\pi t}{T}$, $F(\theta)$ is the periodic force measured by the screen load cells, and T is the excitation period, $T = \frac{\omega}{2\pi}$.

The procedure described above is carried out over the practical range of amplitudes conducted in this study, $0.003 \geq \Lambda \geq 0.031$, where Λ is the non-dimensional excitation amplitude, $\Lambda = A/L$. C_D and C_l ($C_{0°}$) were calculated for both screen solidities. Keulegan and Carpenter (1958) found that the loss coefficients are related to a period parameter subsequently termed the *Keulegan-Carpenter number* (KC), defined as,

$$KC = \frac{U_o T}{d} \tag{4.62}$$

KC is a ratio between the fluid motion (U_o, T) and the size of the submerged body (d). Stated earlier in this chapter, steady flow represents the limiting case of oscillatory flow when KC becomes large. In fact, the transition point of this case is approximately $KC = 20$ for plates and C_D decreases very gradually over a large range of $KC < 125$ (Keulegan and Carpenter 1958). This is reflected in the experimentally determined pressure-loss coefficients found for this study in Figure 4.12. For the range of Λ values mentioned previously, the range of KC in this study is above 25 and therefore the drag losses associated with viscous effects, fluid separation, and turbulent wake formation past the submerged objects in the oscillatory nature of the fluid in this TLD is similar to the behaviour in steady flow. Both the 42% and 52% screens experimentally determined pressure-loss coefficients are presented in Figure 4.12 (corresponding C_D may be determined via Equation (4.5)). Both screens tend to reflect the expected behaviour of the gradual decrease in C_l over increasingly large KC.

Also plotted in Figure 4.12 is another experimental prediction of the drag coefficient from an energy-matching procedure that will be described here. The *potential flow* (PF) model described in §4.5 is implemented in a spreadsheet program to generate a theoretical non-dimensional frequency-response curve (β-E_w'). In an iterative calculation, this frequency-response curve is forced to

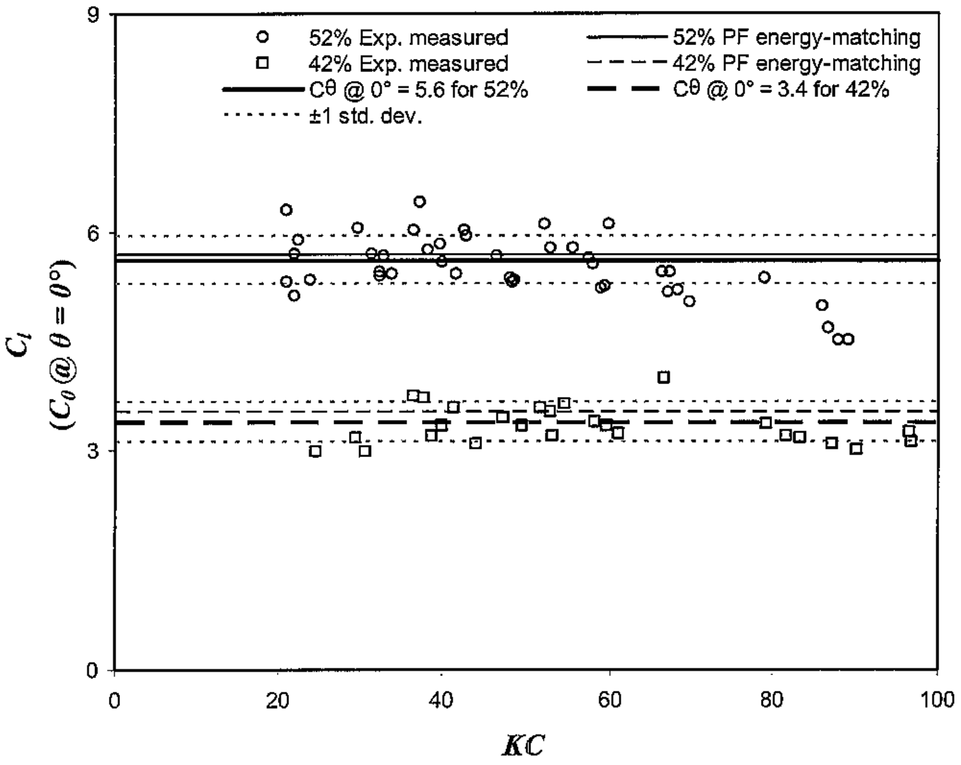

Figure 4.12. Comparison of C_l ($C_{0°}$) values versus *KC* values.

match with the experimental frequency-response curve solving for the loss coefficient (or equivalent solidity ratio, S_{eq}) while the sum of the square of the error between the predicted and experimental response at each frequency is minimized (a least-squares fit) and also matching the peak values of both frequency-response curves. The lines denoted "PF energy-matching" plotted in Figure 4.12 for each set of screens is an average value of C_θ (at 0°, $C_{0°}$) found using this energy-matching scheme over amplitudes $0.003 \leq \Lambda \leq 0.031$. The PF pressure-loss coefficient values of $C_{0°}$ fall within one standard deviation of the scatter of measured values for each set of screens.

From the experimental results, $C_{0^\circ} = 3.4$ and 5.6 are selected to be the loss coefficients for the set of 42% and 52% screens for this study, respectively, supported by the two methods described and these values are plotted in Figure 4.12. The screen coefficients and solidities are summarized in Table 4.2.

Table 4.2. Summary of Loss Coefficients and Solidities for $\theta = 0°$.

S_n	C_{0°	from Eq. (4.14) S_{eq}	PF $E_w{}'$-matching C_l	$\frac{A_s}{A_g}$	$\frac{A_s/A_g - S_{eq}}{S_{eq}}$
42%	3.4	0.485	3.53	0.4740	-2.27%
52%	5.6	0.554	5.69	0.5605	1.17%

A_s/A_g is also tabulated in Table 4.2, in addition to the percent difference between this value and the equivalent solidity, S_{eq}, which is determined from the selected loss coefficients via Equation (4.13). The measurement of the solidity (A_s/A_g) may not be entirely accurate given the location, size, and span of the floating frames and the hinges (§2.2). However, it is interesting to note that the difference between the measured solidity and S_{eq}—determined from an accurate evaluation of the overall physical losses of the screens, frames, and hinges combined—is quite small.

In conclusion to this section, the experimental screen loss coefficients, $C_{0^\circ} = 3.4$ and 5.6 will be used for the 42% and 52% screens, respectively. A corresponding drag coefficient, C_D, can be established in accordance with Equation (4.5) utilizing S_{eq}.

4.7 Comparison of Experimental Results with Linear Simulations

Comparisons between experimental results obtained via the testing procedure detailed in Chapter 2 and the two linear models described in this chapter are made. Three key parameters of TLD response are compared: free-surface response, the base shear force, and the overall average energy dissipated per cycle of excitation. First, a comparison between the different pressure-loss coefficients (Equation (4.14)) is addressed.

4.7.1 Frequency-Response Comparisons with Various C_θ

Three pressure-loss coefficients have been presented in this chapter, Equation (4.14), and their influence in predicting the frequency-response of the TLD is shown in Figure 4.13 and Figure 4.14. Due to the similarity between pressure-loss coefficients, $C_{\theta 1}$ and $C_{\theta 2}$, and the knowledge that $C_{\theta 1}$ underestimates fluid losses for $\theta \geq 45°$, $C_{\theta 1}$ will not be utilized.

Both figures display the non-dimensional energy, E_w' (Equation (3.5)), frequency-response curves for both sets of screens at amplitudes, Λ = 0.003, 0.005, 0.010, and 0.021, for angles 0°, 30°, and 60°. The experimental results are plotted along with simulations from the *potential flow theory model* (PF) of §4.5 and the *shallow water wave theory model* (SW) of §4.4 utilizing both $C_{\theta 2}$ ("Blev." in figures) and $C_{\theta 3}$. The deflection angle of $C_{\theta 3}$ that is used is $\psi = 0.80\theta$. For θ = 60°, $\psi = 0.90\theta$ is assumed for the 42% screens and $\psi = 0.85\theta$ is assumed for the 52% screens, in accordance with the discussion of Figure 4.3 and Figure 4.4.

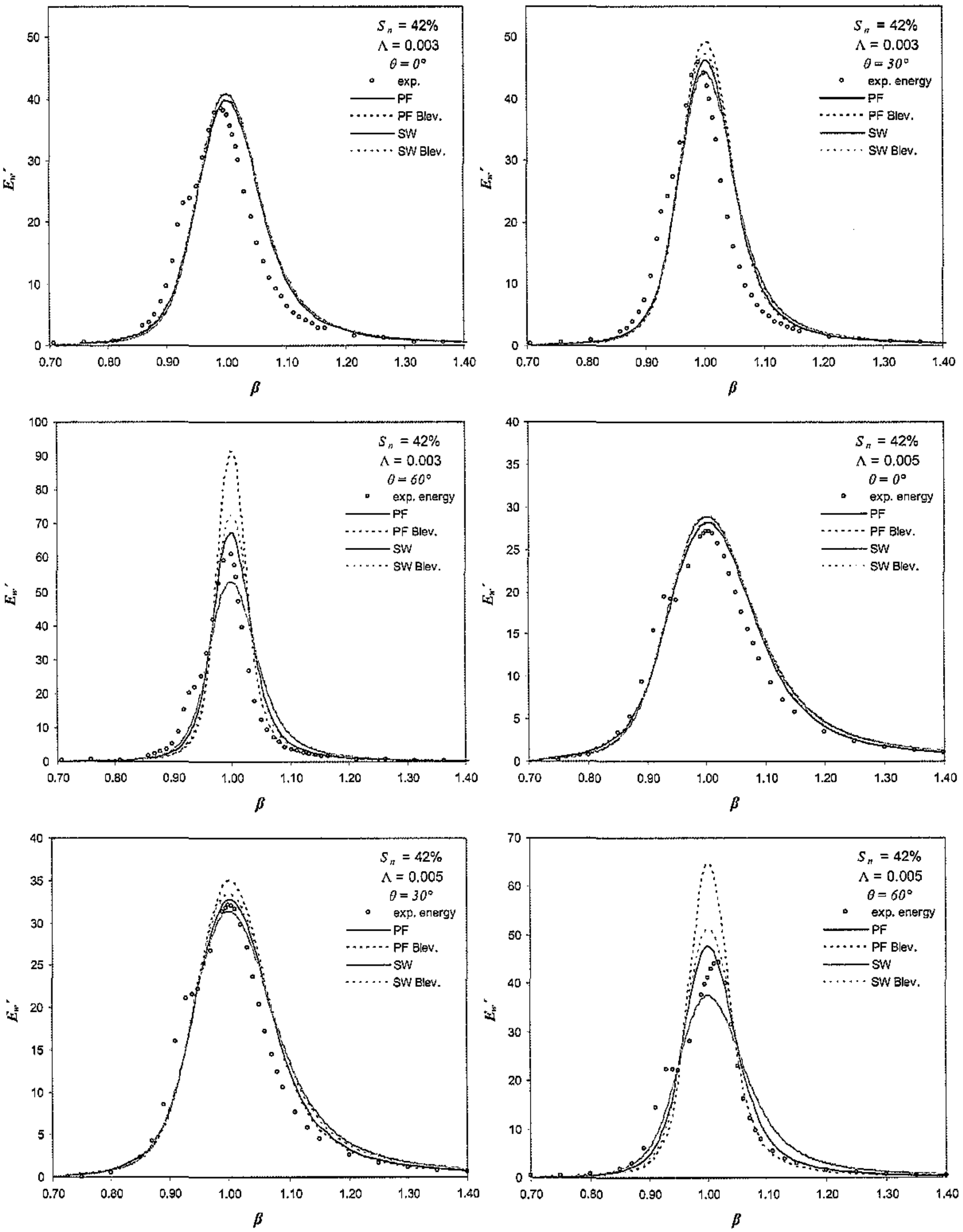

Figure 4.13. Impact of different C_0 on energy dissipation frequency-response, 42% screens.

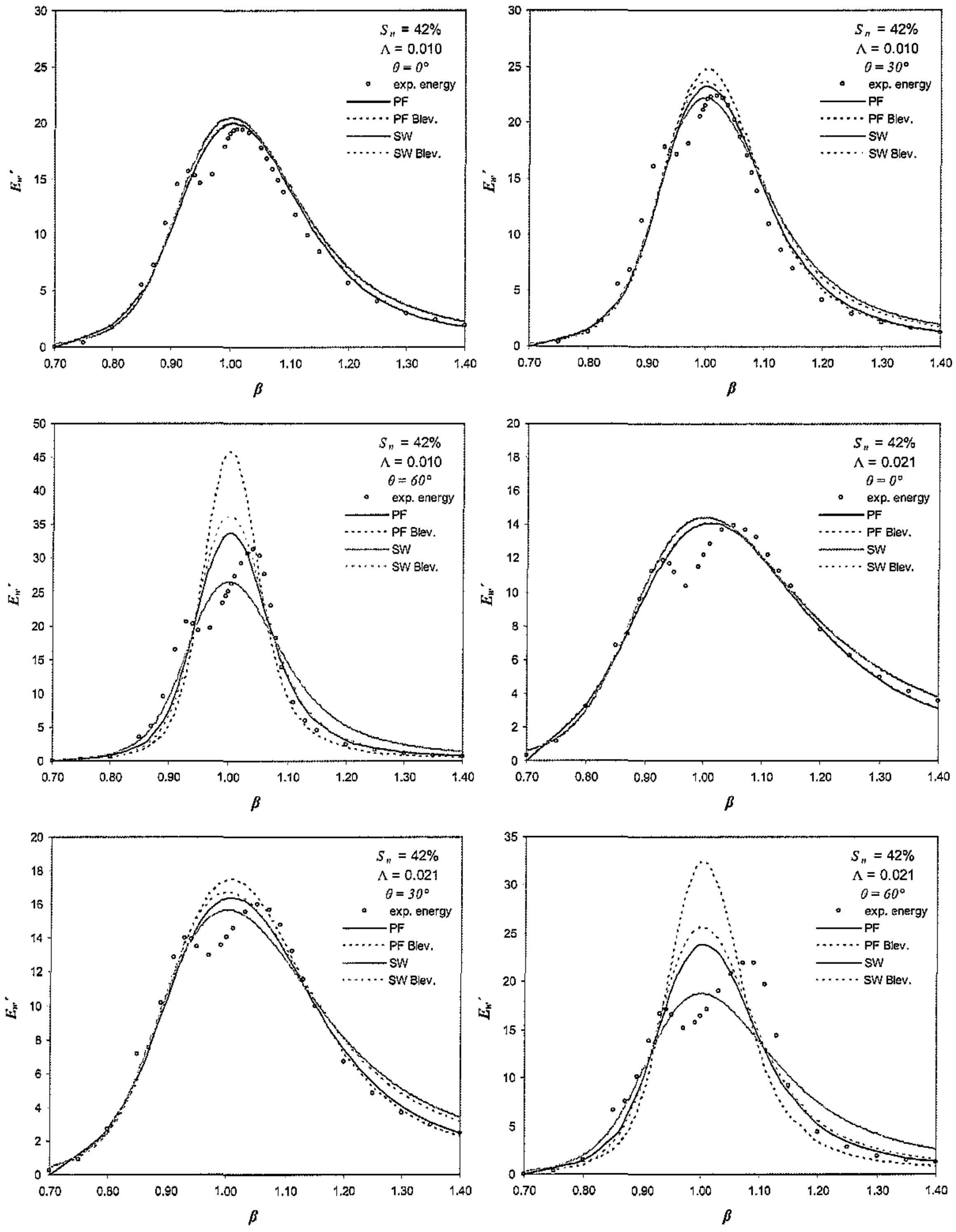

Figure 4.13 (continued).

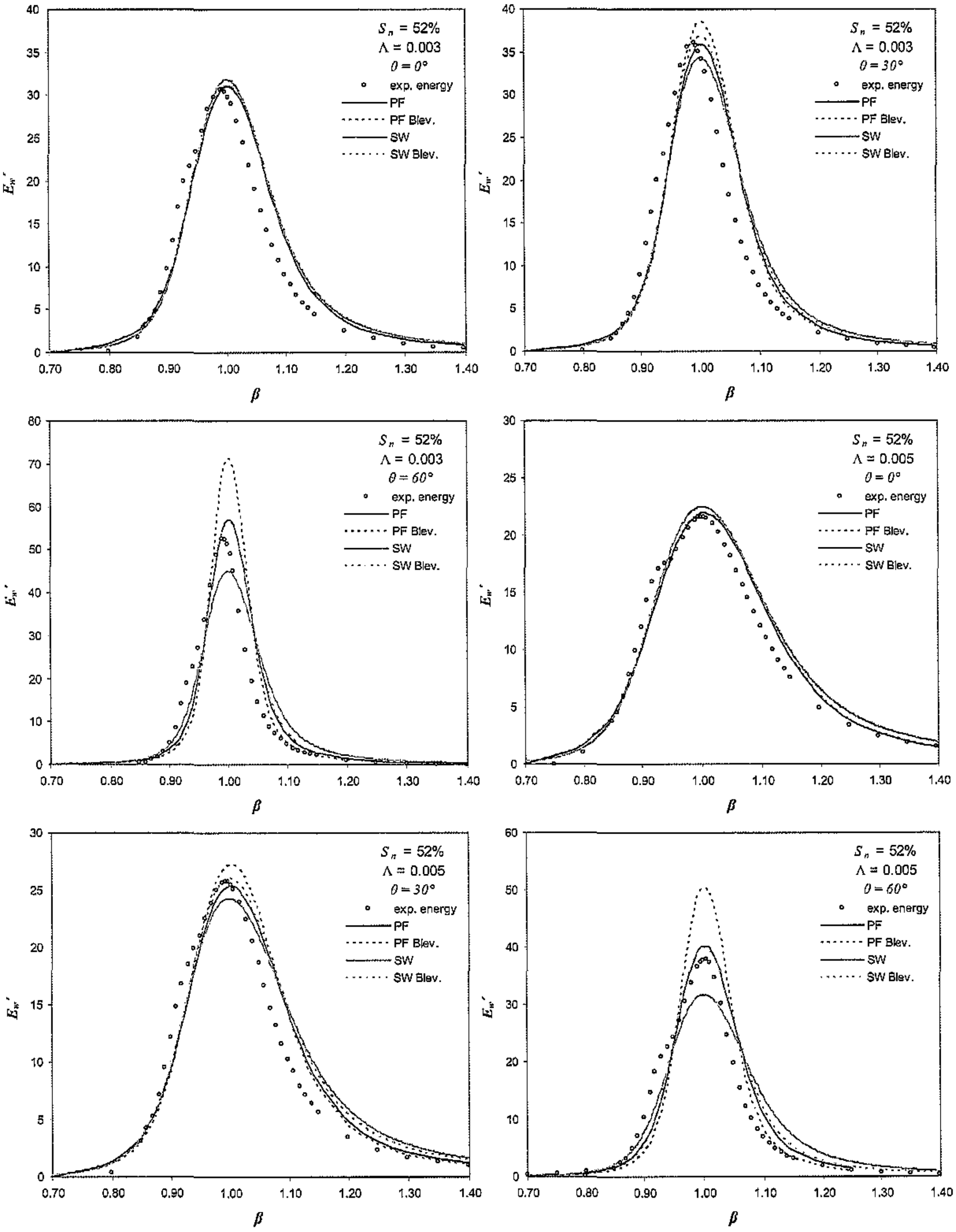

Figure 4.14. Impact of different C_0 on energy dissipation frequency-response, 52% screens.

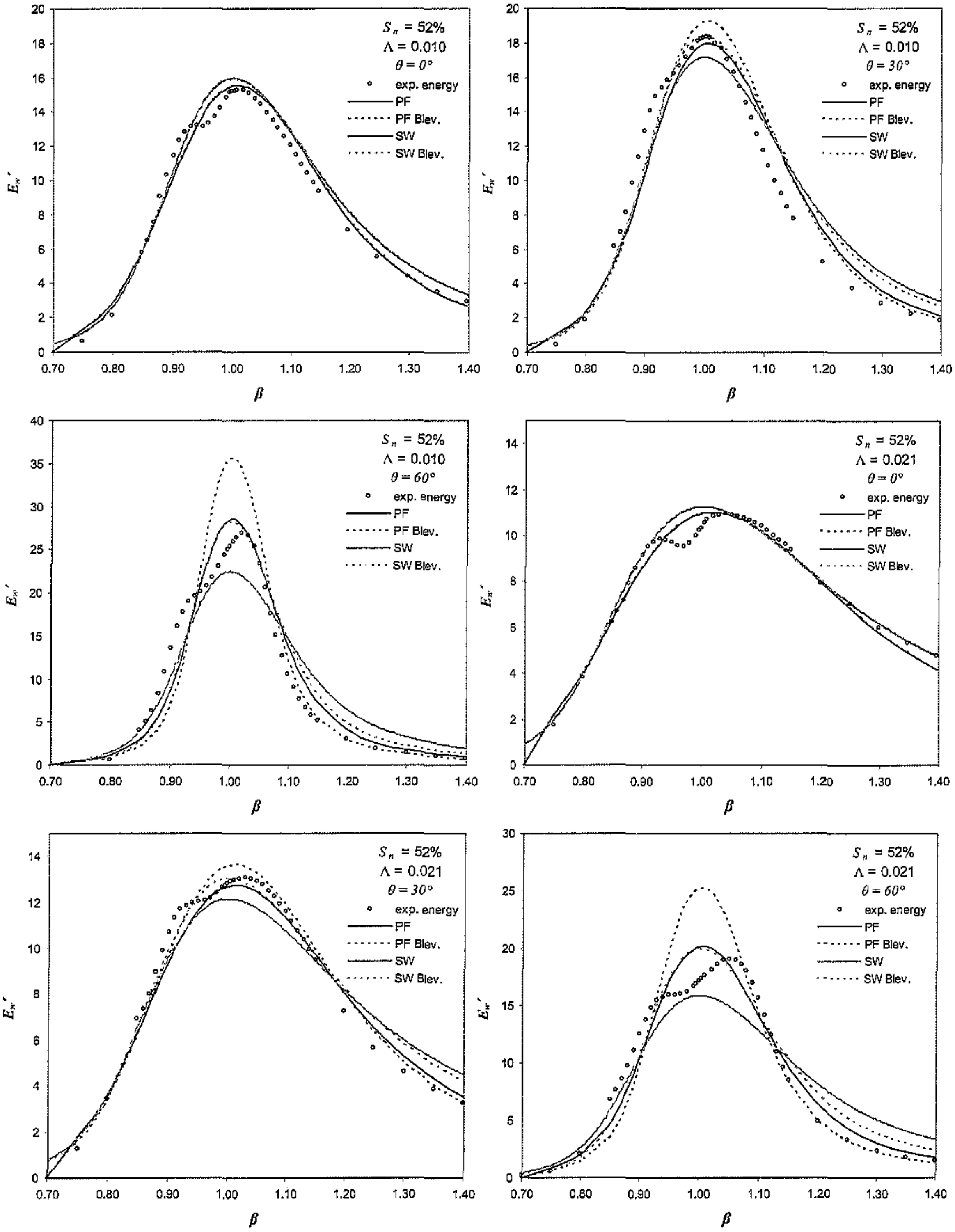

Figure 4.14 (continued).

First and foremost is the difference in results using $C_{\theta 2}$ and $C_{\theta 3}$ at different screen angles. For $\theta < 60°$, the frequency-responses for a particular model utilizing $C_{\theta 2}$ and $C_{\theta 3}$ are in reasonable agreement with one another, with the peak value of E_w' calculated using $C_{\theta 2}$ being higher overall between the two solidities. However, the significant influence of ψ/θ in $C_{\theta 3}$ is noticeable at the highest screen angle of $\theta = 60°$, resulting in a better estimated peak level of E_w' (for PF model).

The difference between the two models, PF and SW, is primarily due to the PF model more accurately capturing the influence of the screen losses over the height *and* length of the screen. The SW model, initially developed in this study (Cassolato and Tait 2005), is shown to contrast with the more complex PF model. Between both solidities the SW model tends to underestimate E_w' utilizing $C_{\theta 3}$, while better agreement is found by utilizing $C_{\theta 2}$, which produces results that appear to follow the PF model utilizing $C_{\theta 3}$. The SW model demonstrates that a change of value in the loss coefficient, C_θ, at the location (of the bottom) of the screens provides a simple technique to initially approximate the non-dimensional energy with changing screen angle.

Overall, Figure 4.13 and Figure 4.14 reveal the importance of selecting an appropriate solidity ratio, S, and for $C_{\theta 3}$, the deflection angle coefficient, ψ/θ. From the figures it is demonstrated that the higher values of ψ/θ are more suitable for $\theta = 60°$, which is in agreement with findings by Yeh and Shrestha (1989) after experimentally measuring slight variations in ψ with θ. From the comparisons, it is apparent that selecting suitable constant S and ψ values for a linear simulation of a non-linear device such as a TLD is challenging; however, the models presented in this study provide a good first approximation of the response of the TLD equipped with inclined slat-screens.

From this point forward, all simulations will utilize the loss coefficient developed in this thesis, $C_{\theta 3}$, with C_θ implicitly referring to this coefficient.

4.7.2 Time History Comparisons

The calculated responses of the fluid height, η', and base shear forces, F_w', from the SW and PF models are compared to the experimental results obtained in this subsection. The higher harmonics are removed from the experimental data using a digital low-pass filter to provide a suitable comparison to the linear models ability to predict the fundamental component of the response of the sloshing fluid. Figure 4.15 and Figure 4.16 are non-dimensional force-displacement, F_w'-Λ, energy loops for the 52% screens at amplitudes 5mm (Λ = 0.005) and 20mm (Λ = 0.021), respectively. Four frequencies are chosen, β = 0.95, 1.01, 1.07, and 1.15, at three screen angles, 0°, 30°, and 60°, to show the energy (loop area) and phase (loop trajectory) between the input excitation and the resultant base shear force at the lowest, middle, and highest screen angle. The horizontal x-axes are the normalized table motion, $\Lambda = A/L$, and the vertical y-axes are the normalized base shear forces, F_w' (Equation (3.4)). Similar results for the 42% screens are plotted in Figure 4.17 and Figure 4.18. Note that only Λ = 0.005 and 0.021 data was chosen to display for conciseness in comparing the models, one amplitude representing low (RMS/serviceability) amplitude range and another representing high (peak/ultimate) amplitude range.

Both models capture the response under low amplitude and low screen angle. They also capture the area of the loop and the trajectory—which represents the phase, φ, of the response—reasonably well up to 45°. Overall, the potential flow model captures the area of the loop more accurately as it accounts for the variation of velocity through the fluid depth. As expected at the highest angle, 60°, and high excitation amplitude ($\Lambda = 0.021$), the linear models are unable to accurately capture the area and trajectory of the loops due to the increased non-linear response at higher amplitudes. However, at $\beta = 1.15$ there is very good agreement especially between the potential flow model and the filtered experimental data, both in loop area and trajectory. The acceleration of the liquid mass becomes more prevalent at high β values and the accurate representation of the participating mass in the PF model is evident at $\beta = 1.15$ in the figures, compared to the SW model.

The time histories of the normalized free-surface motion, $\eta'(t)$, and the normalized base shear forces, $F_w'(t)$, are presented in Figure 4.19 and Figure 4.20 at $\beta = 1.01$ for the same amplitudes and screen angles presented in the previous four figures of force-displacement loops. Simulated and digitally filtered experimental results are shown. The free-surface motion is calculated at the wave probe locations shown in Figure 4.1. Both $\eta'(t)$ and $F_w'(t)$ are plotted over time normalized by the excitation period, T.

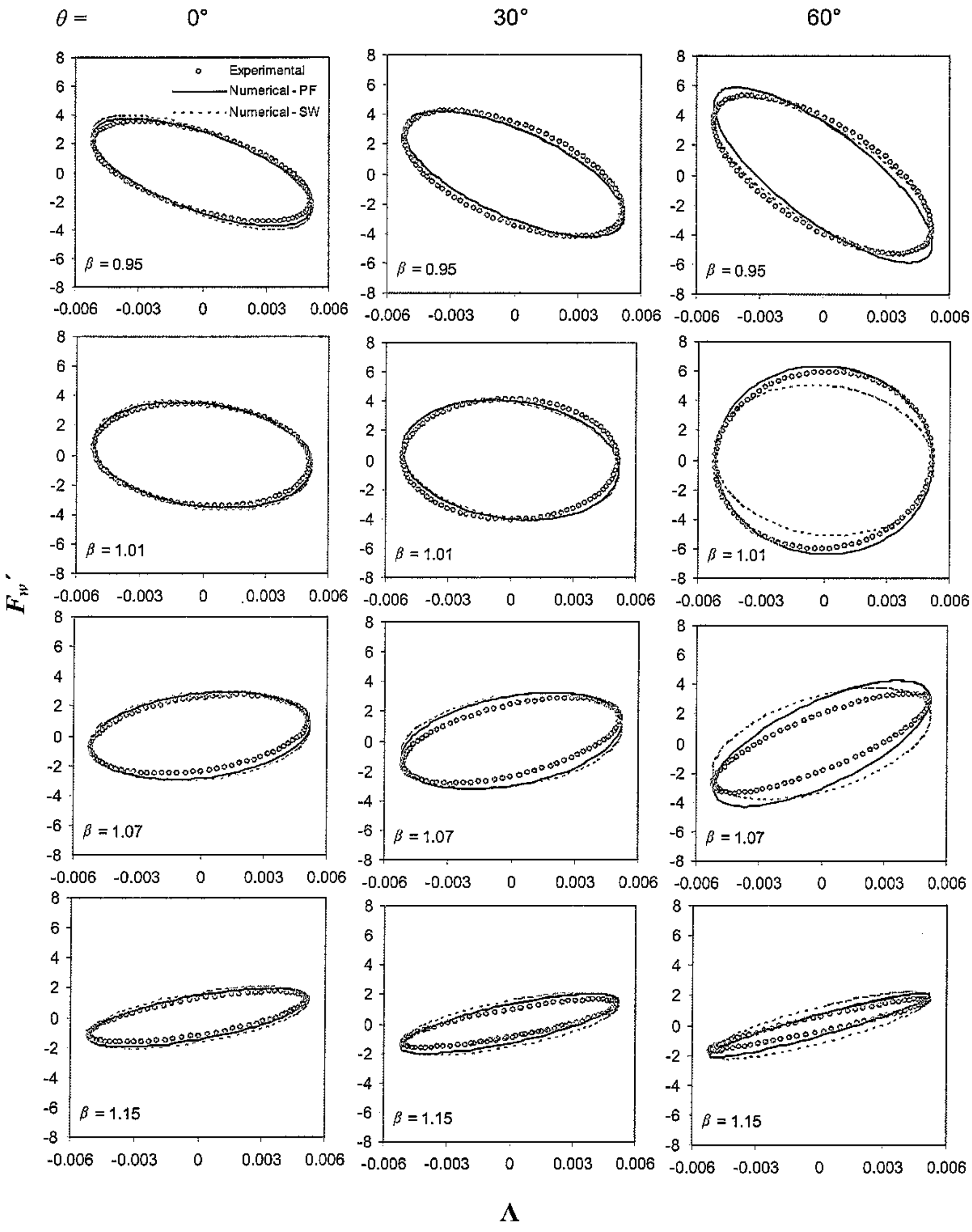

Figure 4.15. $S_n = 52\%$, $A = 5\text{mm}$, F_w'-Λ (ordinate-abscissa) energy loops at $\theta = 0°, 30°, \& \ 60°$.

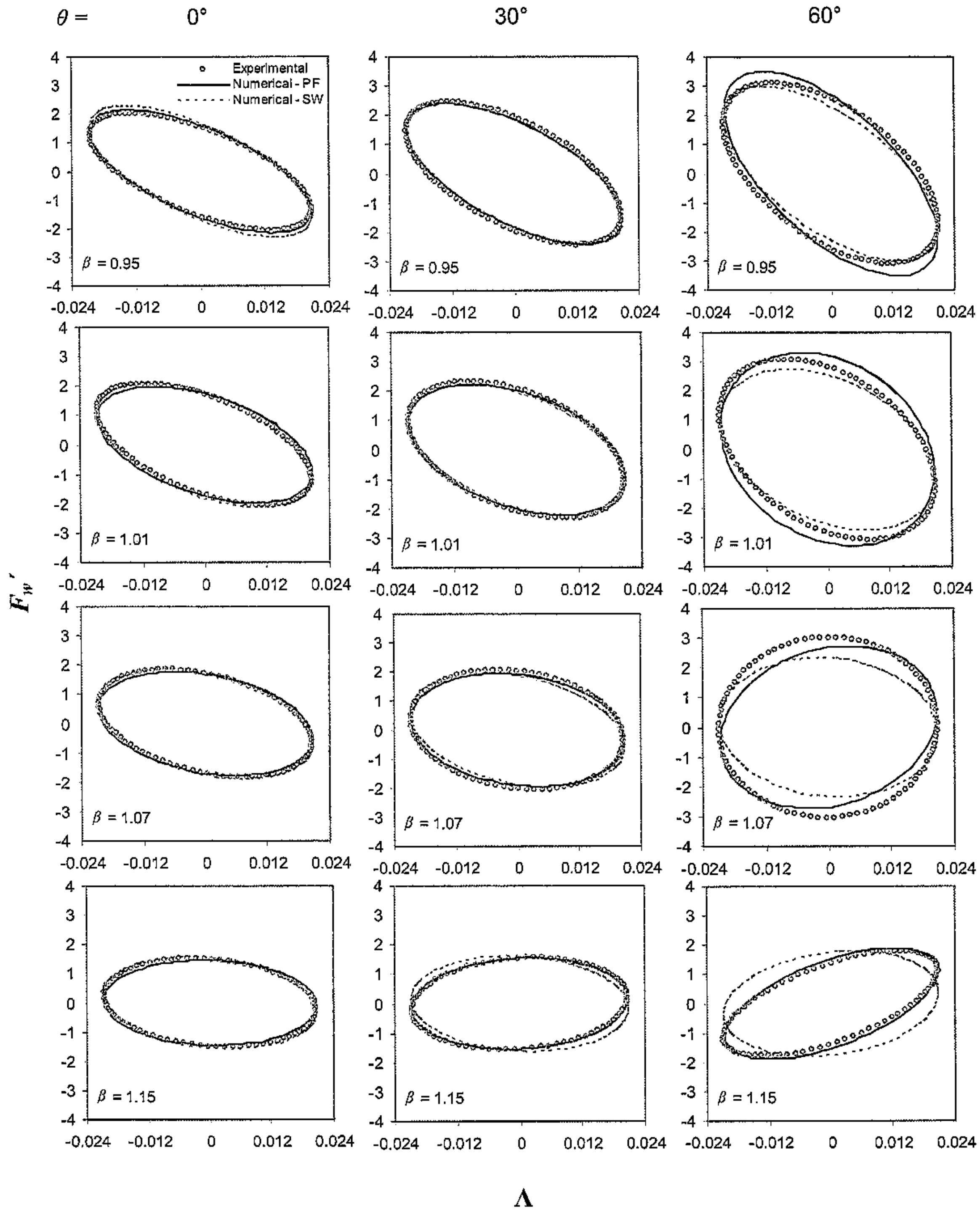

Figure 4.16. $S_n = 52\%$, $A = 20$mm, F_w'-Λ (ordinate-abscissa) energy loops at $\theta = 0°, 30°, \& 60°$.

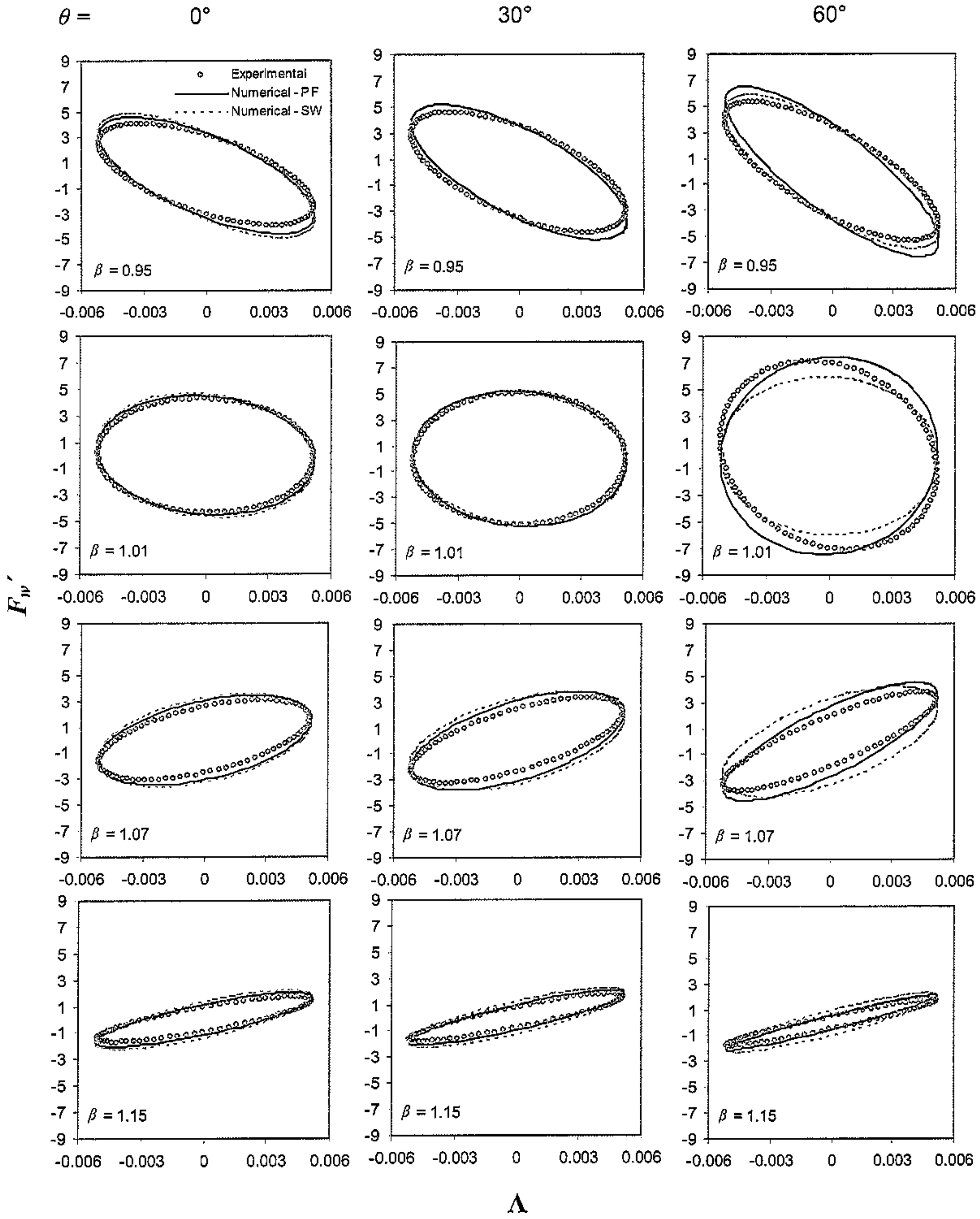

Figure 4.17. $S_n = 42\%$, $A = 5\text{mm}$, F_w'-Λ (ordinate-abscissa) energy loops at $\theta = 0°, 30°, \& \ 60°$.

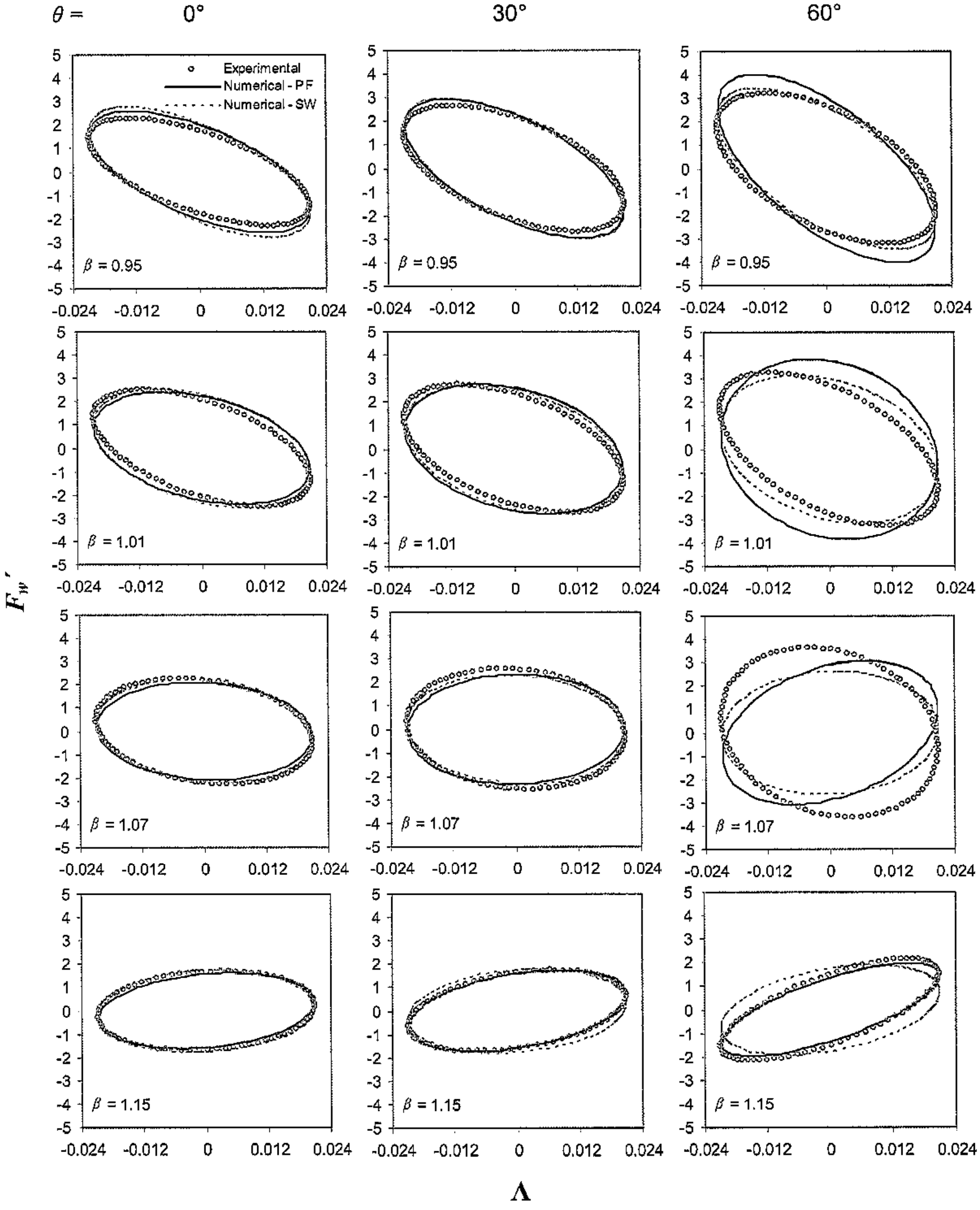

Figure 4.18. $S_n = 42\%$, $A = 20\text{mm}$, F_w'-Λ (ordinate-abscissa) energy loops at $\theta = 0°, 30°, \& 60°$.

Very good agreement is found between the fundamental test results and both linear models for $\Lambda = 0.005$ at both solidities at the 0° and 30° angles shown, for both wave height and base shear force time histories. Again, linear model calculations deviating from fundamental test results are found at $\theta = 60°$ and $\Lambda = 0.021$. It should be noted that although the simulated and fundamental free-surface response appear to be in good agreement, the linear models cannot accurately capture the actual response of the non-linear free-surface elevation (see Figure 3.17); however, as found with previous studies by Tait (2004) and Fediw (1992), the linear models do estimate the shear force quite accurately, within 10% at $\Lambda = 0.021$ at 0° and 30°. Therefore, in general, the resultant base shear forces can be modelled quite accurately for $\theta \leq 45°$ at lower excitation amplitudes.

Although the development of a non-linear simulation is beyond the scope of this study, the two linear models produced in this chapter can be used to predict with reasonable accuracy and quick efficiency the effect of symmetrically-angled horizontal-slat screens in a tuned liquid damper.

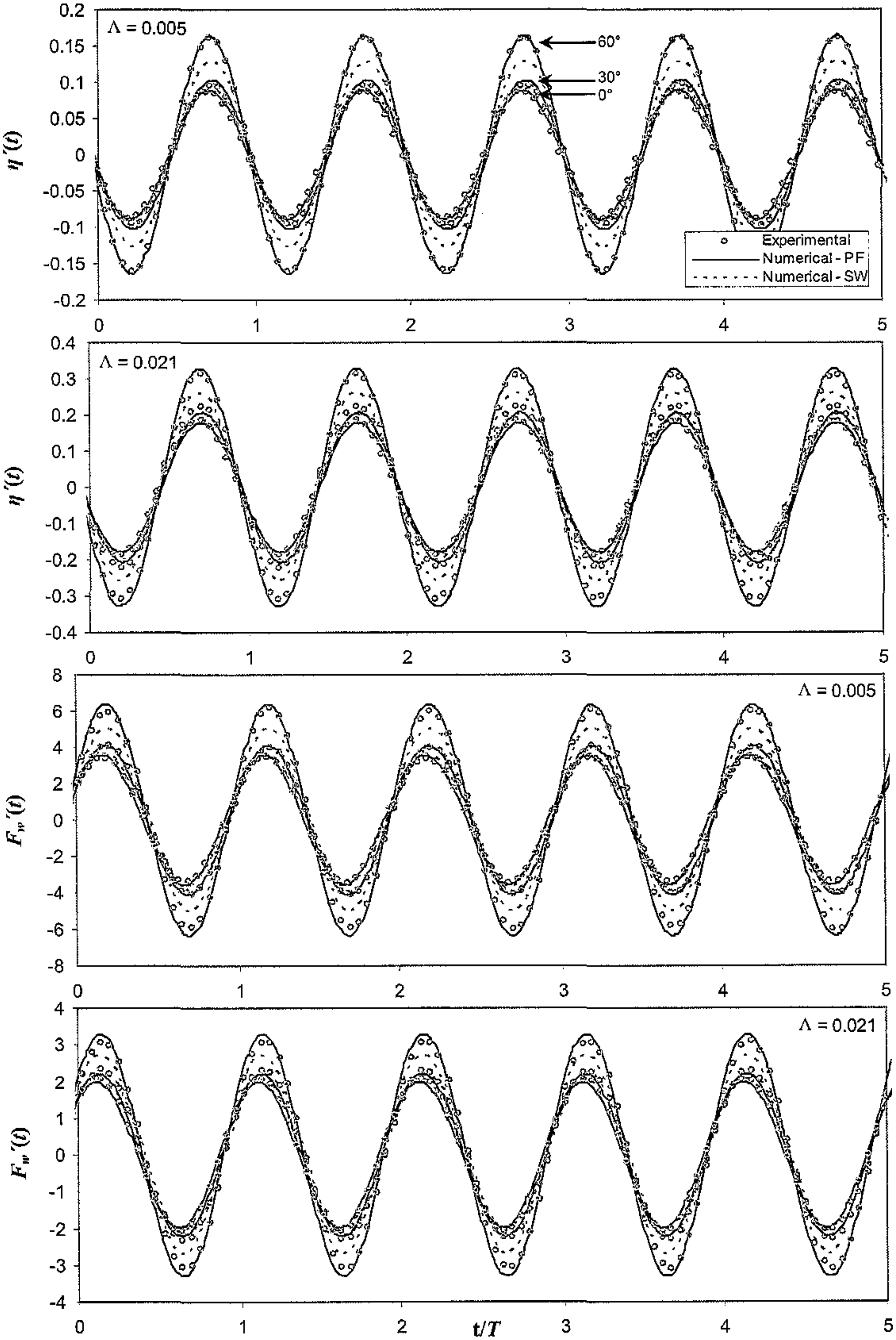

Figure 4.19. $S_n = 52\%$ Time histories of η' and F_w' for $\theta = 0°, 30°, \& \ 60°$ at $\beta = 1.01$.

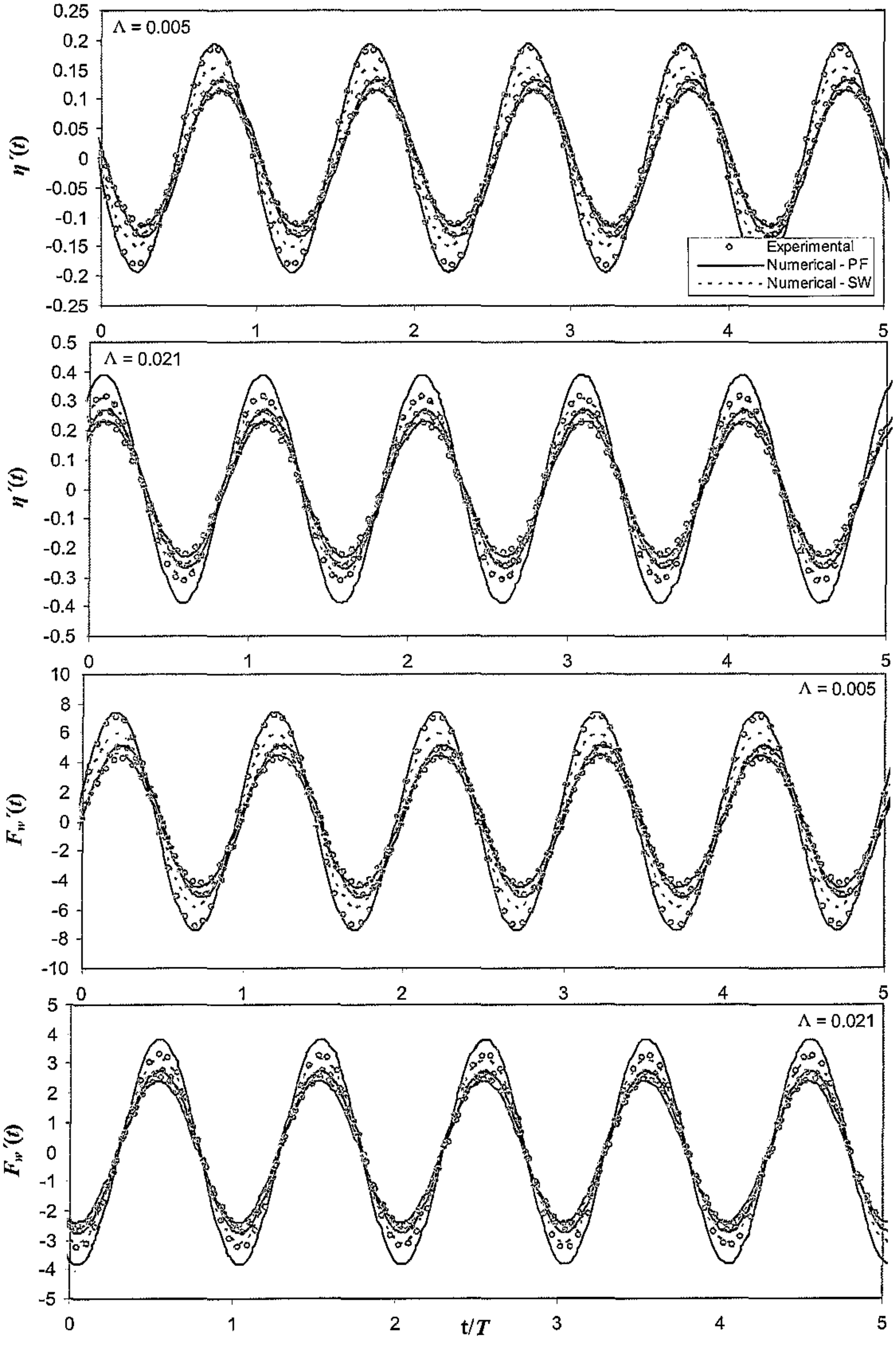

Figure 4.20. $S_n = 42\%$ Time histories of η' and F_w' for $\theta = 0°, 30°, \& \ 60°$ at $\beta = 1.01$.

4.8 Summary and Conclusions

This chapter has set out to compare the experimental results of symmetrically angled screens in a tuned liquid damper. The linear models utilize various pressure-loss coefficients, attempting to capture the overall effect of the change in energy dissipation with a change in screen angle. For the pressure-loss coefficient developed in this study, the loss coefficient formulated by Baines and Peterson (1951), $C_l(S)$, was extended to include the effect of the screen angle, $C_\theta(S,\theta)$, utilizing concepts of pressure-loss for an inclined screen from Yeh and Shrestha (1989). Two models, one based on shallow water wave theory, another based on potential flow theory, were presented. The following conclusions are summarized:

- Equation (4.13), which is equal to the formulation of the established use of the pressure-loss coefficient for a vertical screen ($\theta = 0°$) by Baines and Peterson (1951), allows straightforward implementation of the loss of angled screens
- All theoretical results are valid for $0.40 \leq S \leq 0.60$ and $\theta \leq 60°$, which are the practical values used in experimentation as well, assuming that the fluid losses are independent of the flow direction (§3.9)
- The two linear numerical models developed in this study provide a suitable and efficient way for predicting the energy dissipation, E_w', of a

TLD equipped with angled screens due to the dominance of the fundamental response (§4.7)

- The more rigorous potential flow model is found to accurately predict the TLD response in the RMS excitation amplitude range ($\Lambda < 0.016$)
- The simulated response depends on screen solidity, S, and deflection angle, $\psi(\theta)$. For the value of $\psi/\theta = 0.80$ selected for $\theta \leq 45°$, $\psi/\theta = 0.90$ at $\theta = 60°$ for $S_n = 42\%$, and $\psi/\theta = 0.85$ at $\theta = 60°$ for $S_n = 52\%$, the potential flow model, in particular, accurately predicts the TLD response at low excitation amplitudes for screen angles $\theta \leq 45°$ and for screen angles $\theta > 45°$ when using the suggested ψ/θ values
- Findings from this chapter show that the potential flow model utilizing the pressure-loss coefficient developed, $C_{\theta 3}$, can be used to provide initial estimates of screen forces, the base shear forces, F_w', and corresponding energy dissipated, E_w', for preliminary design purposes

CHAPTER 5: EXPERIMENTAL PERFORMANCE OF OSCILLATING SLAT-SCREENS IN A TUNED LIQUID DAMPER

5.1 Introduction

The performance of a TLD for a given mass ratio, μ, is a function of the tuning ratio, α, and the inherent TLD damping ratio, ζ_a. The damping ratio of a TLD equipped with fixed vertical damping screens is related to the screen pressure-loss coefficient, C_l (C_{0°), and the square of the fluid velocity at the screen location. Therefore, the equivalent linear viscous damping ratio that develops due to the screens is amplitude-dependent. As a result, a TLD equipped with screens may only operate optimally for single excitation amplitude, unless the screen angle is adjusted.

The ability to passively control ζ_a over a range of amplitudes was first proposed theoretically in Cassolato and Tait (2005). Modifying ζ_a by adjusting the screen angle, which alters the screen loss coefficient, was experimentally investigated in Chapter 3 for discrete symmetric fixed-angles, θ. Results from Chapter 3 indicate that rotating the screens to adjust C_θ is a plausible method to maintain a constant level of ζ_a over a range of excitation amplitudes.

The screen configuration employed in Chapter 3 was unable to automatically adjust the screen angle. This chapter focuses on the performance of a TLD equipped with oscillating sharp-edged slat-screens. These screens are termed, *smart screens*, as they can self adjust; i.e., they require no external input to alter their damping characteristics over a range of excitation amplitudes.

5.2 Slat-Screens Motion

To achieve the desired effects, the screens were hinged at the bottom of the floating frames. This set-up was designed to allow the screens to oscillate freely about their initial vertical position, 0°. The screen configuration employed in this chapter is shown in Figure 5.1. As described in Chapter 2, the linked-parallel motion was deemed to be the most feasible solution to have the screens oscillate together, freely with the sloshing fluid.

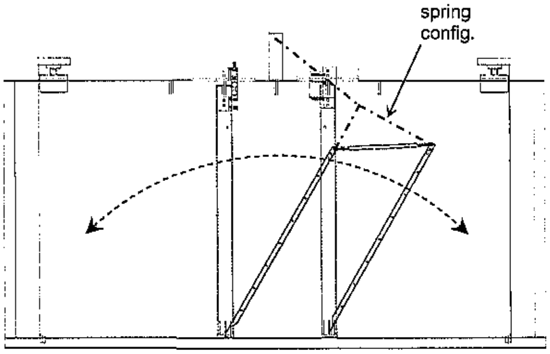

Figure 5.1. Schematic of parallel screen motion.

A three-spring configuration was selected connected in a “Y” formation with the angle between each spring initially set at ~120° (vertical position, 0°). This arrangement permitted reasonable screen motion at all amplitudes and provided enough restoring force so that the screens would return to their vertical position when fluid motion ceased, see Figure 5.1. The restoring force in the springs is a function of the fluid drag force onto the screens, the height of the link above the screen hinges (that the springs are connected to), screen angle, and the weight of the screens. Considering these factors and the springs available, the height of the link was moved from the top of the screens to a lower connection between the vertical stiffeners. Approximately a 140mm span of slats from each set of screens was removed to reduce the screen mass. All fluid still passed through the screens at the highest angle, $\theta = 60°$. The springs were selected to provide sufficient motion at small amplitudes with an adequate restoring force. The individual nominal spring stiffness quoted from the manufacturer was 0.100lbf/in (17.5N/m). Figure 5.2 displays photographs from moving screen experiments conducted at both small (left photo) and large (right photo) excitation amplitudes. The spring configuration discussed above can be clearly seen.

Figure 5.2. Screens oscillating passively under sloshing fluid.

An additional benefit of removing the top portion of slats from the screens was that the screens oscillated without making contact with the wave probes. The stainless steel hinges were coated with vacuum grease, resulting in negligible friction/resistance in the hinges.

The screen angle, θ, for a particular screen was measured as before from the vertical position; however, the screens were now parallel to each other. The highest angle, θ, attained under 5mm excitation amplitude was approximately 30° for the 52% screens and approximately 15° for the 42% screens. The difference in screen angle between the two screens tested can be attributed to their respective solidities where the 52% screens had more screen area resulting in higher drag forces onto the screens.

Owing to a significant increase in the non-linear response of the sloshing fluid through this configuration of oscillating (moving) screens, the highest excitation amplitude tested was A = 20mm (Λ = 0.021). Above a 20mm amplitude of table excitation water began exiting the tank. Also, it was observed at this excitation amplitude that the screens rotated to a maximum angle, $\theta \approx 60°$, similar to the largest angle tested in Chapter 3.

5.3 TLD Frequency-Response with Oscillating Screens

This section examines the energy dissipation frequency-response of the experimental results. The frequency-response curves are plotted as non-dimensional energy, E_w', versus non-dimensional excitation frequency, β. Figure 5.3 displays the β-E_w' results for the moving screen tests conducted at a water depth of h = 119mm (h/L = 0.123) for both sets of screens.

It is evident from Figure 5.3 that increased non-linear hardening behaviour is found for the moving screens configuration as opposed to the symmetric fixed-angle screens configuration studied previously in Chapters 3 and 4.

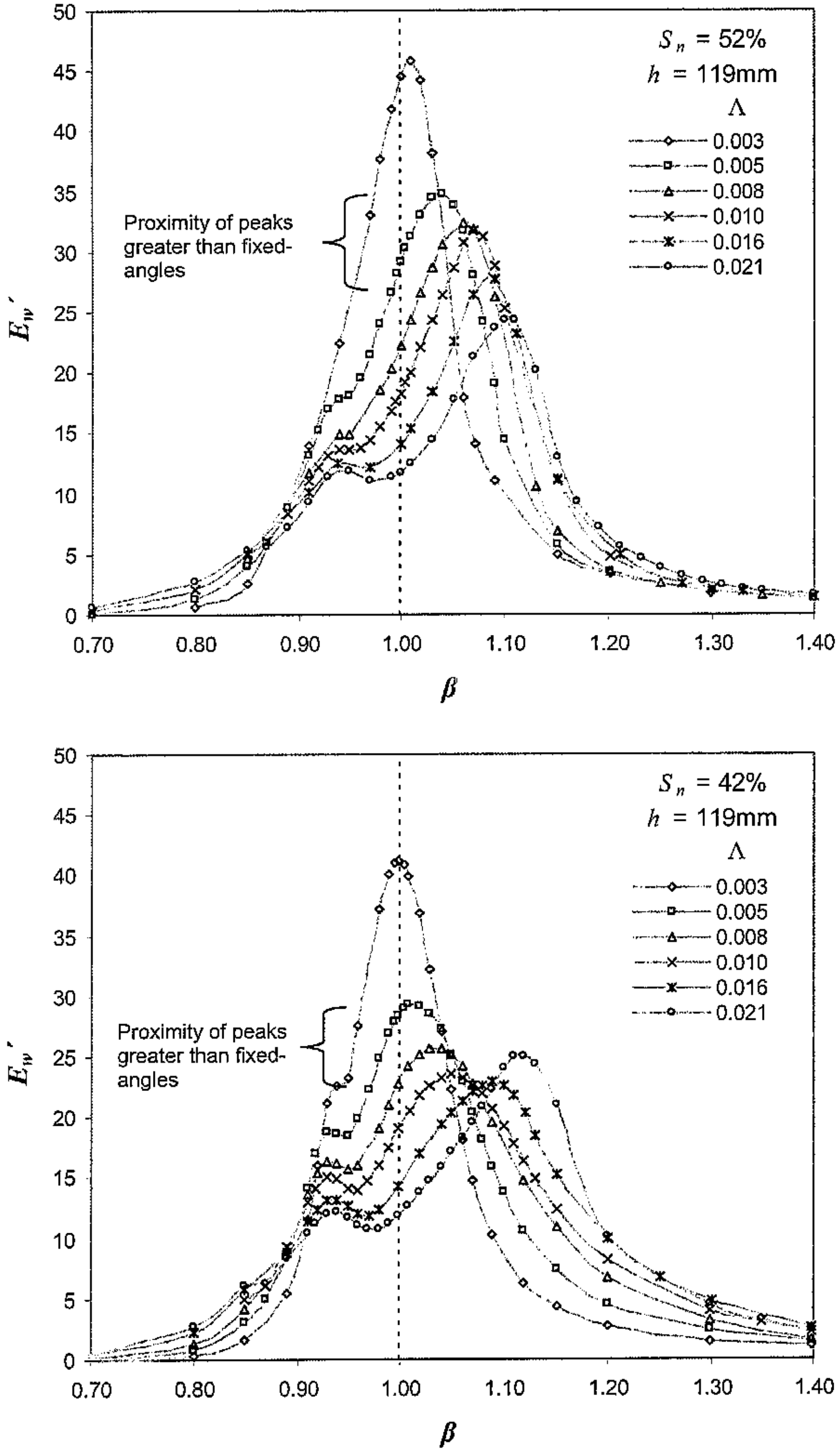

Figure 5.3. Frequency-Response curves for screens in motion (oscillating).

The shift in peak frequency (resonant frequency for E_w') is found to be twice as large for the oscillating screen configuration than for the symmetrically fixed-angle screens at $\Lambda = 0.021$ at both screen solidities (contrast Figure 5.3 with $\theta = 0°$ in Figure 3.13 and Figure 3.14, accordingly).

In addition to the discussion in the previous section (§5.2) regarding the extent of motion between the solidities, the higher movement of the 52% screens results in a more rapidly increasing peak frequency shift at lower excitation amplitudes than observed for the 42% screens. For $S_n = 42\%$ an unexpected trend in the normalized energy dissipation with excitation amplitude is found to occur at the highest $\Lambda = 0.021$. Furthermore, depending how the screen motion responds to fluid motion with the particular spring configuration used, the peak E_w' at $\Lambda = 0.021$ is found to be higher than otherwise expected by the trend over the excitation amplitudes investigated.

From Figure 5.3 it can be seen that the frequency-response peaks across a range of amplitudes, particularly from $\Lambda = 0.008$ to 0.021 in the 42% curve set maintain a more constant value than that of the fixed-angle screens. Although an ideal constant peak value across any range of amplitudes was not achieved, due to the use of a linear spring, it is interesting to find that despite the shifting peak frequency value the closeness of the peaks suggest that the moving screen configuration yields a more invariable damping behaviour over a range of excitation amplitudes; opposed to that found when examining Figure 3.13 or Figure 3.14 for a constant θ. This finding indicates that a near-constant level of

TLD damping, ζ_a, is achievable for these screens. This observed behaviour is similar to the theoretical behaviour of a TLD equipped with symmetric screens, which would maintain a near-constant level of target optimal damping, $\zeta_{a\text{-}opt}$, in a structure-TLD system over a range of excitation amplitudes.

This improved invariable damping behaviour over a range of excitation amplitudes is similar to that observed in Figure 3.21 for different fixed-angles over a large range of excitation amplitudes. The close proximity of the peaks found in the moving screen experiments shows that the implementation of smart screens to linearize damping is plausible.

5.3.1 Frequency Shifting with Change in Water Height, *h*

To investigate frequency hardening with this screen configuration, the water depth, h, is varied to achieve a peak frequency ratio of $\beta = 1.00$ at a desired excitation amplitude. Theoretically, h alone can adjust the natural sloshing frequency (Equation (4.39) with $n = 1$ and $f_n = \omega_n / 2\pi$),

$$f_n = \frac{1}{2\pi}\sqrt{\frac{\pi g}{L}\tanh\frac{\pi h}{L}} \tag{5.1}$$

Since Equation (5.1) is the theoretical *linear* natural sloshing frequency, this adjustment is valid only for small free-surface response amplitudes (approximately $\Lambda \leq 0.010$). For this study here, the 52% screen set was chosen with the frequency-response plotted in Figure 5.4.

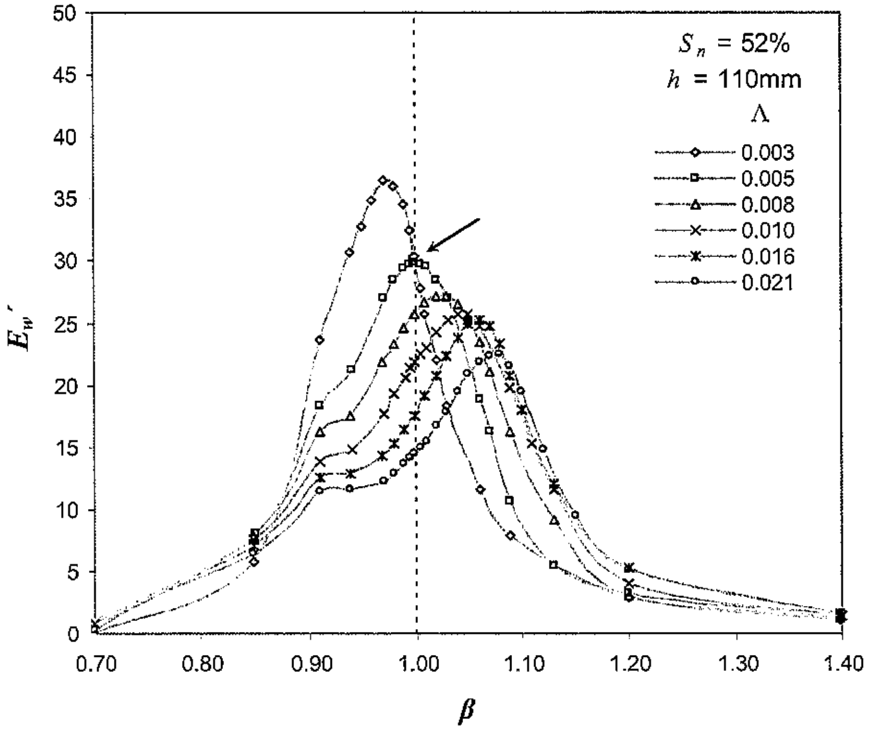

Figure 5.4. Frequency-Response for 52% screens in motion with h = 110mm.

To demonstrate adjustment of the peak frequency (tuning of TLD), a frequency shift methodology was devised with the 5mm (Λ = 0.005) amplitude selected as the target peak to shift back to β = 1.00. The peak frequency of Λ = 0.005 in Figure 5.3 for the 52% screens is 0.568Hz (or $\beta \approx$ 1.04). The target peak frequency is determined by taking the percent difference between $\beta \approx$ 1.04 and the peak frequency of the 0° curve ($\beta \approx$ 1.00, see Figure 3.14) and decreasing the 0° peak frequency by this percent difference. Solving for the corresponding h in Equation (5.1) at this reduced frequency yields the water depth at which the shifted peak frequency upon screen rotation should yield the desired f_n = 0.546Hz (β = 1.00) for the oscillating configuration. Such is the case shown in Figure 5.4

(emphasized by arrow) with experimental results based on a water height of h = 110mm (h/L = 0.114) determined by the aforementioned procedure.

Increased proximity of the peak E_w' values is also present in Figure 5.4, supporting the intended behaviour of smart screens, which are in fact closer than that shown in Figure 5.3 (52% screens) at a water depth of h = 119mm.

5.3.2 Comparison Between Oscillating and Fixed-Angle Screens

This subsection compares the frequency-response curves for fixed-angle and oscillating screens tests, firstly between vertical and oscillating screens, including the effect on the shift in peak (response) frequency as discussed in the

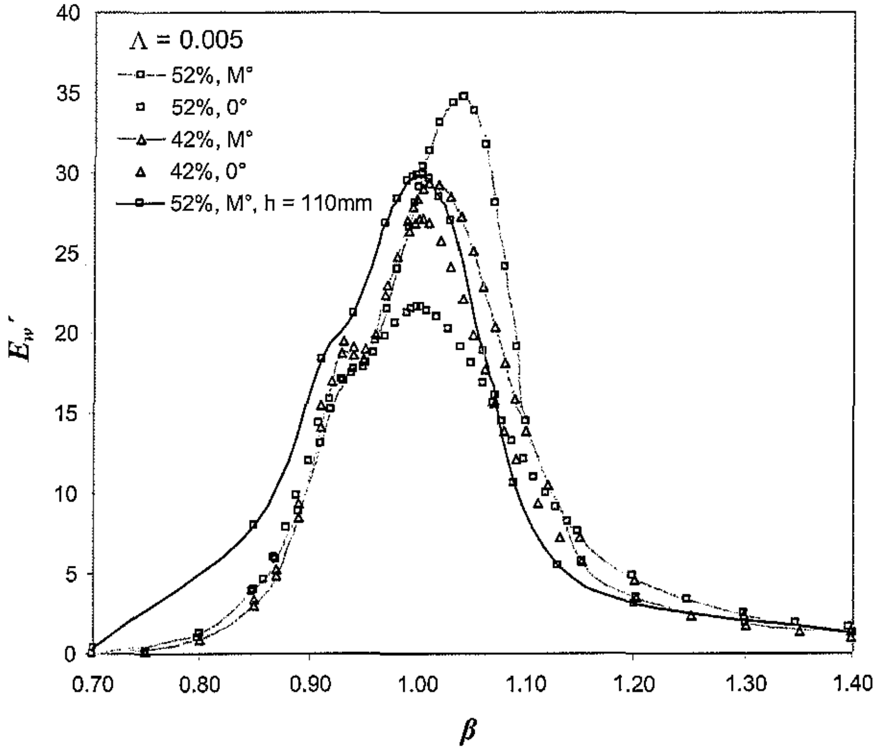

Figure 5.5. β-E_w' comparison between moving (“M°”) and 0° experiments.

previous subsection. Since the frequency shifting test was conducted based on the shift of the 5mm response curve, initial comparisons are made for the $\Lambda = 0.005$ case.

Figure 5.5 displays the experimental frequency-response curves for both screen solidities between the vertical (0°) and moving screens ("M°") and includes the result for h = 110mm for the 52% screens. Note the peak $E_w{}'$ values for 52%-M° at h = 110mm are greater compared to that of 42%-0°. This behaviour is similar to the comparison made in §3.7. This again demonstrates that, in general, rotated screens (or rotating in this case) can exhibit similar damping characteristics as another regular vertical screen(s) with differing S_n.

The fixed-angle screens frequency-response curves from Figure 3.21(a) are presented again in Figure 5.6 for the same excitation amplitudes as the reduced h curves of the oscillating screen tests from Figure 5.4. Figure 5.6 highlights the near-constant damping concept by comparing the results from both the fixed-angle and oscillating screen tests. Although the oscillating screens test results at h = 110mm do not match the level of $E_w{}'$ for the fixed-angle results; for the linear spring configuration utilized, the reduced water height brings the peaks of the oscillating results closer to the fixed-angle curves.

The regular vertical screens ($\theta = 0°$) β-$E_w{}'$ curves for the 42% solidity are also plotted in Figure 5.6 at excitation amplitudes $\Lambda = 0.005$ and 0.008. These two particular β-$E_w{}'$ curves were selected as their peak $E_w{}'$ values are similar to the range of peak $E_w{}'$ values for each group of the 52% test results.

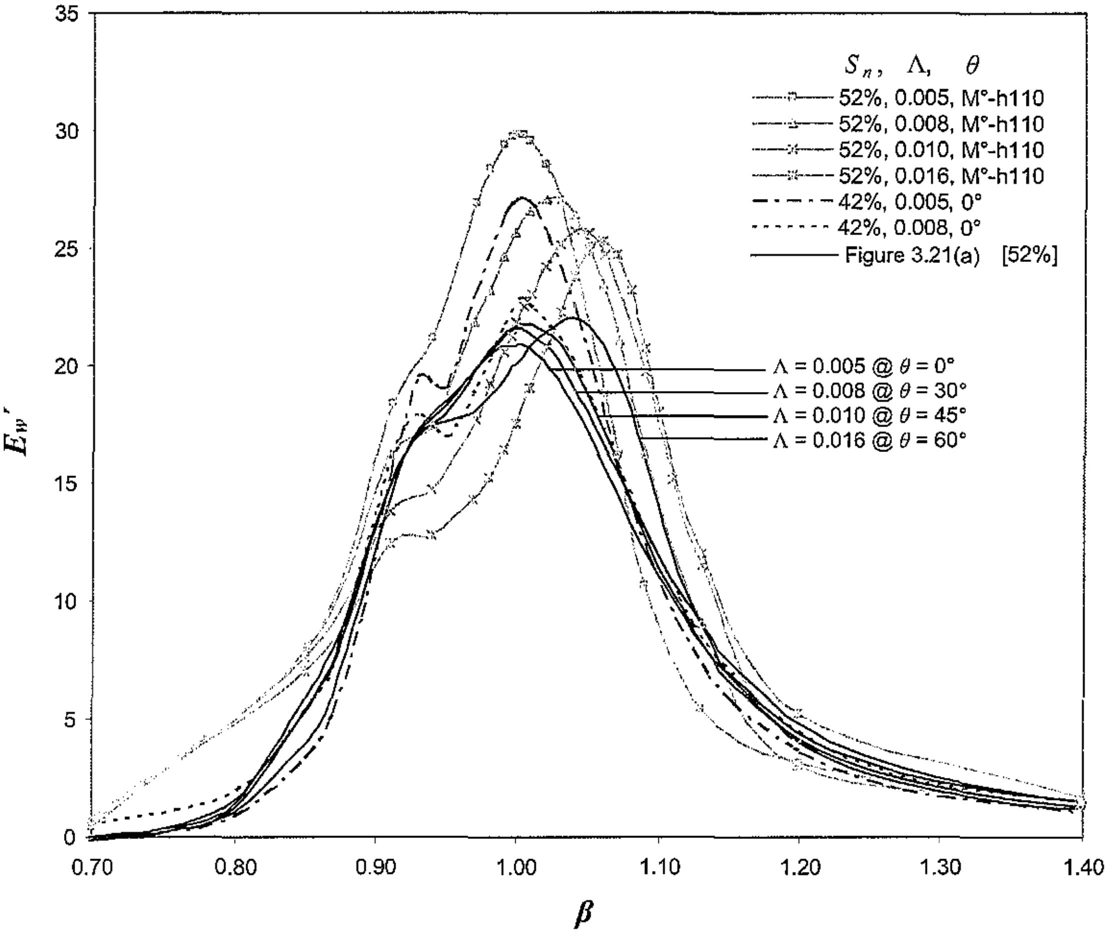

Figure 5.6. Comparison of moving and fixed-angle frequency-response, β-E_w'.

The fixed-angle 52% results (from Figure 3.21(a)) have a level of damping close to that of the 42%-0° results at $\Lambda = 0.008$, whereas the moving 52% results have a level of damping around the 42%-0° results at $\Lambda = 0.005$. Both comparisons highlight the proposed invariable-damping-over-amplitude performance of smart screens, in this case for symmetrically-angled and parallel-oscillating slat-screens, respectively.

5.4 Force-Displacement Hysteresis

This section presents the experimental force-displacement hysteresis loops for the two sets of screens tested. Comparisons are made with the fixed-angle responses. On the other hand, no theoretical simulations for moving screens are presented for comparison purposes as this is beyond the scope of this study. Only the results of the regular water depth primarily used throughout this study, h = 119mm, is examined.

Figure 5.7 and Figure 5.8 are the non-dimensional force-displacement hysteresis loops from the experiments of the 52% oscillating screens and the 42% oscillating screens, respectively. The y-axes are F_w' and the x-axes are Λ. The loops are separated by columns of three different excitation amplitudes, 0.005, 0.010, and 0.021, and are plotted at four frequency ratios of β = 0.95, 1.01, 1.07, 1.15, which are recurring amplitudes and frequencies. The plotted hysteresis loops include the digitally filtered experimental results, as described in previous chapters, to show the energy dissipation due to the fundamental sloshing mode ("FILT. EXP." in legend, Figure 5.7).

Noticeable in the measured data are the influence of higher harmonics indicated by the waviness in the loops. The same contrast can be seen between Figure 3.19 and Figure 4.16, for example. However, careful examination of the difference in energy (area) of each hysteresis loop between the measured and digitally filtered data suggests that nearly all the energy is attributed to the fundamental mode of response (Reed et al. 1998, Tait 2004).

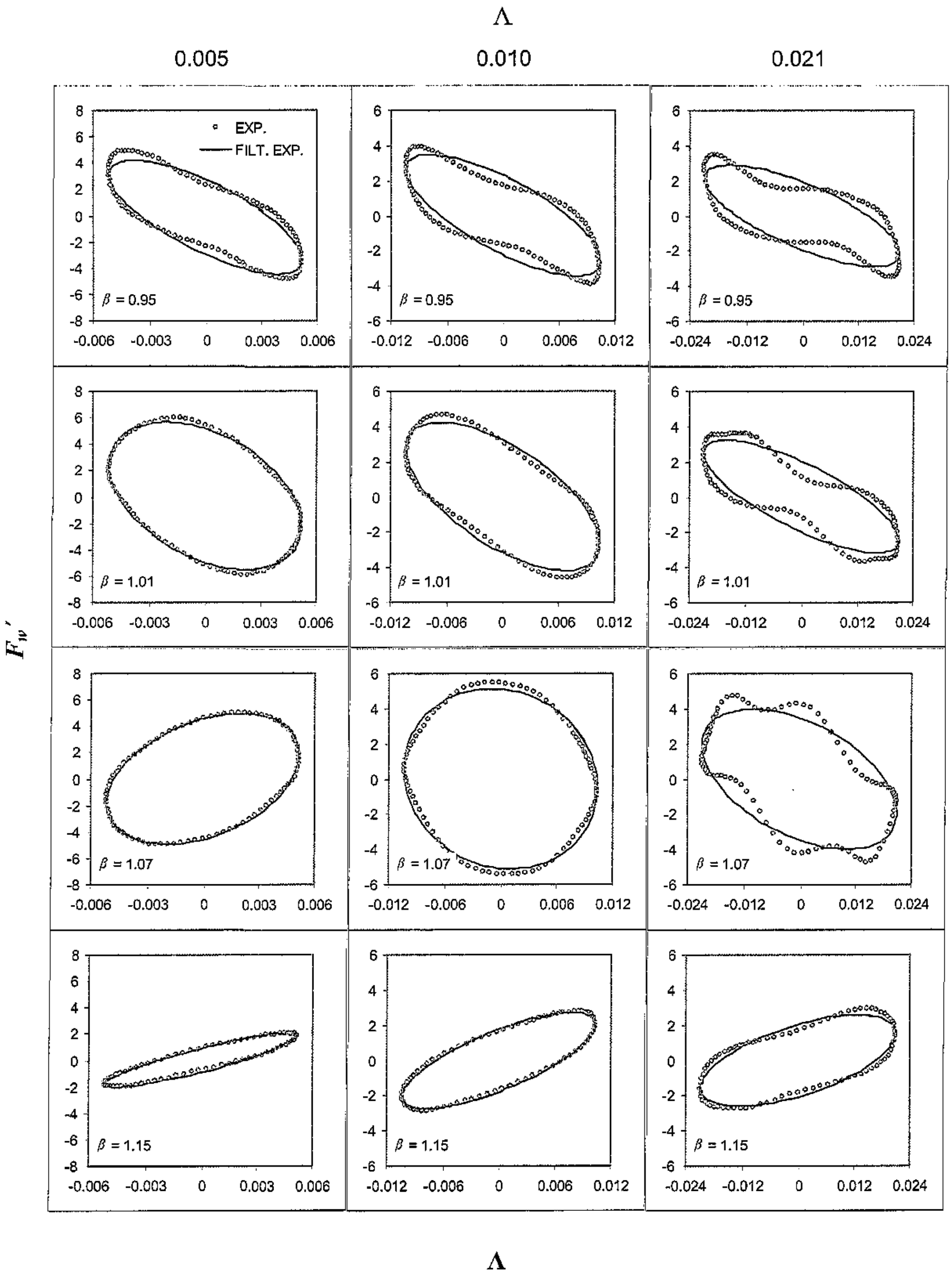

Figure 5.7. F_w'-Λ (ordinate-abscissa) hysteresis loops for 52% oscillating screens.

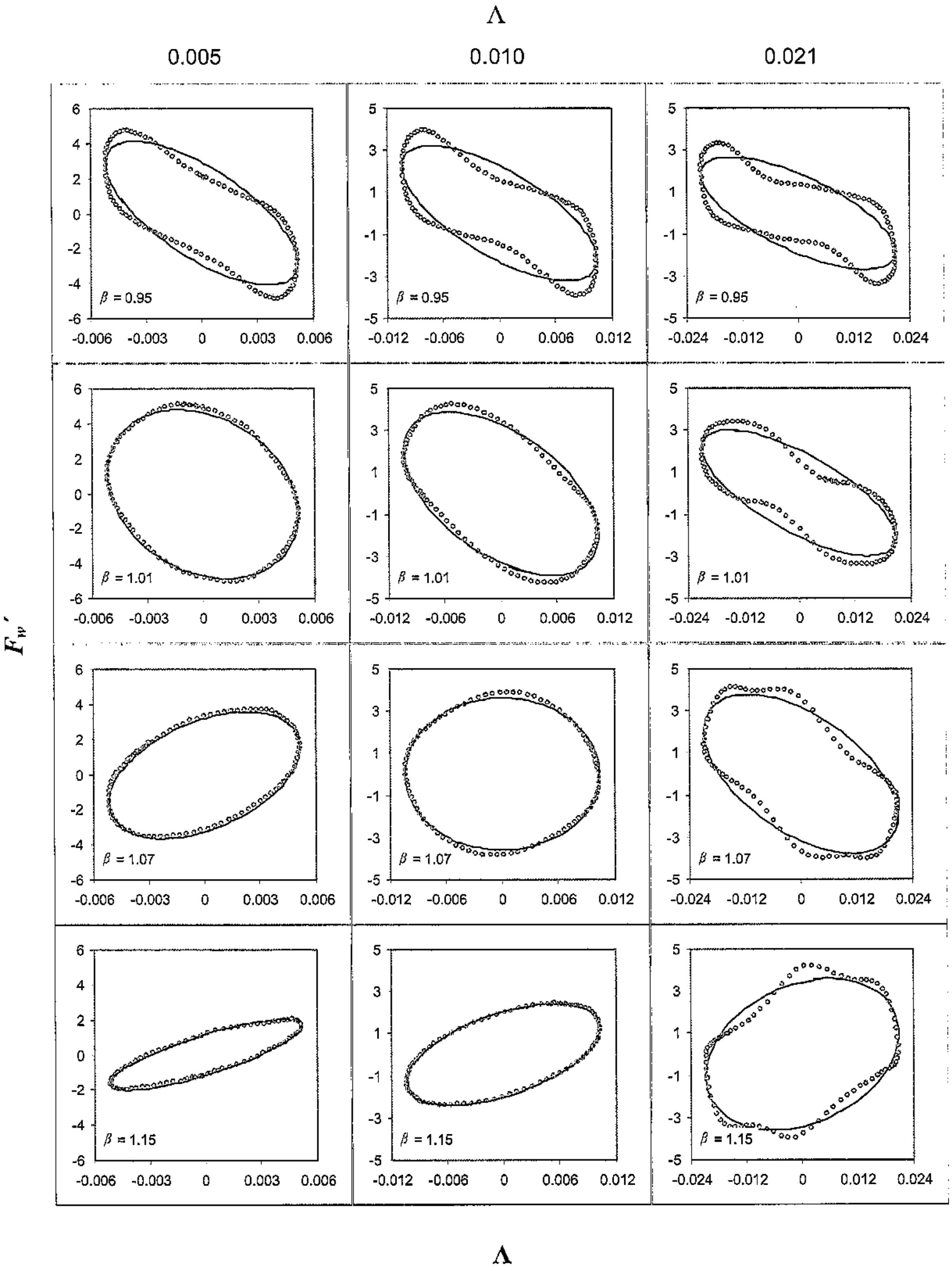

Figure 5.8. F_w′-Λ (ordinate-abscissa) hysteresis loops for 42% oscillating screens.

Unlike the difference in energy dissipation (loop area) between $\Lambda = 0.010$ at $\beta = 1.07$ and $\Lambda = 0.021$ at $\beta = 1.15$ for the 52% screens, note the more comparable loop area for the 42% screens in Figure 5.8. This indicates the increase in peak E_w' at 0.021 in Figure 5.3 for the 42% screens.

5.4.1 Hysteresis Comparison with Fixed-Angle Screens

In this section, the experimental hysteresis loops presented in the previous two figures are plotted with the fixed-angle loops for comparison. Essentially, Figure 5.9 is an amalgamation of Figure 3.19 and Figure 3.20 with Figure 5.7 and Figure 5.8 (respectively) for two frequency ratios ($\beta = 1.01$ and 1.07).

From Figure 5.9 the following observations are made. At higher (normalized) excitation amplitudes, Λ, a significant difference between the oscillating screens hysteresis loops and fixed-angle screens hysteresis loops is observed. This is particularly evident at $\Lambda = 0.021$ where higher harmonics are clearly visible for the oscillating screens case. The moving screens hysteresis loops for the 42% screens case are found to be in reasonable agreement for the $\theta = 60°$ test case. In addition to the presence of higher harmonics for the 52% screens, a noticeable change in loop trajectory is observed, which is a result of hardening (Figure 5.3). Comparing the TLD response behaviour for fixed-angle and oscillating screens cases (Figure 5.9), it can be seen that greater changes were found to occur in the hysteresis loops for the screens with higher solidity, $S_n = 52\%$.

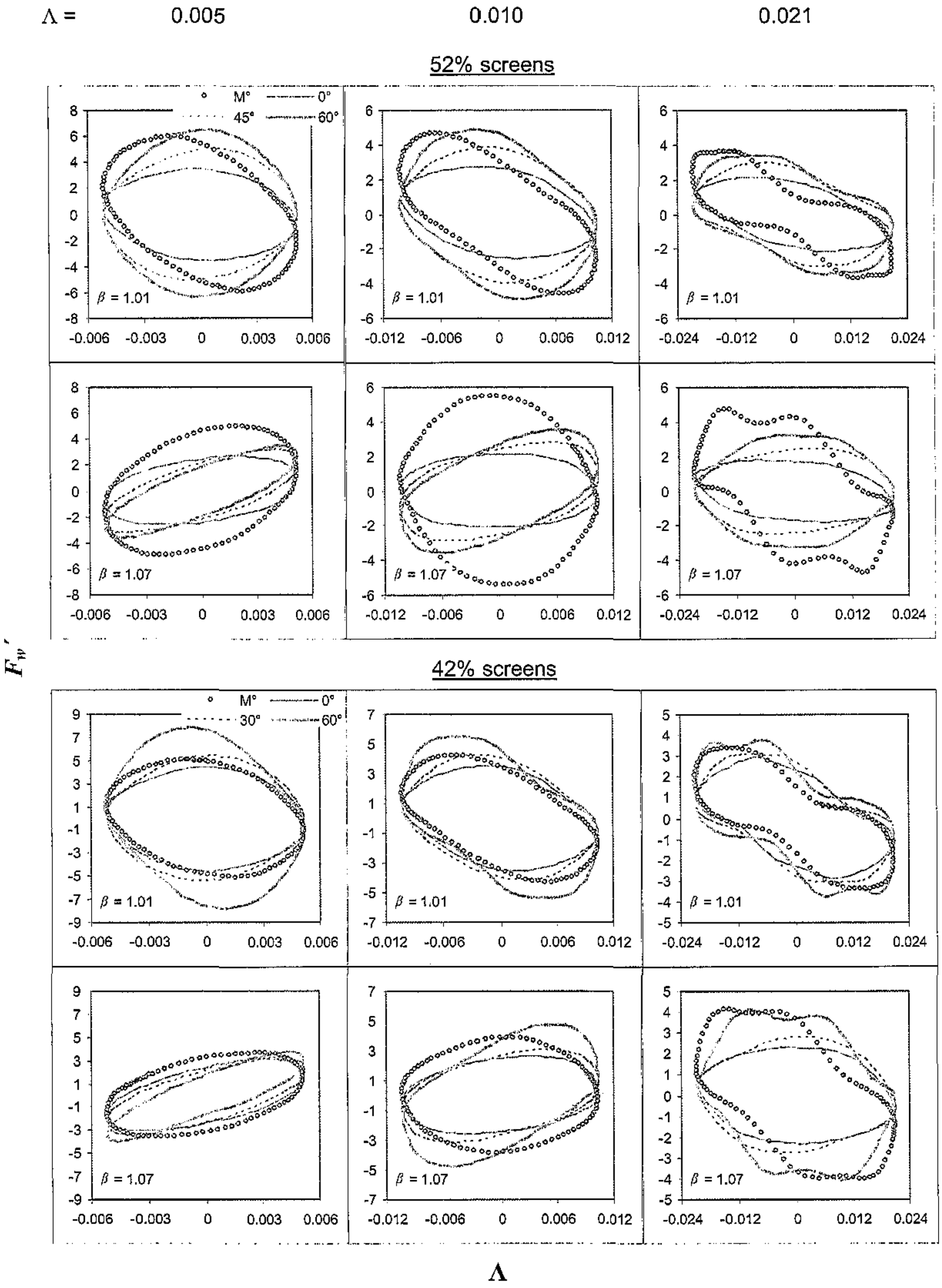

Figure 5.9. Experimental E_w' loops from oscillating ("M°") and fixed-angle, θ (°), tests. (ordinate: F_w'; abscissa: Λ)

5.5 Time Histories

The following two figures are normalized time histories of experimental base shear forces, Figure 5.10, and experimental free-surface response, Figure 5.11, at a frequency ratio, $\beta = 1.01$. $F_w'(t)$ and $\eta'(t)$ for various fixed-angle tests are also plotted in the figure for comparison.

The extent of screen motion between the two solidities discussed earlier in §5.2 can be seen in the following two figures, both in $F_w'(t)$ and $\eta'(t)$. Since there was greater screen motion for the more solid 52% screens, the base shear forces and the free-surface motion tend to reflect the response level of the 45°-60° fixed-angles, whereas the 42% screens match the response level of their 15°-30° fixed-angle counterparts. In addition, at the largest amplitude tested, $\Lambda = 0.021$, the 52% screens F_w' and η' amplitudes both exceeded the 60° response level, whereas the 42% screens are less than its respective fixed-angle response levels.

It should be noted that the velocity-squared damping seen earlier in the fixed-angle screen forces (§3.9) is also visible in the time domain of the base shear forces in Figure 5.10 but only at the higher excitation amplitudes (in this case, $\Lambda = 0.021$ shown in the figure).

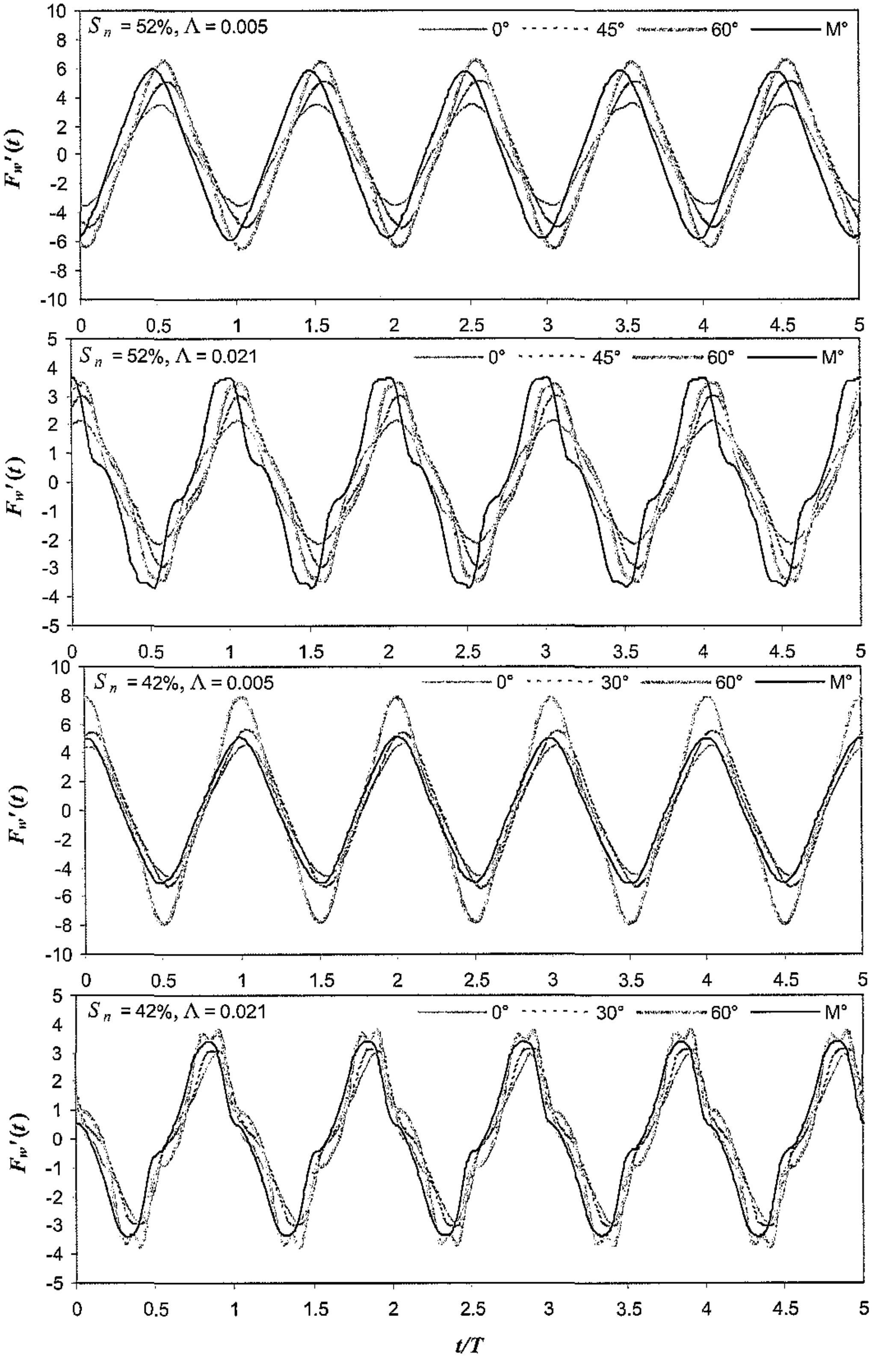

Figure 5.10. Base shear forces, $F_w'(t)$, for moving and various fixed-angle tests @ $\beta = 1.01$.

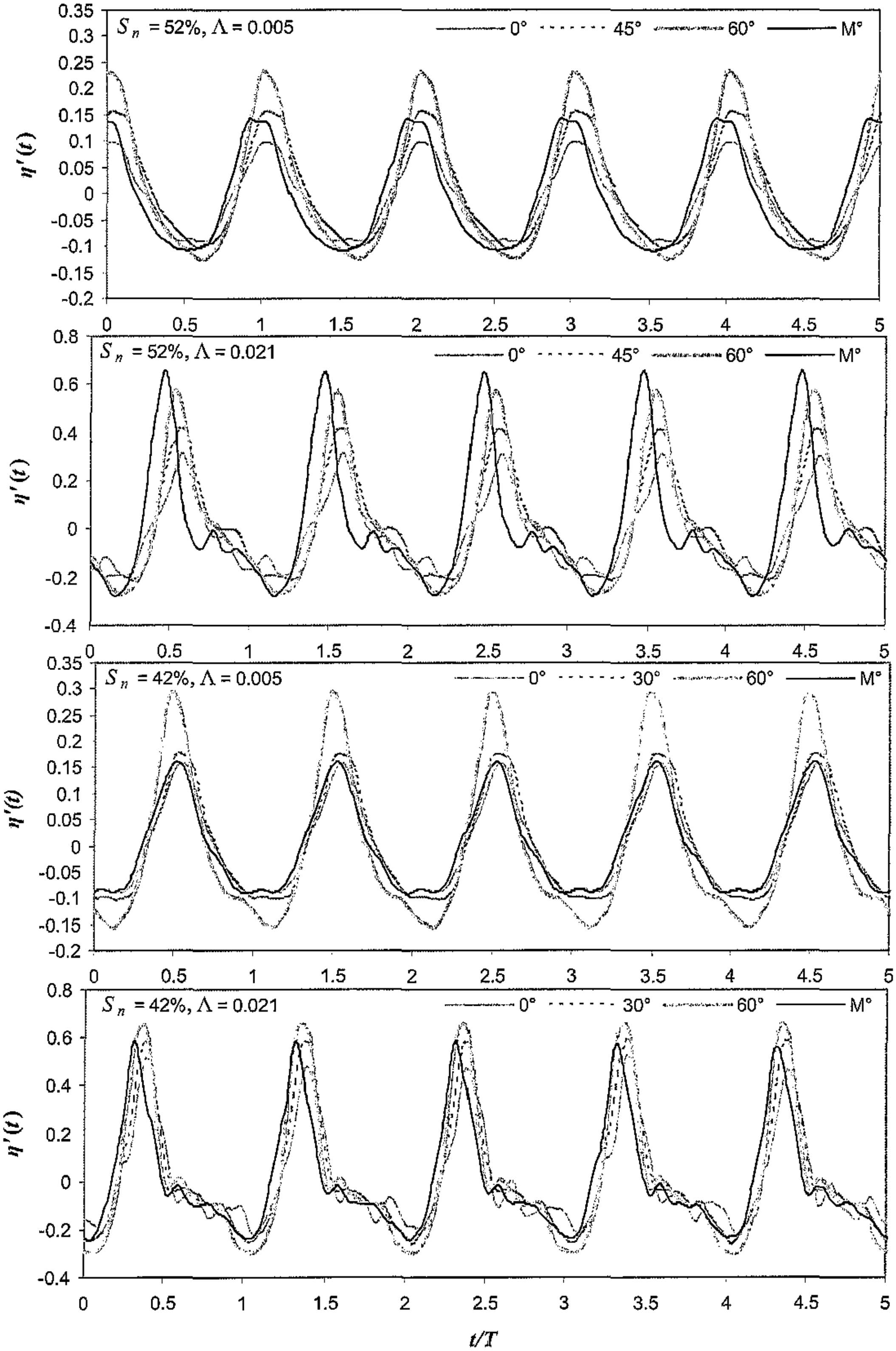

Figure 5.11. Free-surface response, $\eta'(t)$, near end walls for moving and fixed-angle tests @ β = 1.01.

5.6 Summary and Conclusions

The implementation of smart screens as rotating screens in a tuned liquid damper to oscillate freely under the sloshing water motion was presented experimentally. The main goal of this chapter was to present the findings associated with inserting a set of screens that automatically changed angle under varying excitation amplitudes. This change in screen angle with fluid response results in a more invariable level of inherent TLD damping and, ultimately for design, a more effective vibration absorber over a range of excitation amplitudes. Figure 5.6 demonstrated this by showing that the symmetric fixed-angled screens maintained a near-constant peak E_w' over a three-fold range of excitation amplitudes. The oscillating screens in this chapter demonstrated the intended effect of automatically changing C_θ with increasing excitation. A reduced gap in peak E_w' between amplitudes (compared to "normal" vertical screens seen in Figure 3.14) was found for the oscillating screens and this trend was more pronounced for h = 110mm (h/L = 0.114). This automatic adjustment of the pressure-loss and corresponding enhanced invariableness in damping provided by the freely oscillating screens are in agreement with the proposal and simulations initially conducted in Cassolato and Tait (2005).

Although the spring configuration employed in this chapter for screen motion did not result in a constant level of inherent TLD damping, the level of damping provided by the oscillating screens was found to be more invariable compared to fixed-angle screens. Initial findings from this preliminary study indicate that oscillating screens (a full implementation of passive *smart screens*) have merit and may be used to improve the performance of a TLD.

CHAPTER 6: THEORETICAL STUDY OF SYMMETRICALLY-ANGLED SLAT-SCREENS IN A STRUCTURE-TLD SYSTEM

6.1 Introduction

*Tuned liquid damper*s (TLD) are traditionally used as passive *dynamic vibration absorber*s (DVA) in the application of tall structures subjected to wind-induced excitation because of their effectiveness and their natural activation mechanism for the restoring force onto the structure (Soong and Dargush 1997). Kaneko and Ishikawa (1999) stated that techniques for designing optimal TLDs were lacking and developed a non-linear numerical model, which was subsequently enlisted to investigate the effectiveness of a TLD with a submerged net (screen). Tait (2004) expanded and implemented Kaneko's model for multiple submerged slat-screens and determined the effectiveness of a structure-TLD system, both numerically and experimentally, and found that the screens can be optimally designed for a single structural response amplitude.

Previous chapters primarily focused on the impact of fixed-angle or oscillating slat-screens on the dynamic response behaviour of a TLD under sinusoidal excitation. Wind excitation is often modelled by random (white-noise) excitation since a wind spectrum is fairly constant over the resonant domain of the frequency-response of the structure.

This chapter demonstrates that an idealized TLD equipped with angled screens can operate optimally over a range of structural response amplitudes. This chapter employs the theoretical model (§4.5), which was developed and verified in Chapter 4. The main goal of this chapter is to study the effect of adjustable symmetrically-angled damping screens and their variable pressure-loss with angle (C_θ) properties on the performance of a hypothetical structure-TLD system. The ability to optimize the effective damping provided by the TLD over a *range* of structural response is addressed. First, a background on the mathematical theory developed to describe the performance of a structure equipped with a DVA under a white-noise force spectrum is presented.

6.2 Structure-DVA Systems

The response of a structure equipped with a DVA, otherwise known as a *Structure-DVA system*, is a function of four main parameters (Tait 2004):

- Mass ratio,

$$\mu = \frac{\phi^2 m_a}{M^*} \tag{6.1}$$

where ϕ is the modal amplitude of the structure at the damper location (taken as $\phi = 1$ in this study) and m_a is the DVA mass. For the TLD, $m_a = m_{eff}$, the participating effective mass derived in Equation (4.52). M^* is the generalized mass of the primary structure for the targeted mode of vibration to be suppressed,

$$M^* = M^* + m_o \tag{6.2}$$

which includes the non-participating mass (Figure 1.2(c)) of the fluid in the TLD, m_o,

$$m_o = m_w - m_{eff} = \rho bhL - m_{eff} \tag{6.3}$$

- Tuning ratio,

$$\alpha = \frac{f_a}{f_s} \tag{6.4}$$

where f_a is the fundamental natural frequency of the DVA and f_s is the modal natural frequency of the generalized primary structure with generalized stiffness, K^*; f_s is defined as,

$$f_s = \frac{1}{2\pi}\sqrt{\frac{K^*}{M^*}} \tag{6.5}$$

For a TLD undergoing small response amplitudes, $f_a \approx f_n$, the fundamental sloshing frequency ($n = 1$) derived earlier in Chapter 4, given here as,

$$f_n = \frac{1}{2\pi}\sqrt{\frac{\pi g}{L}\tanh\frac{\pi h}{L}} \tag{6.6}$$

It should be noted that a non-linear analysis with amplitude-dependent natural frequency is beyond the scope of this study and only the linear sloshing frequency defined above shall be considered for all structural amplitudes, which has been shown to be experimentally valid for TLDs equipped with screens up to $\Lambda \approx 0.010$ in Chapter 3. The reduced hardening characteristics of symmetrically-angled screens for increasing screen angle, θ, (§3.6) support the use of Equation (6.6) for the linear analysis in this chapter.

- DVA damping ratio,

$$\zeta_a = \frac{c_a}{4\pi m_a f_a} \tag{6.7}$$

where c_a is the viscous damping of the DVA. For the TLD, $c_a = c_{eq}$, the equivalent linear viscous damping for a particular form of excitation. Therefore, $\zeta_a = \zeta_{eq} + \zeta_w$, the corresponding equivalent linear viscous damping ratio for the TLD including boundary layer damping (Equation (4.45)). Note that $\zeta_w << \zeta_{eq}$ and $\zeta_a \approx \zeta_{eq}$.

- Structural damping ratio,

$$\zeta_s = \frac{C^*}{4\pi M^* f_s} \tag{6.8}$$

The fourth parameter includes the viscous generalized modal damping of the primary structure, C^*. The performance of a TLD is weakly dependent on ζ_s.

Following the formulation of the response of the TLD as an analogous TMD as in Chapter 4 and employing the linearization process for a random white-noise excitation as given by Vickery et al. (2001), the TLD equivalent linear damping ratio, ζ_{eq}, results in,

$$\zeta_{eq} = \sqrt{\frac{32}{\pi}}\left(C_0\Theta_x + C_{0z}\Theta_z\right)\tanh^2\frac{\pi h}{L}\cdot\frac{\sigma_r}{L^2} \tag{6.9}$$

where σ_r is the *root-mean-square* (RMS) response of an equivalent linear TMD. Note that the same relationship between TMD motion response and TLD fluid response, Γ, holds for the random excitation case, i.e.,

$$\sigma_\eta = \Gamma \cdot \sigma_r \tag{6.10}$$

where σ_η is the RMS fluid response amplitude of the generalized coordinate and Γ is the modal participation factor as defined in Equation (4.41).

Numerous studies have determined criteria-dependent optimal tuning ratio, α_{opt}, and optimal damping ratio, $\zeta_{a\text{-}opt}$, values for DVAs as described in §1.6. For the special case of zero structural damping, $\zeta_s = 0$, closed form algebraic solutions have been formulated (Warburton 1982). For a linear structure-TMD system excited by white-noise excitation applied to the primary structure with no damping, $\zeta_s = 0$, the H_2 optimization values for tuning ratio and damping ratio are given as (Warburton 1982),

$$\alpha_{opt} = \frac{\sqrt{1+\mu/2}}{1+\mu} \tag{6.11}$$

$$\zeta_{a-opt} = \sqrt{\frac{\mu(1+3\mu/4)}{4(1+\mu)(1+\mu/2)}} \tag{6.12}$$

For structures having well-separated vibration modes, a structure-DVA system can be accurately modelled as a *two-degree-of-freedom* (2DOF) system as shown in Figure 1.1. The parameters commonly used to evaluate the performance of a structure-TLD system are the efficiency, effectiveness, and robustness (Tait 2004). These parameters are utilized in this chapter to study the performance of the TLD shown in Figure 2.1, which is equipped with symmetrically inclined slat-screens. The effectiveness of a TMD can be expressed in terms of the amount of additional effective viscous damping that it adds to the primary structure (Vickery and Davenport 1970), symbolized by the effective viscous damping ratio, ζ_{eff}. This can be accomplished by equating the area under the frequency-response of the combined system to that of a *single-degree-of-freedom* (SDOF) system with the same frequency and solving for the effective damping, ζ_{eff} (McNamara 1977). Gerges and Vickery (2003) reported a general closed form expression for the effective viscous damping ratio in a damped structure under a white-noise force spectrum, developed by McNamara (1977) as,

$$\zeta_{eff} = \frac{(1+\mu)^2\alpha^4\zeta_s\zeta_a+(1+\mu)\left(2\alpha\zeta_s\zeta_a+2\zeta_a^{\ 2}-1\right)2\alpha^2\zeta_s\zeta_a+\alpha\mu\left(\alpha^2\zeta_s^{\ 2}+2\alpha\zeta_s\zeta_a+\zeta_a^{\ 2}\right)+\zeta_s\zeta_a\left(4\alpha^2\zeta_s^{\ 2}+4\alpha\zeta_s\zeta_a+1\right)}{(1+\mu)^2\alpha^4\zeta_a+(1+\mu)2\alpha^2\zeta_a\left(2\alpha\zeta_s\zeta_a+2\zeta_a^{\ 2}-1\right)+\alpha^2\mu\left(\alpha\zeta_s+\zeta_a\right)+\zeta_a\left(4\alpha^2\zeta_s^{\ 2}+4\alpha\zeta_s\zeta_a+1\right)}-\zeta_s \tag{6.13}$$

The ratio of the RMS DVA relative displacement, σ_r, to the RMS structure displacement, σ_s, at the DVA location in the structure, $R=\sigma_r/\sigma_s$, can be obtained from McNamara (1977) as (Gerges and Vickery 2003),

$$R = \sqrt{\frac{\alpha\zeta_s+\zeta_a}{(1+\mu)^2\alpha^4\zeta_a+(1+\mu)2\alpha^2\zeta_a\left(2\alpha\zeta_s\zeta_a+2\zeta_a^{\ 2}-1\right)+\alpha^2\mu\left(\alpha\zeta_s+\zeta_a\right)+\zeta_a\left(4\alpha^2\zeta_s^{\ 2}+4\alpha\zeta_s\zeta_a+1\right)}} \tag{6.14}$$

For the special case of zero structural damping, $\zeta_s = 0$, R and ζ_{eff} can be simplified to, respectively,

$$R=\left[(1+\mu)^2\alpha^4+(1+\mu)2\alpha^2\left(2\zeta_a^{\ 2}-1\right)+\alpha^2\mu+1\right]^{-\frac{1}{2}} \tag{6.15}$$

$$\zeta_{eff}=\frac{\alpha\mu\zeta_a}{(1+\mu)^2\alpha^4+(1+\mu)2\alpha^2\left(2\zeta_a^{\ 2}-1\right)+\alpha^2\mu+1}=\alpha\mu\zeta_a R^2 \tag{6.16}$$

The optimal parameters for the effective damping, $\zeta_{eff\text{-}opt}$, and the response ratio, R_{opt}, for zero structural damping can be obtained by substituting Equations (6.11) and (6.12) into Equations (6.15) and (6.16), resulting in,

$$\zeta_{eff-opt} = \frac{1}{4}\sqrt{\frac{\mu(1+\mu)}{1+3\mu/4}} \tag{6.17}$$

$$R_{opt} = \frac{1+\mu}{\sqrt{\mu(2+3\mu/2)}} \tag{6.18}$$

The efficiency, Ψ, of the TLD, defined here as the amount of effective damping the TLD provides, compared to an optimal equivalent linear TMD *with the equivalent TMD mass* = m_{eff} (Equation (6.1)), expressed as a percentage is,

$$\Psi = \frac{\zeta_{eff}}{\zeta_{eff-opt}} \cdot 100\% \tag{6.19}$$

yielding 100% efficiency at the target structural response amplitude.

The structure-DVA system can be modelled as an equivalent SDOF mass-spring-damper system with effective damping (Figure 1.11). Equations (6.15) through (6.19) are valid for the assumption of $\zeta_s = 0$. Since ζ_{eff} depends only weakly on ζ_s, ζ_{eff} computed with the assumption of no structural damping is an adequate approximation (Vickery et al. 2001).

While efficiency is determined by the effective damping, ζ_{eff}, provided to the primary structure (Equation (6.19) above), the robustness is described as the changes in effectiveness with changes in tuning ratio (α), TLD damping ratio (ζ_a), and structural response amplitude. Since TLD inherent damping is found to be amplitude-dependent (Reed et al. 1998, Sun et al. 1995), the robustness of a TLD depends on the range of excitation amplitudes and affected tuning ratio, α (Tait 2004). The TLD is modelled using linear potential flow theory as described in §4.5 and, therefore, no amplitude-dependent hardening characteristics are considered. Results have shown the linear model can reasonably predict the response of a TLD with increasing screen angle (§4.7), given the negligible hardening response over θ found experimentally (§3.6). For the structure-TLD performance to be demonstrated in the following section, the tuning ratio is assumed to maintain its optimal value, α_{opt}. Therefore, the robustness due to mis-tuning shall not be addressed. It should be noted that non-linear amplitude-dependent simulations for angled screens are recommended for future study.

6.3 Linear Structure-TLD System Performance

Theoretical system performance due to random white-noise excitation applied to the primary structure is addressed in this section. The ability of the symmetrically-angled screens to extend TLD efficiency, Ψ, over a range of excitation amplitudes is the focus. A parametric study on the mass ratio, μ, is conducted (see Equations (6.17) and (6.18)). The efficiency, Ψ, for different screen angles, θ, versus various target structural response amplitudes and θ versus the same response amplitudes at different μ values is addressed. First, the parameters used to model the TLD and the structural response is presented.

6.3.1 Description of Response Formulation

The effective damping is calculated utilizing the potential flow model of §4.5 for the TLD response and the system equations of §6.2. The main parameter that determines the performance of the TLD is the equivalent linear damping ratio, ζ_{eq}, given in Equation (6.9)—recall that $\zeta_a \approx \zeta_{eq}$. The damping of liquid sloshing is an important parameter affecting the effectiveness of the TLD (Sun et. al 1995). This parameter depends on the fluid pressure-loss coefficient, C_θ, and related screen angle, θ. C_θ derived in §4.3.2 is utilized, which is reproduced below,

$$C_\theta = \left(\frac{\cos\theta}{C \cdot \cos\psi} - 1 \right)^2 \tag{6.20}$$

with $\psi = 0.80\theta$ assumed for $\theta \leq 45°$ and for $45° < \theta \leq 60°$,

$$\psi/\theta = \begin{cases} 0.80 + \dfrac{\theta - 45°}{60° - 45°}(0.90 - 0.80); & S_n = 42\% \\ 0.80 + \dfrac{\theta - 45°}{60° - 45°}(0.85 - 0.80); & S_n = 52\% \end{cases} \tag{6.21}$$

ψ is linearly interpolated to the assumed values at 60° given in §4.7.1.

The TLD equipped with the S_n = 42% screen configuration was initially designed for a mass ratio of 2% (Tait 2004), falling within a typical range of $\mu \leq$ 5% in most DVA applications for tall structures. Particular values of mass ratio, chosen here, are μ = 0.5%, 1%, 2%, and 3.5% for the parametric study.

A *peak factor* (PF) of approximately 3.75 is predicted for the hypothetical structure using (Davenport 1964),

$$PF = \sqrt{2\ln(\nu T_o)} + \frac{0.5772}{\sqrt{2\ln(\nu T_o)}} \tag{6.22}$$

where ν is the cycling frequency and T_o is the averaging time corresponding to hourly peaks. The cycling frequency is often taken as the natural frequency of the structure, $\nu = f_s$ (Boggs 1997). The RMS structural acceleration, $\ddot{\sigma}_s$, is multiplied by the peak factor to obtain an estimate of the peak-hourly structural acceleration, $\hat{\ddot{x}}_S$, typically expressed in *milli-g* (denoted as "mg" in this study).

The calculations continue with the TLD optimally tuned, α_{opt}, and optimally damped, $\zeta_{a\text{-}opt}$, Equations (6.11) and (6.12), respectively. Target $\hat{\ddot{x}}_S$ values are calculated for each set of screens at the normal vertical position, 0° (for Ψ = 100%). For incremental values of $\hat{\ddot{x}}_S$, the screens are rotated to maintain 100% efficiency. Given the experimental (practical) limit of screen rotation and maximum building acceleration criteria discussed in §1.5, the screens are rotated until $\theta \approx 60°$ or $\hat{\ddot{x}}_S = 30\text{mg}$.

6.3.2 Improved Efficiency Over a Range of Structural Response

From the procedure in §6.3.1, the efficiency curves of Figure 6.1 through Figure 6.4 are generated for different mass ratios, μ, demonstrating the ability of angled screens to extend the efficiency over a range of structural response amplitudes. This chapter assumes that a mechanism exists to adjust the screens to a desired symmetric screen inclination. The y-axes are the efficiency, Ψ, given by Equation (6.19) and the x-axes are the peak-hourly structural acceleration, $\hat{\ddot{x}}_S$.

In Figure 6.1 through Figure 6.4, individual efficiency curves are plotted for particular values of $\hat{\ddot{x}}_S$. The value of $\hat{\ddot{x}}_S$ corresponding to Ψ = 100%, for each individual curve, is indicated in the legend along with the corresponding (symmetric) screen angle, θ. As can be seen, vertical screens (0°), for a given solidity, can be designed to operate optimally for only one particular structural response acceleration. Throughout the different screen angles, an envelope efficiency curve can be drawn capturing 100% efficiency over a range of structural response accelerations as shown in each figure. The value of efficiency at $\hat{\ddot{x}}_S = 30\text{mg}$ is indicated with a vertical line and arrow pointing to the envelope curves in Figure 6.1 through Figure 6.4. Recall from §1.5 that 30mg is often used as a maximum allowable acceleration with respect to serviceability criteria. The envelope curves ("env." in legends) highlight the angled screens ability to maintain 100% efficiency over a range of structural response accelerations compared to conventional vertical screens, which can only obtain $\Psi = 100\%$ at one structural response acceleration. For example, in Figure 6.1 at $\mu = 1.0\%$, vertical screens optimally designed at 3mg would only achieve $\Psi \approx 55\%$ at a structural acceleration of 30mg. The angled screens are optimally designed for a range of structural response from the vertical position at 3mg rotating to their maximum angle for $\Psi = 100\%$ through 12mg. At a large amplitude of 30mg, the angled screens maintain an efficiency of 92% at an angle $\theta \approx 60°$.

Furthermore considering the $S_n = 42\%$ screens that were originally designed for $\mu = 2\%$, their optimal damping in their conventional vertical position (0°) can now be extended through a three-fold range of structural response amplitude (Figure 6.4). In particular, the θ and corresponding $\hat{\ddot{x}}_S$ values are (rounded): 0° for 10mg, 30° for 15mg, 40° for 20mg, and 60° for 30mg.

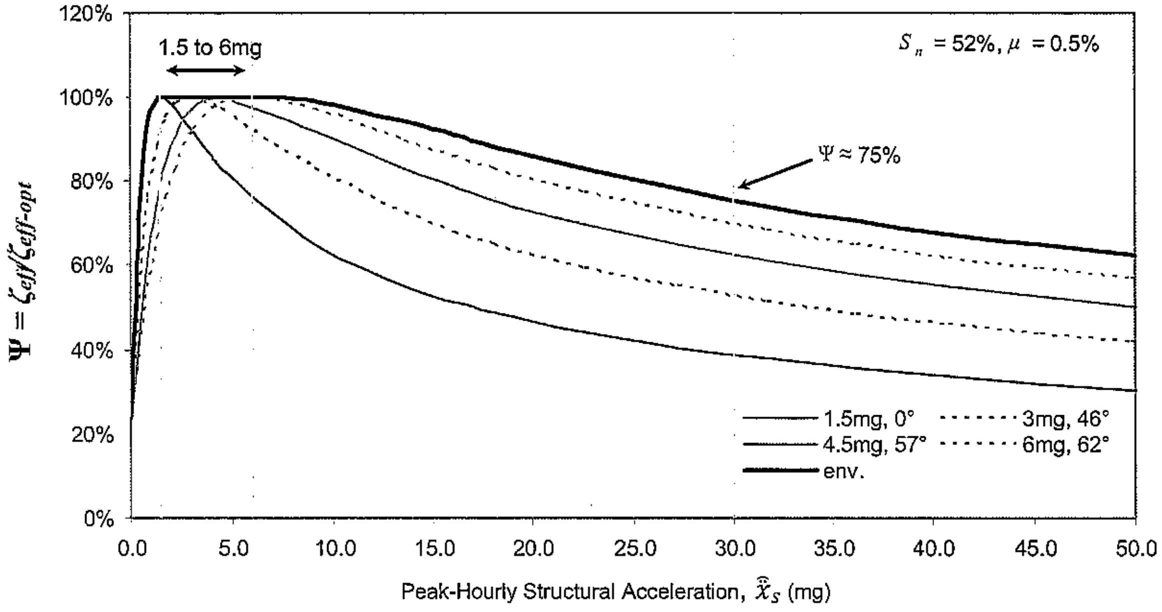

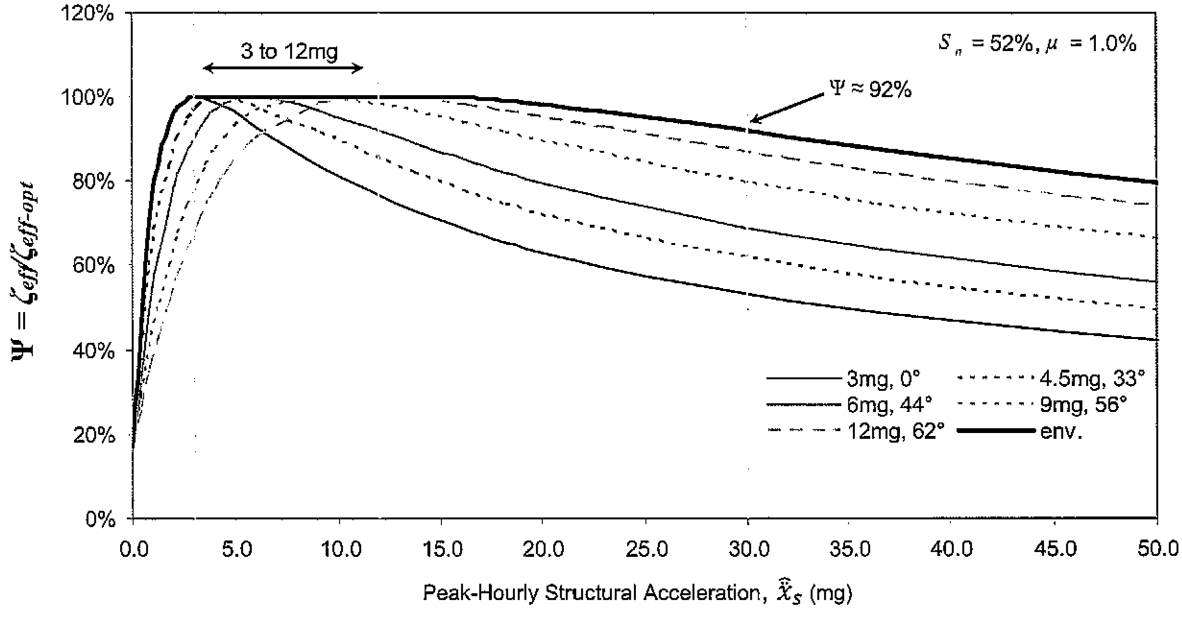

Figure 6.1. Efficiency over range of structural response. $S_n = 52\%$, $\mu = 0.5$ & 1.0%

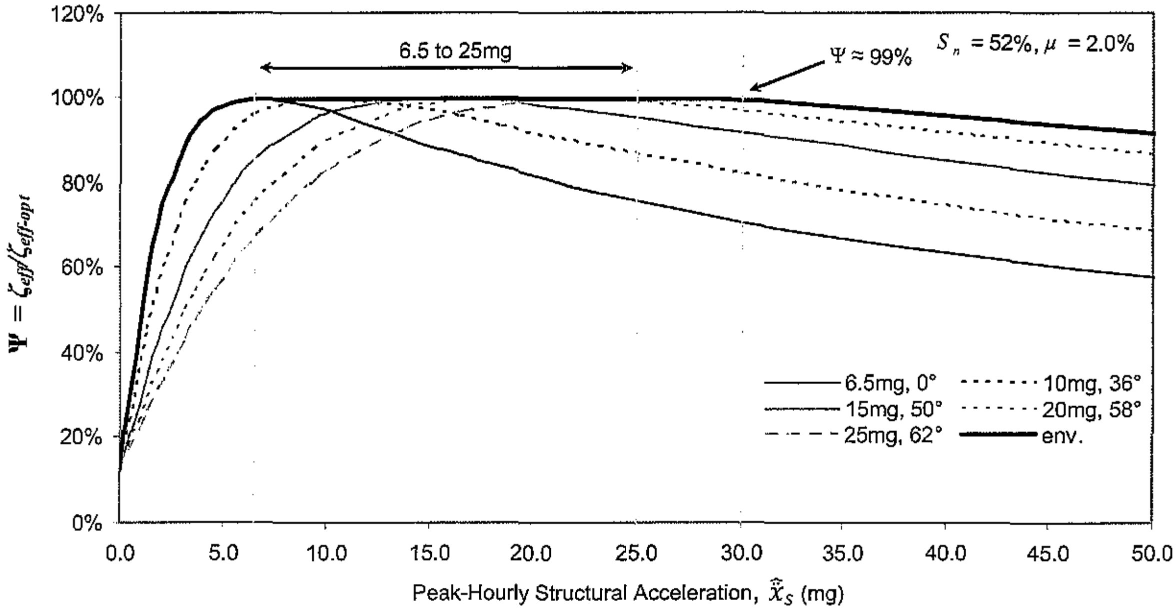

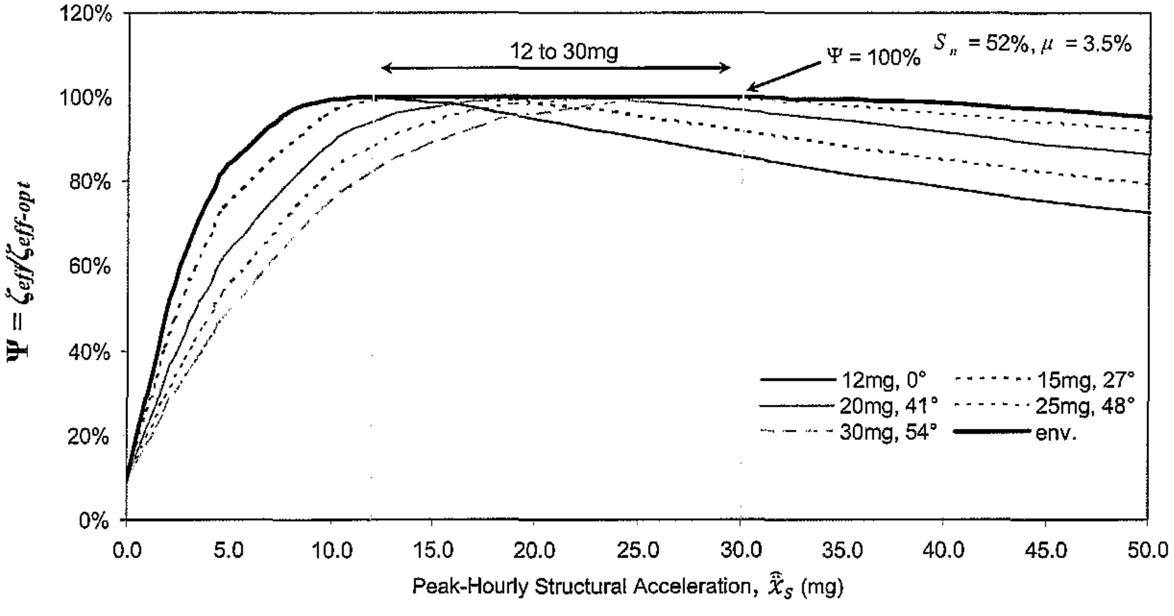

Figure 6.2. Efficiency over range of structural response. S_n = 52%, μ = 2.0 & 3.5%

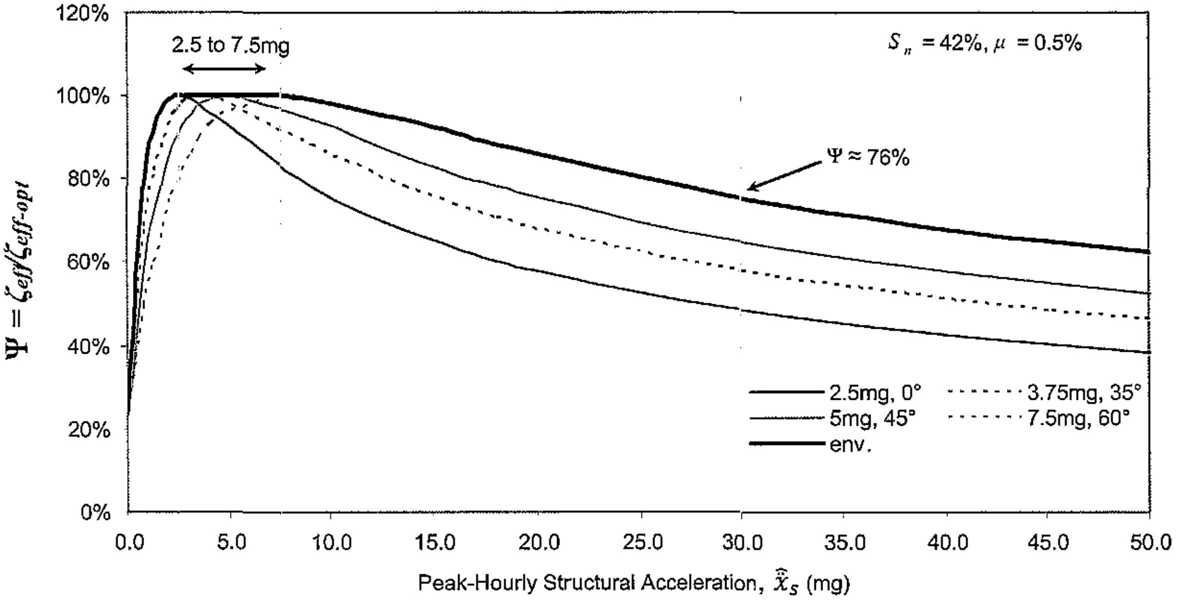

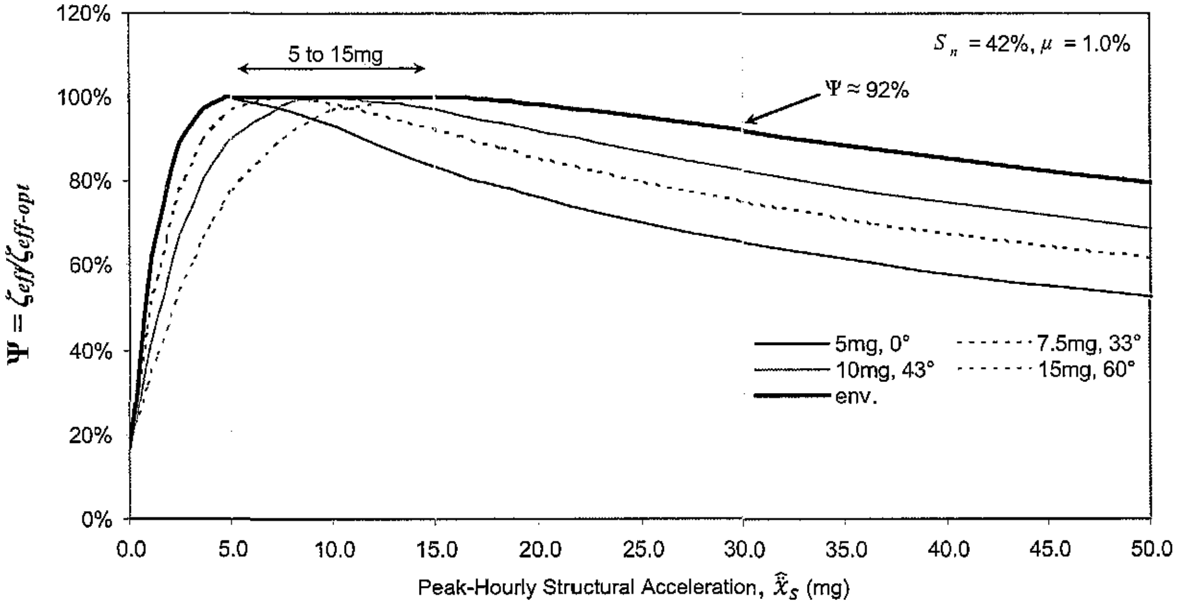

Figure 6.3. Efficiency over range of structural response. $S_n = 42\%$, $\mu = 0.5$ & 1.0%

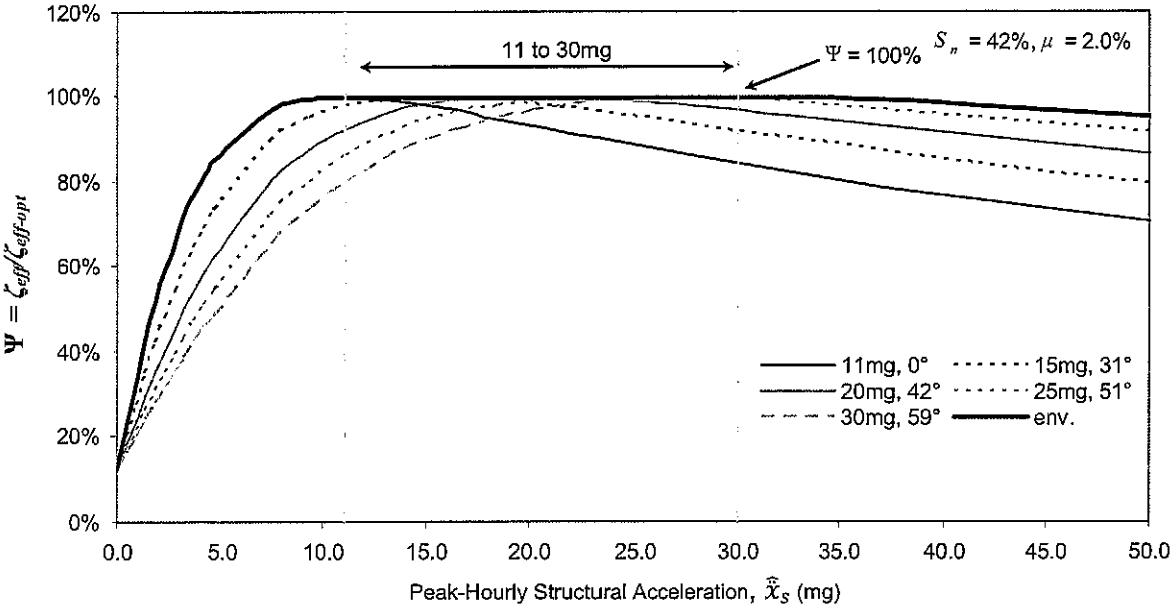

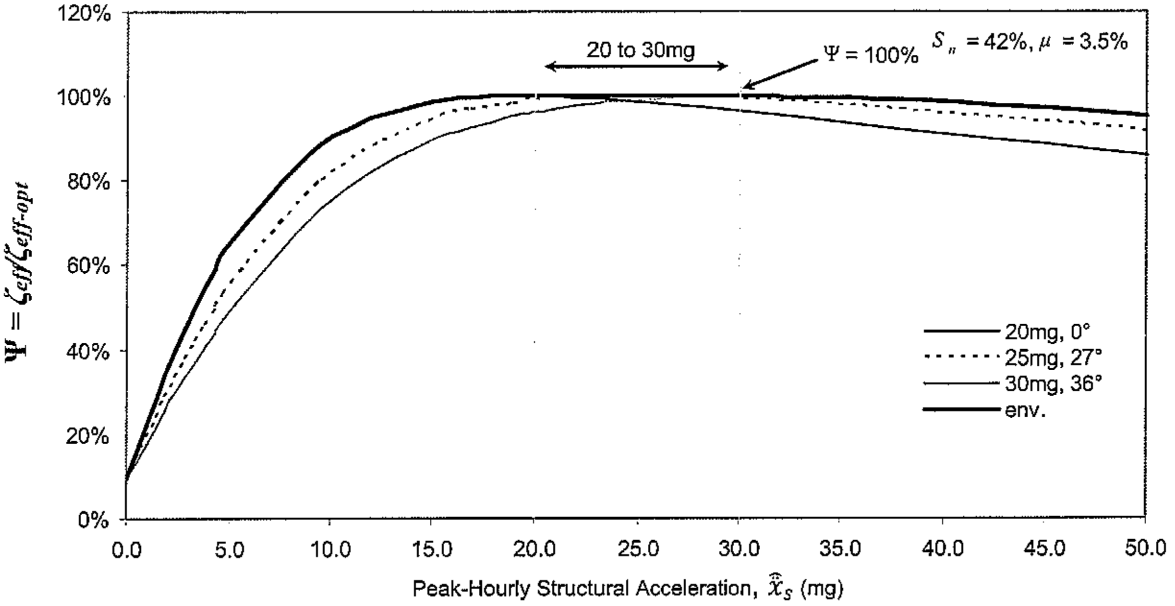

Figure 6.4. Efficiency over range of structural response. S_n = 42%, μ = 2.0 & 3.5%

The benefit of damping screens in a symmetric inclination could also be utilized in a semi-active mode of control. Vertical screens could be optimally designed for a particular target structural response acceleration as discussed before and when the structural response deviates from the target $\hat{\ddot{x}}_S$ a feedback mechanism could be implemented to readjust the screens to some inclined position. In the event of a power failure there remains a considerable amount of ζ_{eff} associated with typical motionless screens—particularly for mid-range screen inclinations ($\theta \approx 30°$) as opposed to common 0° screens, over the target $\hat{\ddot{x}}_S$ ranges.

To compare screen solidity, the extent of screen rotation for each set of screens at the various mass ratios is shown in Figure 6.5. The differences between screen solidity are once again evident in the figure by the required screen rotation at a particular μ for a certain $\hat{\ddot{x}}_S$. The 52% screens will achieve $\zeta_{eff\text{-}opt}$ at a lower $\hat{\ddot{x}}_S$ than the 42% screens. As $\hat{\ddot{x}}_S$ increases, the 52% screens will be required to rotate through a greater screen angle, θ, in order to maintain $\zeta_{eff\text{-}opt}$ (and $\zeta_{a\text{-}opt}$) for a particular μ. As the mass ratio is increased, a greater level of ζ_a is required. For example, at the highest mass ratio, $\mu = 3.5\%$, at a target $\hat{\ddot{x}}_S = 15$mg, the 42% screens are unable to provide sufficient ζ_a even in their vertical position (also see Figure 6.4). The 52% screens can provide $\zeta_{a\text{-}opt}$ at a screen angle of approximately, $\theta \approx 20°$. At a target $\hat{\ddot{x}}_S = 20$mg, the 42% screens achieve $\zeta_{a\text{-}opt}$ in their vertical position, whereas the 52% screens require a screen angle of $\theta \approx 42°$. At $\hat{\ddot{x}}_S = 30$mg, the 42% screens require $\theta \approx 36°$, whereas the 52% screens require $\theta \approx 54°$.

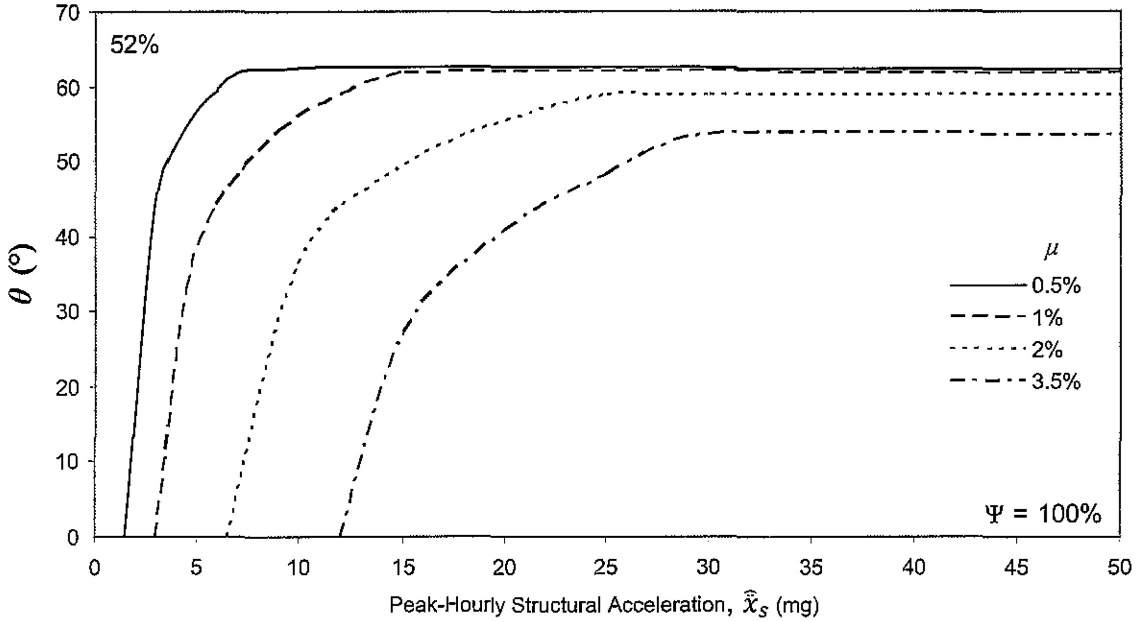

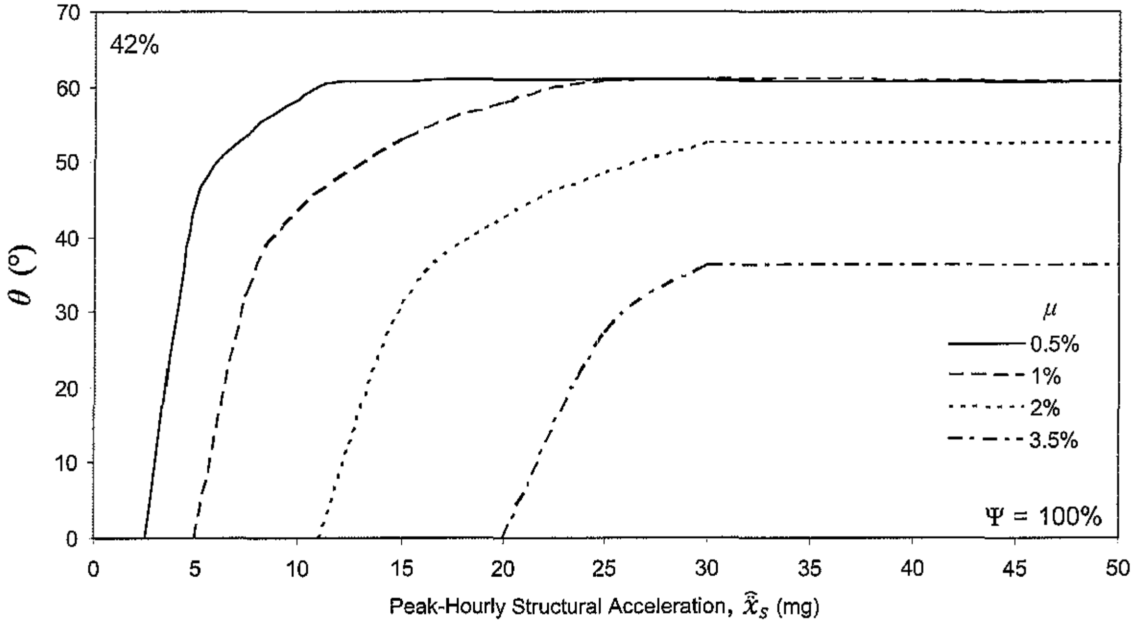

Figure 6.5. Symmetric screen rotation at various mass ratios.

Figure 6.5 highlights the larger angles needed in order to maintain $\zeta_{a\text{-}opt}$ for the higher screen solidity. In addition, Figure 6.5 is a valuable initial design aid as it permits the range of θ resulting in $\Psi = 100\%$ to be identified. Also, a figure of this type can be used as a look-up table for semi-active control as described by Yalla and Kareem (2003). Gain scheduling is an open-loop control scheme with a non-linear regulator whose parameters are changed as a function of the operating conditions in a pre-programmed way (Astrom and Wittenmark 1989), which can be employed in the semi-active control scheme discussed. In gain scheduling, the regulator parameters can be changed very quickly in response to process dynamics (Yalla and Kareem 2003). The look-up table, shown in Figure 6.5, is the gain scheduler, the regulator is the controllable inclination of the symmetric damping screens, and the pressure-loss coefficient, C_θ, is the parameter being changed. Gain scheduling is an efficient control scheme for maintaining optimal damping in TLDs, where the process dynamics is the structure-TLD system. For a given structural response acceleration, C_θ is changed in accordance with the look-up table (Figure 6.5).

6.4 Summary and Conclusions

Vertical damping screens used in TLDs can be optimally designed for only one particular structural response acceleration. This chapter has theoretically shown that the symmetrically-angled screens of Chapters 3 and 4 with a variable loss coefficient, C_θ, can extend the optimization of vertical damping screens and increase their efficiency through screen rotation over a range of structural response. On average, this range of target structural response maintaining Ψ = 100% was found to be approximately a three-fold range (see Figure 6.1 through Figure 6.4), which is ideal for typical target acceleration values corresponding to the 1 in 10 year event in the range of 10 to 30mg.

Although ideally smart screens would adjust their angle passively, Chapter 5 has shown that more experimental work must be undertaken in order to develop a suitable screen arrangement that would result in invariable damping, without the undesirable frequency-hardening characteristics. However, the smart screen concept of adjusting the screen loss coefficient and corresponding damping of the TLD, ζ_a, with increasing structural response has been demonstrated in this chapter. Practically, the symmetrically-angled screens considered in this chapter must be adjusted via some feedback mechanism or semi-active control that adjusts the screen angle upon measuring structural response.

A plausible semi-active control method utilizing look-up tables ("gain scheduling") similar to Figure 6.5 could be implemented in order to adjust the screen inclination to obtain $\zeta_{a\text{-}opt}$ in the absorber (and $\zeta_{eff\text{-}opt}$ of the combined structure-TLD system) over a range of structural response accelerations.

CHAPTER 7: CONCLUSIONS AND RECOMMENDATIONS

7.1 Summary and Conclusions

The research conducted in this thesis consisted of the dynamic response and performance of a 1-D *tuned liquid damper* (TLD) equipped with two damping screens located at 0.4*L* and 0.6*L*. In particular, two main configurations of the damping screens were employed: (1) at symmetric fixed-angle positions measured at 0° from the vertical position to investigate the effect of screen inclination on the inherent damping and energy dissipation; and (2) in an oscillating parallel-linked configuration to investigate increased damping invariableness (and the similar characteristics in energy dissipation) with excitation amplitude as the screens oscillated passively inside the tank (a full implementation of *smart screens*). See Figure 7.1 below.

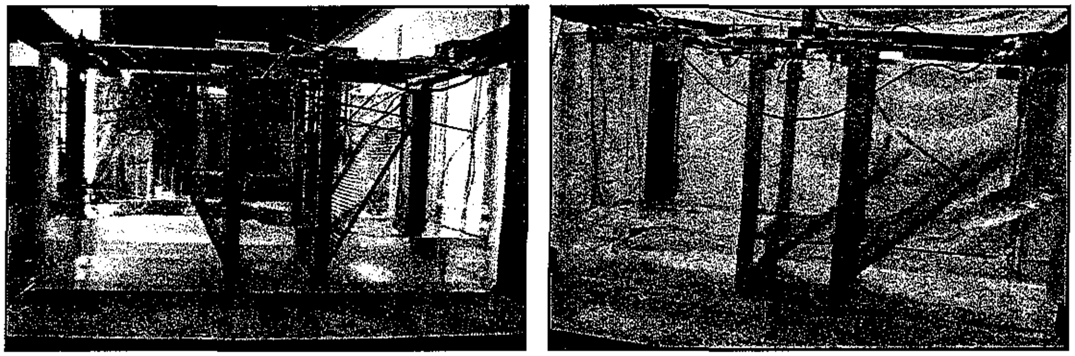

Figure 7.1. Symmetric fixed-angle (left) and parallel-linked oscillating (right) configurations.

Experimentally, each configuration was tested under sinusoidal excitation over a large range of excitation amplitudes. The practical performance was assessed through measurement of the screen forces, free-surface response, and the inertial forces resulting from the sloshing liquid motion. The energy dissipation (frequency-response) over a cycle of motion was the key descriptor in determining the performance of the TLD.

Theoretically, research was conducted to formulate the pressure-loss characteristics of the angled sharp-edged horizontal-slat screens. Mathematical models were developed to simulate the sloshing fluid response found in experiments conducted utilizing two linear flow models: shallow water wave theory and potential flow theory. Subsequently, the efficiency of a TLD equipped with symmetrically-angled damping screens in a hypothetical structure-TLD system under random excitation was investigated. The effect of angled damping screens was shown to improve the efficiency of the damper over a range of structural response accelerations.

7.2 Research Findings

Conclusions pertaining to the previous four main research chapters shall be summarized here.

7.2.1 Experimental Performance of Symmetric Fixed-Angle Horizontal-Slat Screens in a TLD

Research consisted of experimentally determining the performance characteristics of angled screens in a TLD. Using a shake-table and test set-up, described in detail in Chapter 2, the damping screens were rotated to discrete fixed inclinations to measure the various fluid response characteristics at each inclination. The frequency-response of the TLD at each screen angle was examined in detail. The following conclusions were made:

- For the frequency domain, the overall TLD performance was examined using energy dissipation. The dissipation per cycle at each frequency is a convenient way of examining the frequency-dependent performance of a damper in general, rather than using force vectors, their direction, and their minima or maxima.
- Screen angle reduces the damping effect of the screens with increasing angle and the change in energy dissipation is found to be relatively consistent over the range of amplitudes tested
- The effect of inclined screens on inherent TLD damping, ζ_a, has demonstrated that one set of inclined screens can dissipate an equivalent amount of energy as another set of vertical screens having a different solidity. This makes it possible to replace multiple sets of screens with one, conceivably adjusting its angle with excitation amplitude to target an optimal design performance through a *range* of excitations
- Experimental results show that despite the natural amplitude-dependent response hardening (increase in peak response frequency) due to increasing free-surface response, more significant free-surface response due to increased screen angle does not lead to a significant change in the

resonant frequency, which greatly aids in keeping the TLD in-tune with a structure

- In conjunction with the previous point, the free-surface response amplitude, η, increases greatly with increasing θ without significant frequency-hardening, unlike the behaviour of increasing η linked with increasing excitation amplitude, A. The phase, φ, of η was shown to harden (increase in β) only slightly at high screen angles early in Chapter 3.

7.2.2 Linear Simulation of Symmetric Fixed-Angle Slat-Screens in a TLD

A theoretical pressure-loss coefficient, C_θ, for a sharp-edged horizontal-slat screen at an angle θ was developed. C_θ was employed in two linear flow models that were used to predict the response of the TLD equipped with the fixed-angle screens: one being shallow water wave theory and the other, potential flow theory. As stated previously, a non-linear study capturing the effect of higher harmonics is beyond the scope of this thesis. The drag (or pressure-loss) coefficient was experimentally validated for both the 42% and 52% solidity screens at their vertical position (0°). Numerous comparisons were made between the linear models and experimental results. Good agreement was found, particularly for the potential flow model at the low- to mid-range of excitation amplitudes tested. The linear numerical models presented could be used to efficiently estimate the response of the TLD in design. The following points summarize the main findings of this section of research:

- Various pressure-loss coefficients were examined. For the one developed in this study, the loss coefficient formulated by Baines and Peterson (1951), $C_l(S)$, was extended to include a function of the screen angle, $C_\theta(S,\theta)$, utilizing concepts of pressure-loss for an inclined screen from Yeh and Shrestha (1989)
- Equation (4.13) is equal to the formulation of the established use of the pressure-loss coefficient for a vertical screen ($\theta = 0°$) by Baines and Peterson (1951) and allows straightforward implementation of the loss of angled screens, independent of the incident flow velocity
- The two linear numerical models that were employed in this study are suitable and efficient for predicting the energy dissipation, E_w', of a TLD equipped with angled screens due to the dominance of the fundamental response (§4.7)—first mode dominance also shown in §5.4.
- The more rigorous potential flow model is found to accurately predict the TLD response in the RMS excitation amplitude range ($\Lambda < 0.016$)
- The simulated response depends on screen solidity, S, and deflection angle, $\psi(\theta)$. For the value of $\psi/\theta = 0.80$ selected for $\theta \leq 45°$, $\psi/\theta = 0.90$ at $\theta = 60°$ for $S_n = 42\%$, and $\psi/\theta = 0.85$ at $\theta = 60°$ for $S_n = 52\%$, the potential flow model, in particular, accurately predicts the TLD response at low

excitation amplitudes for screen angles $\theta \leq 45°$ and for screen angles $\theta > 45°$ when using the adjusted ψ/θ values

- All theoretical results are valid for $0.40 \leq S \leq 0.60$ and $\theta \leq 60°$, which are the practical values used in experimentation as well, assuming that the fluid losses are independent of the flow direction (§3.9)
- Findings from this chapter show that the potential flow model utilizing the pressure-loss coefficient developed, $C_{\theta 3}$, can be used to provide initial estimates of screen forces, the base shear forces, F_w', and corresponding energy dissipated, E_w', for preliminary design purposes

7.2.3 Experimental Performance of Oscillating Slat-Screens in a TLD

Chapter 5 investigated a full passive implementation of *smart screens*. Two sets of screens that oscillated under the sloshing fluid motion using a linear spring were tested. The goal was to investigate the benefits of this relatively simple configuration. The impact the oscillating (moving) screens had on the frequency-response were examined in detail including the effect of changing the depth ratio, h/L, to adjust the observed frequency-hardening characteristics, unlike the symmetric fixed-angle test results. For this particular TLD equipped with oscillating screens, the following conclusions were made:

- Although not optimized, the performance of the oscillating configuration yielded more invariable damping characteristics over the range of excitation amplitudes tested, $0.003 \leq \Lambda \leq 0.021$
- Contrasted with the fixed-angle experimental frequency-response, the moving configuration showed signs toward the practical goal of having a near-constant level of energy dissipation around resonance (near-constant damping)
- A reduction in depth ratio to $h/L = 0.114$ aided in limiting the hardening behaviour of the TLD response while providing increased damping invariability compared to experiments conducted at the regular water depth ratio throughout this study, $h/L = 0.123$, over a range of excitation
- Increased free-surface response and corresponding hardening characteristics at high excitation amplitudes, associated with rapid screen oscillation with high angles of inclination, limited the maximum testing amplitude
- This preliminary study of smart screens gives merit to the effect they would have on maintaining near-constant effective damping in a structure-TLD system over a range of structural response

7.2.4 Theoretical Study of Symmetrically-Angled Slat-Screens in a Structure-TLD System

This stage of research investigated the effect of adjustable angled damping screens on the performance of a structure-TLD system. To demonstrate the concept of invariable damping over a range of structural response utilizing the symmetrically-angled damping screens, the efficiency of such a structure-DVA system under white-noise excitation was quantified. The system performed at 100% efficiency, being optimally tuned and damped. A common trend resulted; this 100% efficiency in performance was extended through a three-fold range of peak-hourly structural (response) acceleration. For example, equipped with the S_n = 42% screens at a mass ratio of, μ = 2%, the TLD remained optimally damped through a targeted range of structural response from approximately 10 to 30 milli-g's (mg). Experimental findings of this nature are, of course, recommended for future study.

The theoretical study conducted showed that by altering the pressure-loss coefficient, by rotating the damping screens, the inherent TLD damping can be controlled to achieve a constant effective structure-TLD damping over a *range* of structural response. A semi-active control scheme of this nature implementing the concept of gain scheduling was also postulated utilizing a "look-up" table created for an open-loop form of structural response control. This open-loop control provides a quick parameter adjustment scheme for varying structural response where the parameter adjusted is the pressure-loss coefficient(s), C_θ, of the damping screen(s).

7.3 Recommendations for Future Study

This section presents recommendations for future work based on the research presented in this thesis.

- The experimental work on fixed-angle screens completed in this thesis was limited to only a single arrangement of damping screens (at $0.4L$ and $0.6L$) submerged in a single water depth ratio, h/L. Future experiments are recommended at different screen locations to determine the robustness of the linear flow models developed in this study. Deep-water behaviour ($h/L > 0.2$) with angled damping screens is also suggested for investigation
- Numerous studies on different tank shapes rather than the common rectangular shape studied in this thesis were mentioned in Chapter 1. The insertion of angled damping screens in combination with different tank shapes is recommended for future study
- Investigation into the damping characteristics at large peak excitation amplitudes representative of earthquakes for screens at a large inclination to determine the contribution of the vertical damping component at large amplitudes

- Non-linear numerical models to simulate fixed-angle and oscillating screen damping characteristics for both TLD and structure-TLD system modelling

Suggestions for alternate implementations of *smart screens*:

- Insert horizontal screens at ends of tank to damp vertical fluid velocity component while simultaneously limiting the motion of parallel-linked screens
- Parallel-linked screens oscillating by connection of a damper (dashpot) instead of a linear spring used in this study, designed to be proportional to fluid velocity at a target level of excitation. This may also reduce non-linear fluid response for a larger range of excitation amplitudes. Non-linear springs that are designed for a range of screen loads at different excitation amplitudes is also suggested
- The negligible peak response frequency-shifting (hardening) characteristics of symmetrically-angled screens appears to be a promising option, if it can be implemented in an automatically adjusting manner for passive control, ideal for "smart" screens
- Since passive control is desired, the effect of one screen tilting away from centre with the sloshing fluid while the other returns

temporarily vertical could be studied to determine its frequency-shifting and invariable damping benefits

- Screens rotating from a hinge connection at top of screen instead of bottom.

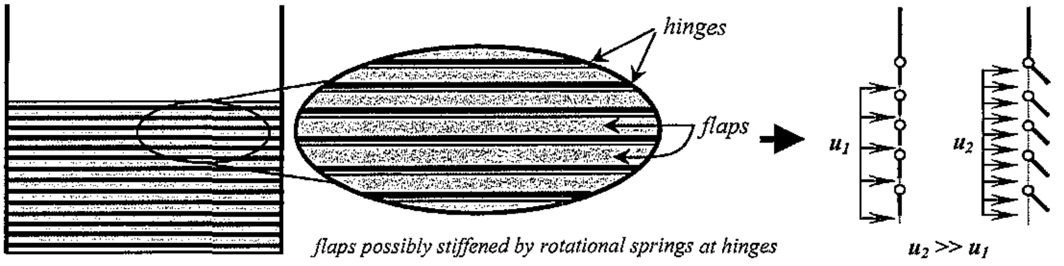

Figure 7.2. Slat-screen (left) with adjustable flaps (detailed, centre/right).

- A slat screen incorporating adjustable flaps (see Figure 7.2 above) with much more detail in screen design & fabrication. A slat screen with flaps effectively changes its solidity with changes in fluid velocity (and excitation amplitude) by opening & closing the flaps accordingly. Pressure-loss coefficients for such flaps can be found in Idelchik (1986), for example.
- The effect of the spring configuration or any other configuration (above) under random excitation should also be experimentally considered

REFERENCES

Asami, T., and Nishihara, O., "Closed-Form Exact Solution to H_∞ Optimization of Dynamic Vibration Absorbers (Application to Different Transfer Functions and Damping Systems)", *Journal of Vibration and Acoustics (Transactions of the ASME)*, Vol. 125, 2003, 398-405.

Asami, T., Nishihara, O., and Baz, A., "Analytical Solutions to H_∞ and H_2 Optimization of Dynamic Vibration Absorbers Attached to Damped Linear Systems", *Journal of Vibration and Acoustics (Transactions of the ASME)*, Vol. 124, 2002, pp. 284-295.

Astrom, K. J., and Wittenmark, B., *Adaptive Control.* Addison-Wesley: Reading, MA, USA, 1989.

Badr, H.M., "Oscillating Inviscid Flow Over Elliptic Cylinders with Flat Plates and Circular Cylinders as Special Cases", *Ocean Engineering*, Vol. 21, No. 1, 1994, pp. 105-113.

Baines, W.D., and Peterson, E. G., "An Investigation of Flow through Screens", *Transactions of the ASME*, Vol. 73, 1951, pp. 467-480.

Bauer, H.F., "Nonlinear Propellant Sloshing in a Rectangular Container of Infinite Length", *Development in Theoretical and Applied Mechanics*, Vol. 3, 1969, pp. 725-759.

Blevins, R. D., *Applied Fluid Dynamics Handbook.* Macmillan: Agincourt, ON, Canada, 1984.

Boggs, D., "Acceleration Indexes for Human Comfort in Tall Buildings—Peak or RMS?", *CTBUH Monograph Chpt. 13: Motion Perception Tolerance and Mitigation*, 1997 (21 pages).

Brock, J. E., "A Note on the Damped Vibration Absorber", *Trans. A.S.M.E.*, 1946, A284.

Brundrett, E., "Prediction of Pressure Drop for Incompressible Flow Through Screens", *Journal of Fluids Engineering*, Vol. 115, 1993, pp. 239-242.

Carrier, G.F., and Miles, J.W., "On the Annular Damper for a Freely Processing Gyroscope", *Journal of Applied Mechanics*, Vol. 27, 1960, pp. 237-240.

Carrothers, P. J. G., and Baines, W. D., "Forces on Screens Inclined to a Fluid Flow", *Journal of Fluids Engineering*, Vol. 97, 1965, pp. 116-117.

Casciati, F., De Stefano, A., and Matta, E., "Simulating a Conical Tuned Liquid Damper", *Simulation Modelling Practice and Theory,* Vol. 11, 2003, pp. 353-370.

Cassolato (Casson), M., and Tait, M., "A Preliminary Study of a Tuned Liquid Damper with Smart Screens", *Proceedings of the 1st Canadian Conference on Effective Design of Structures,* McMaster University, Hamilton, ON, Canada, 2005, pp. 227-236.

Chester, W., "Resonant Oscillations of Water Waves", *Proceedings of Royal Society of London*, Vol. 306, 1968, pp. 5-22.

Chopra, A. K., *Dynamics of Structures: theory and applications to earthquake engineering, 2nd edition.* Prentice-Hall Canada, Inc.: Toronto, 2001.

Chwang, A. T. and Chan, A. T., "Interaction Between Porous Media and Wave Motion", *Annual Review of Fluid Mechanics*, Vol. 30, 1998, pp.53-84.

Cornell, W.G., "Losses in Flow Normal to Plane Screens", *Meeting of the American Society of Mechanical Engineers*, Hartford, CT, 1957, pp. 791-799.

Coulson, C. A., and Jeffrey, A., *Waves: A Mathematical Approach to the Common Types of Wave Motion.* Longman Group Ltd.: New York, 1977, 2nd edition.

Davenport, A.G., "Note on the Distribution of the Largest Value of a Random Function with Application to Gust Loading", *Institute for Civil Engineers*, Vol. 28, 1964, pp. 187-196.

Den Hartog, J. P., *Mechanical Vibrations.* Dover Publications, Inc.: New York, 1985. (republication of *4th edition*, 1956)

Discovery Channel Canada (2005), "Skinny Skyscraper". <http://www.exn.ca/news/video/exn2005/11/29/exn20051129-skyscraper.asx> (online – streaming video) Accessed: 20 Feb. 2007.

Fediw, A. A., *Performance of a One Dimensional Tuned Sloshing Water Damper.* M.E.Sc. Thesis. The University of Western Ontario, London, Canada, 1992.

Fediw, A.A., Isyumov, N., and Vickery, B.J., "Performance of a Tuned Sloshing Water Damper", *Journal of Wind Engineering and Industrial Aerodynamics*, Vol. 57, 1995, pp. 237-247.

Fujino, Y., Pacheco, B. M., Chaiseri, P., and Sun, L. M., "Parametric Studies on Tuned Liquid Damper (TLD) Using Circular Containers by Free Oscillation Experiments", *Structural Engineering / Earthquake Engineering*, JSCE, 5(2), 1988, pp. 381-391.

Gao, H., and Kwok, K.C.S., "Optimization of Tuned Liquid Column Dampers", *Engineering Structures,* Vol. 19, No. 6, 1997, pp. 476-486.

Garrison, C. J., "Comments on Cross-Flow Principle and Morrison's Equation", *Journal of Waterway, Port, Coastal, and Ocean Engineering,* Vol. 111, No. 6, 1985, pp. 1075-1079.

Gerges, R.R., and Vickery, B.J., "Wind Tunnel Study of the Across-Wind Response of a Slender Tower with a Nonlinear Tuned Mass Damper", *Journal of Wind Engineering and Industrial Aerodynamics,* Vol. 91, 2003, 1069-1092.

Graham, E.W., and Rodriguez, A.M., "The Characteristics of Fuel Motion which Affect Airplane Dynamics", *Journal of Applied Mechanics,* Vol. 19, No. 3, 1952, pp. 381-388.

Hadenius, P., "The World's Tallest Buildings [For Now]", *Technology Review Magazine,* July/August 2004 edition, pp. 51-54.

Hoerner, S. F., *Fluid Dynamic Drag.* Hoerner Fluid Dynamics, 1964.

Idelchik, I.E., *Handbook of Hydraulic Resistance, 2nd Edition.* Hemisphere Publishing Corporation: New York, 1986.

Ju, Y.-K., "Structural Behaviour of Water Sloshing Damper with Embossments Subject to Random Excitation", *Canadian Journal of Civil Engineering,* Vol. 31, 2004, pp. 120-132.

Kaneko, S., and Ishikawa, M., "Modeling of Tuned Liquid Damper with Submerged Nets", *Journal of Pressure Vessel Technology (Transactions of the ASME),* Vol. 121, 1999, pp. 334-343.

Kaneko, S., and Yoshida, O., "Modeling of Deepwater-Type Rectangular Tuned Liquid Damper With Submerged Nets", *Journal of Pressure Vessel Technology (Transactions of the ASME),* Vol. 121, 1999, pp. 413-422.

Kareem, A., "Mitigation of Wind Induced Motion of Tall Buildings, *Journal of Wind Engineering and Industrial Aerodynamics*, 11(1-3), 1983: 273-284.

Kareem, A., and Sun, W.J., "Stochastic Response of Structures with Fluid-Containing Appendages", *Journal of Sound and Vibration*, Vol. 119, No. 3, 1987, pp. 389-408.

Kareem, A., Kijewski, T., and Tamura, Y., "Mitigation of Motions of Tall Buildings with Specific Examples of Recent Applications", *Wind and Structures*, Vol. 2, No. 3, 1999, pp. 201-251.

Keulegan, G.H., and Carpenter, L.H., "Forces on Cylinders and Plates in an Oscillating Fluid", *Journal of Research of the National Bureau of Standards*, Vol. 60, No. 5, 1958, pp. 423-440.

Laws, E. M., and Livesey, J. L., "Flow Through Screens", *Annual Review of Fluid Mechanics*, Vol. 10, 1978, pp. 247-66.

Luft, R.W., "Optimal Tuned Mass Dampers for Buildings", *Journal of the Structural Division*, ASCE, Vol. 105, No. 12, 1979, pp. 2766-2772.

McNamara, R. J., "Tuned Mass Dampers for Buildings", *Journal of the Structural Division*, Vol. 103, 1977, pp. 1785-1798.

McNamara, R., Kareem, A., and Kijewski, T., "Ask the Experts…Perception of Motion Criteria for Tall Buildings Subjected to Wind: A Panel Discussion", *Conference Abstract for Reflections from ASCE Structures Congress*, Denver, CO, USA, April 4-6, 2002. <http://www.nd.edu/~nathaz/perception/abstract.html> Accessed: 15 Nov 2006.

Miles, J. W., "Surface Wave Damping in Closed Basins", *Proceedings of the Royal Society of London*, Vol. 297, 1967, pp. 459-475.

Modi, V.J., and Welt, F., "Vibration Control using Nutation Dampers", *International Conference of Flow Induced Vibrations*, England, 1987, pp. 369-376.

Modi, V.J., Welt, F., and Seto, M.L., "Control of Wind-Induced Instabilities through Application of Nutation Dampers: A Brief Overview", *Engineering Structures,* Vol. 17, No. 9, 1995, 626-638.

Morison, J.R., O'Brien, M. P., Johnson, J. W., and Schaaf, S. A., "The Force Exerted by Surface Waves on Piles", *Society of Petroleum Engineers of AIME Transactions,* Vol. 189, 1950, pp. 149-154.

Motioneering (2004). <http://www.motioneering.ca/User/Doc/pp_wall_centre.pdf> (online) Project Brochure. Accessed: 15 Feb. 2007.

Nishihara, O., and Asami, T., "Closed-Form Solutions to the Exact Optimizations of Dynamic Vibration Absorbers (Minimizations of the Maximum Amplitude Magnification Factors)", *Journal of Vibration and Acoustics (Transactions of the ASME)*, Vol. 124, 2002, 576-582.

Noji, T., Yoshida, H., Tatsumi, E., Kosaka, H., and Hagiuda, H., "Study on Vibration Control Damper Utilizing Sloshing of Water", *Journal of Wind Engineering*, Japan Association for Wind Engineering, Vol. 37, 1988, pp. 557-566.

Okajima, A., Matsumoto, T., and Kimura, S., "Aerodynamic Characteristics of Flat Plates with Various Angles of Attack in Oscillatory Flow", *JSME International Journal,* Series B, Vol. 41, No. 1, 1998, pp. 214-220.

Olson, D. E., and Reed, D. A., "A Nonlinear Numerical Model for Sloped-Bottom Tuned Liquid Dampers", *Earthquake Engineering and Structural Dynamics,* Vol. 30, 2001, pp. 731-743.

Prandtl, L., "Attaining a Steady Air Stream in Wind Tunnels", *National Advisory Committee for Aeronautics (NACA),* Technical Note (TM) 726, 1933.

Reed, D., Yeh, H., Yu, J., and Gardarsson, S., "Tuned Liquid Dampers under Large Amplitude Excitation", *Journal of Wind Engineering and Industrial Aerodynamics*, 74-76, 1998, pp. 923-930.

Reed, D., Yu, J., Yeh, H., and Gardarsson, S., "Investigation of Tuned Liquid Dampers under Large Amplitude Excitation", *Journal of Engineering Mechanics*, Vol. 124, No. 4, 1998, pp. 405-413.

Reuter, C., Rettemeier, K., and Köngeter, J., "Experimental Head Loss Determination at Inclined Wedge Wire Fish Protection Screen", *29th IAHR Congress Proceedings,* Beijing, China, 2001. <http://www.iahr.org/e-library/beijing_proceedings/Theme_B/EXPERIMENTAL%20HEAD%20LOSS.html> (online) Accessed: 30 Jan 2006.

Richards, P. J., and Robinson, M., "Wind Loads on Porous Structures", *Journal of Wind Engineering and Industrial Aerodynamics*, Vol. 83, 1999, pp. 455-465.

Sakai, F., Takaeda, S., and Tamaki, T., "Tuned Liquid Column Damper – New Type Device for Suppression of Building Vibrations", *Proceedings of International Conference on High-rise Buildings*, Nanjing, China, 1989, pp. 926-931.

Schubauer, G. B., Spangenberg, W. G., and Klebanoff, P.S., "Aerodynamic Characteristics of Damping Screens", *National Advisory Committee for Aeronautics (NACA)*, Technical Note 2001, 1950.

SkyscraperPage (2007). <http://skyscraperpage.com/cities/?buildingID=6999> (online) Accessed: 18 Mar. 2007.

Soong, T. T., and Dargush, G. F., *Passive Energy Dissipation Systems in Structural Engineering*. John Wiley & Sons: Toronto, 1997.

Sun, L. M., Fujino, Y., and Koga, K., "A Model of Tuned Liquid Damper for Suppressing Pitching Motion of Structures", *Earthquake Engineering and Structural Dynamics*, Vol. 24, 1995, pp. 625-636.

Sun, L.M., Fujino, Y., Pacheco, B.M., and Chaiseri, P., "Modelling of Tuned Liquid Damper (TLD)", *Journal of Wind Engineering and Industrial Aerodynamics,* 41-44, 1992, pp. 1883-1894.

Szemplinska-Stupnicka, W., "Higher Harmonic Oscillations in Heteronomous Non-Linear Systems with One Degree of Freedom", *International Journal of Non-Linear Mechanics*, Vol. 3, 1968, pp. 17-30.

Tait, M. J., "Modelling and Preliminary Design of a Structure-TLD System", **submitted to** *Engineering Structures,* May 2007.

Tait, M J., El Damatty, A. A., and Isyumov, N., "An Investigation of Tuned Liquid Dampers Equipped with Damping Screens under 2-D Excitation", *Journal of Earthquake Engineering and Structural Dynamics*, 34, 2005, pp. 719-735.

Tait, M. J., El Damatty, A. A., Isyumov, N., and Siddique, M. R., "Numerical Flow Models to Simulate Tuned Liquid Dampers (TLD) with Slat Screens", *Journal of Fluids and Structures,* 20(8), 2005, pp. 1007-1023.

Tait, M. J., El Damatty, A.A., and Isyumov, N., "Testing of Tuned Liquid Damper with Screens and Development of Equivalent Mechanical Model", *Journal of Wind and Structures*, 7(4), July 2004, pp. 215-234.

Tait, M. J., Isyumov, N., and El Damatty, A. A., "The Effectiveness of a 2-D TLD and its Numerical Modelling [using 1-D TLD Design Theory]", *ASCE Journal of Structural Engineering*, 133(2), 2007, pp. 251-263.

Tait, M. J., Isyumov, N., and El Damatty, A.A., "The Efficiency and Robustness of a Uni-Directional Tuned Liquid Damper and Modelling with an Equivalent TMD", *Journal of Wind and Structures*, 7(4), July 2004, pp. 235-250.

Tait, M. J., *The Performance of 1-D and 2-D Tuned Liquid Dampers*. Ph.D. Thesis. The University of Western Ontario, London, Canada, 2004.

Tamura, Y., "Application of Damping Devices to Suppress Wind-Induced Responses of Buildings", *Journal of Wind Engineering and Industrial Aerodynamics*, 74-76, 1998, pp. 49-72.

Tamura, Y., Fujii, K., Ohtsuki, T., Wakahara, T., and Kohsaka, R., "Effectiveness of Tuned Liquid Dampers under Wind Excitation", *Engineering Structures*, Vol. 17, No. 9, 1995, pp. 609-621.

Taylor, G. I., and Batchelor, G. K., "The Effect of Wire Gauze on Small Disturbances in a Uniform Stream", *Journal of Mechanics and Applied Mathematics,* Vol. 2, Pt. 1, 1949, pp. 1-29.

Vickery, B. J., and Davenport, A. G., "An Investigation of the Behaviour in Wind of the Proposed CenterPoint Tower in Sydney, Australia", *Research Report BLWT-1-70*, The Boundary Layer Wind Tunnel Laboratory, The University of Western Ontario, London, Canada, 1970.

Vickery, B. J., Galsworthy, J. K., and Gerges, R. R., "The Behaviour of Simple Non-Linear Tuned Mass Dampers", *Proceedings of the Sixth World Congress of the Council on Tall Buildings and Urban Habitat*, Melbourne, Australia, 2001.

Warburton, G.B., "Optimum Absorber Parameters for Various Combinations of Response and Excitation Parameters", *Earthquake Engineering and Structural Dynamics*, Vol. 10, 1982, pp. 381-401.

Warnitchai, P. and Pinkaew, T., "Modelling of Liquid Sloshing in Rectangular Tanks with Flow-Dampening Devices", *Engineering Structures,* Vol. 20, No. 7, 1998, pp. 593-600.

Weisbach, J., "Die Experimental-Hydraulik", 1855, p. 133, Englehardt, Freiburg.

Wiesner, K.B., "Tuned Mass Dampers to Reduce Building Wind Motion", *Proceedings of the ASCE Convention and Exposition,* Boston, MA, 1979, pp. 1-21.

Yalla, S. K., and Kareem, A., "Optimal Absorber Parameters for Tuned Liquid Column Dampers", *Journal of Structural Engineering,* 126(8), 2000, pp. 906-915.

Yalla, S. K., and Kareem, A., "Semiactive Tuned Liquid Column Dampers: Experimental Study", *Journal of Structural Engineering,* 129(7), 2003, pp. 960-971.

Yeh, H. H. and Shrestha, M., "Free-Surface Flow Through Screen", *Journal of Hydraulic Engineering,* Vol. 115, No. 10, 1989, pp. 1371-1385.

Yu, J. K., Wakahara, T., and Reed, D. A., "A Non-Linear Numerical Model of the Tuned Liquid Damper", *Earthquake Engineering and Structural Dynamics.* Vol. 28, 1999, 671-686.